FZD-527

Phase separation in carbon:transition metal nanocomposite thin films

Markus Berndt

Dezember 2009

Wissenschaftlich-Technische Berichte
FZD-527 2009 · ISSN 1437-322X

WISSENSCHAFTLICH-TECHNISCHE BERICHTE

Forschungszentrum
Dresden Rossendorf

Wissenschaftlich-Technische Berichte
FZD-527
Dezember 2009

Markus Berndt

Phase separation in carbon:transition metal nanocomposite thin films

Forschungszentrum
Dresden Rossendorf

Institut für Ionenstrahlphysik und Materialforschung
Forschungszentrum Dresden-Rossendorf e. V.

Phase separation in carbon:transition metal nanocomposite thin films

von der
Fakultät Mathematik und Naturwissenschaften
der Technischen Universität Dresden
genehmigte

Dissertation
zur Erlangung des akademischen Grades
Doctor rerum naturalium
(Dr. rer. nat.)

vorgelegt von
Dipl.-Ing. (FH) Markus Berndt
geboren am 14.05.1981 in Zwickau

Dresden 2009

Eingereicht am 09.09.2009

1.Gutachter: Prof. Dr. W. Möller
2.Gutachter: Prof. Dr. W. Zahn

Contents

Abbreviations

3D	Three-dimensional
a-C	Amorphous carbon
a-C:H	Hydrogenated amorphous carbon
BF	Bright-field
BN	Boron nitride
BWF	Breit-Wigner-Fano
BZ	Brillouin zone
C	Carbon
c	Cubic
ccp	Cubic closed-packed
CN_x	Carbon nitride
cs	Cross-section
C:TM	Carbon:transition metal
DF	Dark-field
DSC	Differential scanning calorimetry
DLC	Diamondlike carbon
ERDA	Elastic recoil detection analysis
fcc	Face-centered cubic
FFT	Fast Fourier transformation
FWHM	Full width at half maximum
FL	Fullerene-like
GID	Grazing incidence diffraction
GLC	Graphite-like carbon
GISAXS	Grazing incidence small angle X-ray scattering
h	Hexagonal
hcp	Hexagonal closed-packed
HOPG	Highly oriented pyrolytic graphite
HRTEM	High resolution transmission electron microscopy
IBS	Ion beam sputtering
IUPAC	International Union of Pure and Applied Chemistry
MS	Magnetron sputtering
nc-graphite	Nanocrystalline graphite
NPs	Nanoparticles
PACVD	Plasma-assisted chemical vapor deposition
PFCVA	Pulsed filtered cathodic vacuum arc
PLD	Pulsed laser deposition
pv	Plan-view

PVD	Physical vapor deposition
SAED	Selected area electron diffraction
SEM	Scanning electron microscopy
SQUID	Superconducting quantum interference device
T_a	Annealing temperature
ta-C	Tetrahedral amorphous carbon
ta-C:H	Hydrogenated tetrahedral amorphous carbon
TEM	Transmission electron microscopy
TK	Tuinstra-Koenig
TM	Transition metal
T_s	Substrate temperature
XRD	X-ray diffraction
VDOS	Vibrational density of states

1 Introduction

Nanocomposites consist of two or more phases, whereby at least one component has one dimension less than 100 nm [1]. They are advanced functional materials whose mechanical, electrical, optical, and structural properties cannot be predicted from the properties of the individual components alone, but strongly depend on the composite structure. This is mainly associated with the high surface to volume ratio of the nanometer sized phase resulting in many interfaces between the constituent phases.

In thin films, the small grain size which is by a factor of more than 100 smaller than for bulk materials and the large surface-to-bulk ratio cause thin films to behave different from their bulk counterparts [2]. Nanocomposite films have received considerable interest for their potential application in many fields [1]. Despite the important role of interfaces for nanocomposite properties, there is a lack of understanding in the structure forming phenomena of multiphase films and their stability involving the interplay of thermodynamic and kinetic factors. A deposition can be considered as a sudden quench from a homogeneous mixture of two or more components in the vapor phase upon adsorption on the substrate into a state corresponding to a phase coexistence in the phase diagram [3]. Thermodynamically, the systems tends to phase separate into its major film constituents or the respective compounds, while the phase separation process is dictated by the kinetical parameters such as surface diffusivity of adatoms and their covering rate.

Among nanocomposite films, carbon:transition metal (C:TM) nanocomposite films possess a unique combination of properties which make them promising candidates for high-density magnetic recording media, spintronic devices, low-friction solid lubricants, or hard wear resistant coatings [4–19]. Such nanocomposites have been synthesized by different physical vapor deposition (PVD) techniques such as ion beam co-sputtering [4, 10, 20–24], magnetron sputtering (MS) [5, 17, 18, 25, 26], pulsed filtered cathodic vacuum arc (PFCVA) deposition [6, 9],or pulsed laser deposition (PLD) [16, 27], while hybrid processes such as plasma-assisted chemical vapor deposition (PACVD) [28–31] are also appropriate for the synthesis of C:TM nanocomposite films.

The structure of so-grown nanocomposites consists of metal-rich nanoparticles embedded in a carbon matrix. Dependent on the growth conditions, metal-rich nanoparticles can be either metallic [10, 18, 20, 23–25] or carbidic [18, 20, 25, 32] (chemical state), amorphous [5, 25, 33, 34] or crystalline [17, 20, 25, 32] (phase), globular [17, 18] or elongated [10, 17, 18, 20, 25, 32] (morphology). On the other hand, the carbon matrix can be amorphous [6, 16, 18, 23], graphite-like with graphene layers curved into

a cylindrical shape encapsulating elongated nanoparticles [6, 10, 18, 20, 23, 25], and fullerene-like (FL) with a spherical-like curvature encapsulating globular nanoparticles [17, 18]. It has been demonstrated that such a growth proceeds via feedback interactions between the dispersed phase and the matrix [3], with the matrix affecting the morphology of the dispersed phase, the latter influencing on its turn the matrix structure. Obviously, the chemical interaction between the nanocomposite constituents has to play a role in addition to other growth parameters such as temperature, composition, presence of energetic ions, etc... Although different C:TM systems have been investigated in the literature, the growth technique sensitivity does not allow drawing global conclusions and general tendencies. There is a lack of a systematic investigation to reveal the dispersed phase-matrix feedback interactions and the influence of the C-TM chemistry on the growth-structure relationship of C:TM nanocomposite films. Thus, the purpose of this work is to shed some light on these complex interactions and to disentangle the underlying mechanisms responsible for a particular nanostructure formation.

In order to fill this gap, this work is a comprehensive study on structural changes in C:TM nanocomposite films of *both* the dispersed metal-rich phase and the carbon matrix. Three TMs have been chosen to be incorporated into the carbon matrix based on their chemical affinity to the carbon matrix, namely vanadium, cobalt and copper. In addition to their tendency to form carbides (V - strong carbide former, Co - metastable carbide former, Cu - non-carbide former), the phase diagrams of these elements with carbon represent three different classes: intermediate compound phase diagram for V-C, eutectic for Co-C and peritectic for Cu-C [35]. Thus, the tendencies observed for each of these elements are expected to be at least partially valid for other systems described with the same phase diagram type. The nanostructural development of C:TM thin films is investigated in two regimes: during growth which is limited by surface diffusion and during annealing controlled by bulk diffusion. The latter represents the approach of the system toward the thermodynamic equilibrium, while the former highlights the interplay of thermodynamic and different kinetic factors.

In this study, four parameters affecting the film structure are varied: growth temperature (RT-500°C), annealing temperature (300-700°C), metal type (V, Co, and Cu) and content (15-40 at.%). The influence of these parameters on the composite structure is reported. Methodically, the nanocomposite structure is determined by combined elastic recoil detection analysis (ERDA), X-ray diffraction (XRD), transmission electron microscopy (TEM), and Raman spectroscopy. Recently, the study on C:Ni nanocomposites [20] has demonstrated that the combination of these analytical techniques is appropriate for the characterization of both nanocomposite constituents - matrix and dispersed phase, provides a better understanding of the structure forming phenomena in composite films, and allows to highlight the dispersed phase-matrix feedback interactions. The C:TM nanocomposite films were grown by ion beam co-sputtering. Despite of its simplicity, this synthesis technique allows a high and independent control over synthesis parameters such as sputtering ion type, flux, and energy, and substrate temperature. In order to underline the metal effect on the surrounding carbon phase and on the thermal stability of the films a series of pure carbon samples has been

deposited at identical growth conditions for comparative spectroscopic investigations.

This thesis consists of the following chapters. The basic principles are reviewed in section two. The experimental part and the film characterization techniques are presented in sections three and four. The results obtained on as-deposited films as a function of growth temperature, metal type and content are reported and discussed in section five. In the same section, the modification of phases and morphology as a result of annealing are studied. Part six summarizes the findings of this work and presents the conclusions.

2 Basic principles

As this work concerns the investigation of carbon:transition metal nanocomposite thin films, the aim of this introductory chapter is to give an overview on the bonding behavior of carbon, transition metals (TMs) and their respective carbides - the principle constituents of C:TM nanocomposites - as well as on C:TM phase diagrams, the nanostructural evolution during thin film growth, and on the structure of C:TM nanocomposites. The different types of hybridization of the carbon atom and general properties of the carbon allotropes are described in section 2.1 and 2.2. As phase structure and morphology of a composite are influenced by the miscibility of the main film constituents, section 2.3 considers the transition metals and their tendency to form carbides. In section 2.4 the phase diagrams of carbon with the three TMs used in this work (V, Co, and Cu) are presented and described. The fundamental film growth processes and resulting structure zone models (SZMs) during physical vapor deposition (PVD) of single- and multiphase systems are summarized in section 2.5. The description of the film structure and morphology of C:TM (TM=V, Co, and Cu) nanocomposites in section 2.6 closes the introductory chapter.

2.1 Bonds between carbon atoms

Atomic carbon (C) has a $1s^2 2s^2 2p^2$ electronic ground state configuration with two electrons occupying the innermost K shell and four electrons occupying the second L shell [36, 37]. The electrons from completely filled shells and subshells, called orbitals, (1s and 2s) do not take part in any bonding. Only the electrons located in the outer orbital, namely the two 2p orbitals, are available for bonding to other atoms and are called valence electrons. Carbon in this state would be divalent, since only two electrons are available for bonding [36]. Divalent carbon indeed exists and is found in some highly transient-organic intermediates such as the carbenes [36]. However, the carbon allotropes and the stable carbon compounds are not divalent but tetravalent, which means that four valence electrons are present [38]. The increase in valence electrons is achieved by the formation of hybrid atomic orbitals.

In order to obtain four valence electrons, the arrangement of the electrons in the L shell of the carbon atom in the ground state is modified as one of the 2s electrons is promoted to the higher 2p orbital. These new orbitals are called hybrids since they combine the 2s and 2p orbitals and are labeled sp^3 since they are formed from one s and three p orbitals [36]. The tetrahedral symmetry is found in structures like diamond

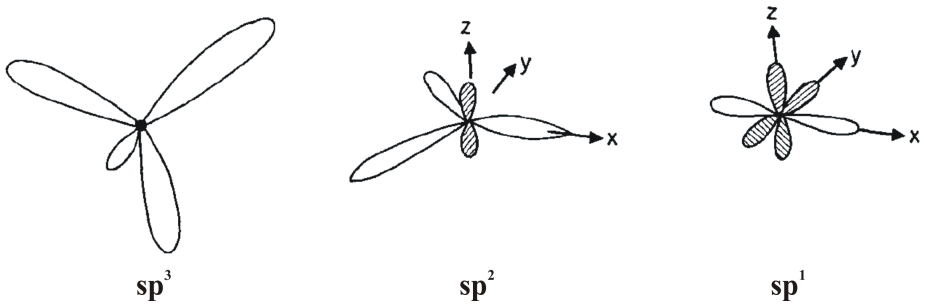

Figure 2.1: Schematic presentation of sp^3, sp^2 and sp^1 hybridizations [39, 40]. The open loops denote strong σ-bonds and the shaded loops denote weak π-bonds.

or methane (CH_4) where a carbon atom is bonded to four other carbon or hydrogen atoms, respectively, by strong covalent sigma bonds using 2s, $2p_x$, $2p_y$, $2p_z$ orbitals in an sp^3 configuration (figure 2.1). The distinguishing feature of a sigma (σ) bond is that the orbital overlap lies directly between the two nuclei, while the pi (π) bond has orbital overlap off to the sides of the line joining the two nuclei. In the graphite structure, strong in-plane sigma bonds are formed between a carbon atom and its three nearest neighbors from 2s, $2p_x$ and $2p_y$ orbitals. This bonding arrangement, denoted by sp^2, is achieved by the promotion and combination of one of the ground state 2s electrons with two of the 2p orbitals. The remaining unhybridized electron with a p_z orbital directed perpendicularly to the plane of the three sp^2 orbitals provides only weak interplanar bonding (pi bond), but is responsible for the semimetallic electronic behavior in graphite [37]. The trigonal orbital is the basis of all graphitic structures and aromatic compounds. The third type is the sp^1 hybridization consisting of two sigma and two pi bonds. The sp molecules have a linear structure due to the mutual repulsion of the two sigma bonds. Examples of molecules having sp bonds are the gas acetylene and the carbynes, which are cross-linked linear-chain carbon polytypes, usually unstable [41].

2.2 The carbon allotropes: graphite, diamond, fullerenes and others

Carbon possesses various atomic structures with different hybrid configurations (sp, sp^2, sp^3) called the allotropes of carbon. This capability makes carbon unique in that simple changes in its local bonding can give rise to materials as diverse as graphite, diamond, fullerenes and their many derivatives like carbon nanotubes, and disordered, nanostructured and amorphous carbons [37, 42]. The carbon allotropes can be classified into three major categories: (i) the sp^2 structures which include graphite, the graphitic materials, amorphous carbon, and other carbon materials, (ii) the sp^3 structures which include diamond and lonsdaleite (a form detected in meteorites) and (iii) the fullerenes [36]. Examples of carbon allotropes are shown in figure 2.2. In addition to the natural carbon materials, like natural single crystal graphite flakes or diamond,

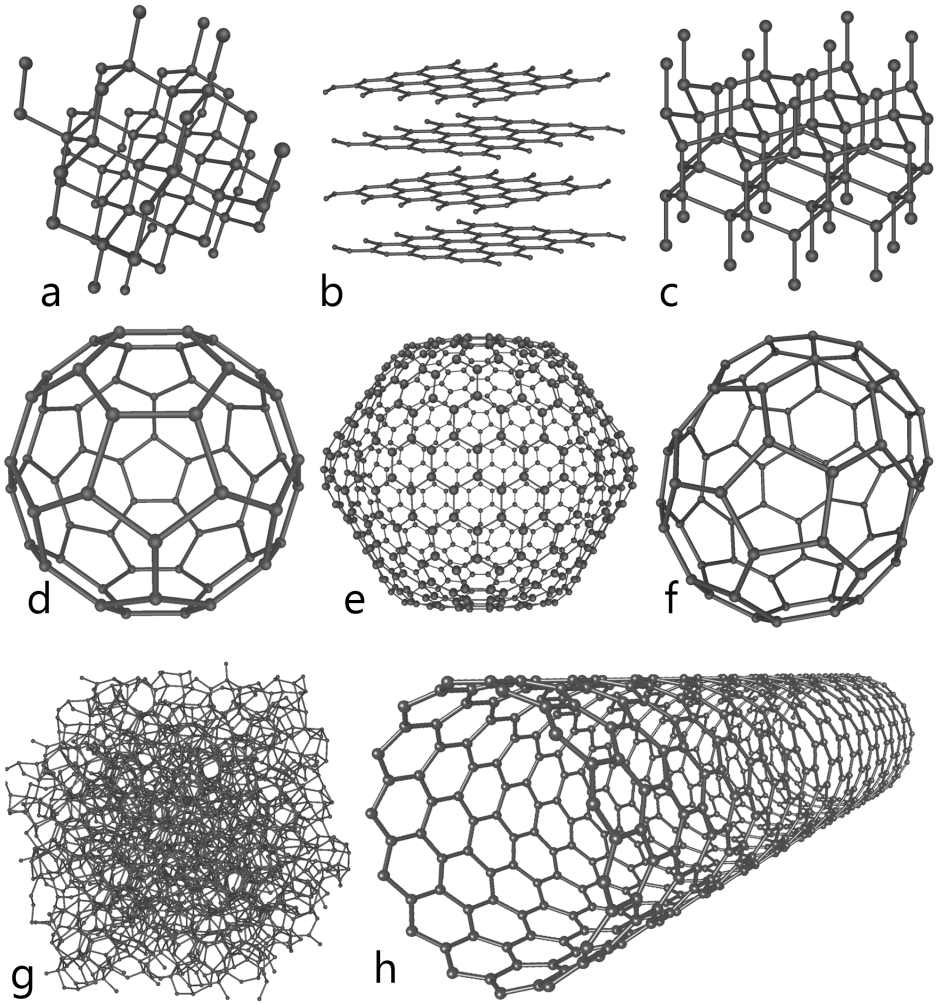

Figure 2.2: Some allotropes of carbon: (a) diamond, (b) graphite, (c), londsdaleite, (d)-(f) fullerenes (C_{60}, C_{540}, C_{70}), (g) amorphous carbon, (h) carbon nanotube [51].

synthetic products exist such as kish graphite [43], highly oriented pyrolytic graphite (HOPG) [44], glassy carbon [45], carbon fibers [46], nanotubes [47–49] and graphene [50].

Graphite has a hexagonal structure which is highly anisotropic, exhibiting metallic behavior in the basal (ab) plane and poor electrical conductivity perpendicular to the plane (along the c-axis) [52]. In contrast, diamond is an isotropic cubic wide gap semiconductor [53]. In terms of mechanical properties diamond is by far the hardest known material, while graphite can be one of the softest [36, 37]. Though graphite and diamond are rather inert under ambient temperatures and pressures, they can transform into one another when exposed to special conditions [54, 55]. The fullerenes are different from either one forming closed-cage structures that combine both sp^2 and sp^3 bonds [36].

The great versatility of carbon materials arises from the strong dependence of their physical properties on the ratio of sp^2 (graphitelike) to sp^3 (diamondlike) bonds [57, 58].

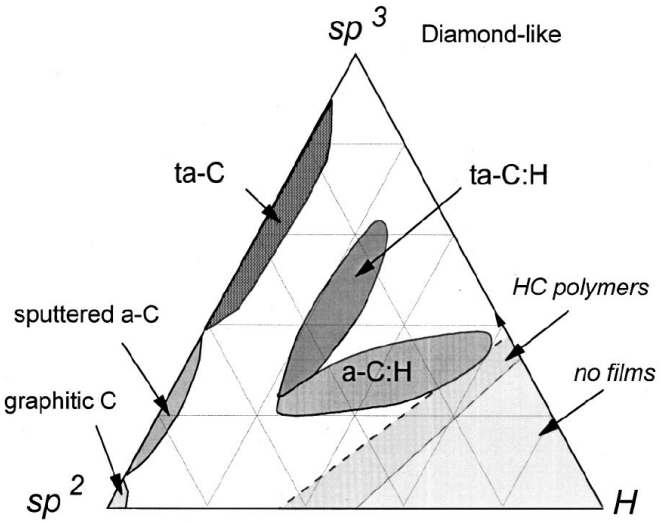

Figure 2.3: Ternary phase diagram of amorphous carbons. The three corners correspond to diamond, graphite, and hydrocarbons, respectively [56].

There exist many forms of sp^2-bonded carbons with various degrees of graphitic ordering, ranging from microscrystalline graphite to glassy carbon. In general, an amorphous carbon can have any mixture of sp^3, sp^2, and even sp^1 sites, with the possible presence of up to 60 at.% hydrogen [56]. The ternary phase diagram in figure 2.3 shows possible compositions. Diamondlike carbon (DLC) is defined as an amorphous (a-C) carbon with a significant amount of sp^3 hybridized carbon atoms. The hydrogenated amorphous carbons (a-C:H) have a rather small C-C sp^3 content. DLC's with a higher sp^3 content are called tetrahedral amorphous carbon (ta-C) and its hydrogenated analog ta-C:H. The key parameters of interest in such materials are (1) the sp^3 content; (2) the clustering of the sp^2 phase; (3) the orientation of the sp^2 phase; (4) any cross-sectional structure; and (5) the H content [42]. Amorphous carbons with the same sp^3 and H content but different sp^2 clustering, sp^2 orientation and cross-sectional nanostructure show different optical, electronic and mechanical properties [59].

2.3 Transition metals and their carbides

In the periodic table of elements in figure 2.4 the 40 chemical elements with the atomic numbers 21-30, 39-48, 57-80 and 89-112 are referred to as transition elements or transition metals. They are positioned between the elements of main group IIA and IIIB and contain electrons in d atomic orbitals. The name *transition* comes from their position in the periodic table of elements. In each of the four periods in which they occur, these elements represent the successive addition of electrons to the d atomic orbitals of the atoms. A definition by the IUPAC (International Union of Pure and Applied Chemistry) defines a transition metal as an element whose atom has an incomplete d sub-shell, or which can give rise to cations with an incomplete d sub-shell [60]. By this

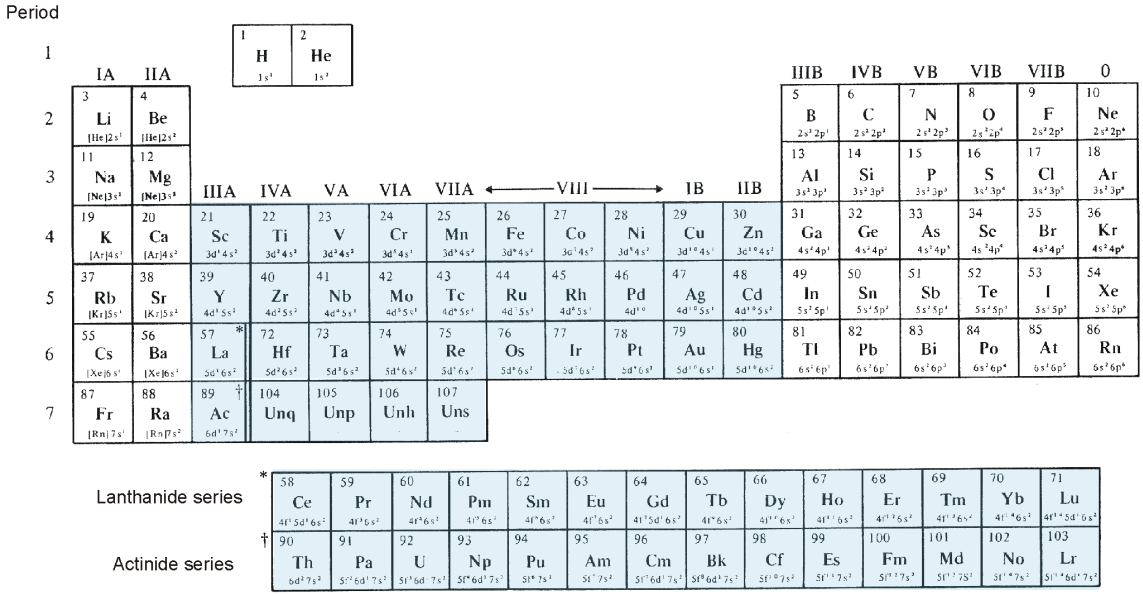

Figure 2.4: Periodic table of elements [61]. Lanthanides and actinides form the inner transition elements. Elements 108-112 are not shown in the table.

definition zinc, cadmium and mercury are excluded from the transition metals, as they have a d^{10} configuration.

Transition metals strongly differ in their physical and chemical properties. The reason for this behavior is the different number of d electrons, which results in partially or completely filled d sub-shells. Transition metals may have multiple oxidation states, they form complexes and exhibit a good catalytic activity [62, 63]. Iron, cobalt and nickel are ferromagnetic at room temperature while the others are not. In comparison to the alkali and alkaline earth metals, transition metals are fairly hard and exhibit, with the exception of the metals of the zinc group, a relatively high melting point [62].

Transition metals show a different chemical affinity to carbon which decreases along one period with the exception of group IIIA elements. Therefore, transition metals can form stable, metastable or relatively unstable carbides [61, 62] which are separated into three different groups: acetylides, interstitial carbides and intermediate transition metal carbides. As this work concerns vanadium, cobalt and copper, in the following the 3d transition metals and their respective carbides will be considered.

Together with the methanides, acetylides belong to the salt-like carbides. Acetylides contain a C_2-unit and are formed by the alkali and alkaline earth metals, e. g. Na_2C_2 and CaC_2, and by the lanthanides, e.g. LaC_2. Copper forms explosive acetylides [61, 62].

Interstitial carbides are formed by the transition metals of group IVA, VA and VIA, with the exception of chromium [61, 62]. These carbides are chemically quit inert, refractory, harder than pure metals, they show metallic conductivity and exhibit a high melting point in the range of 3000-4000°C [61, 62]. Carbon atoms fill octahedral

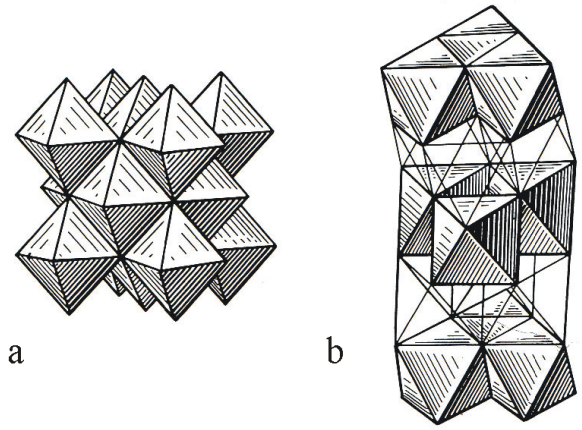

Figure 2.5: Structure of NaCl (a) and CdI_2 (b) in polyhedra [64]. Cl^- and I^{2-} ions are situated on the corners of the polyhedron while Na^+ and Cd^{2+} ions occupy the holes.

interstices in a close packed metal lattice, which only occurs if the metal atom radius is greater than approximately 135 pm [61]. When the metal atoms are cubic closed-packed (ccp), all of the octahedral interstices are filled with carbon achieving 1:1 stoichiometry with the rock salt, NaCl, structure (figure 2.5 (a)). When the close packed arrangement of metal atoms is hexagonal (h) instead of cubic (c), as the octahedral interstices lie directly opposite each other on either side of the layer of metal atoms, filling only one of these with carbon atoms achieves 2:1 stoichiometry with the CdI_2 structure (figure 2.5 (b)) [61]. An example for the latter case is V_2C. In the case of alternating layer sequences of metal atoms, intermediate stoichiometries exist, e. g. V_4C_3 (hhcc) [61]. Also regularly disordered structures of the NaCl-type are known, like V_8C_7 and V_6C_5, which demonstrates the range of stoichiometries of interstitial carbides [61].

The transition metals Cr, Mn, Fe, Co and Ni, with an atomic radius below 135 pm, do not form typical interstitial carbides, but intermediate transition metal carbides with a more complex structure [61, 62]. These compounds appear either as metastable carbides or intermediate phases. Multiple stoichiometries are common, e.g. iron forms a number of carbides, Fe_3C, known as cementite, Fe_7C_3 and Fe_2C [61]. The carbides of Cr, Mn, Fe, Co and Ni are more reactive than the interstitial carbides. These compounds share features with both the inert interstitials and the reactive salt-like carbides.

2.4 Phase diagrams

2.4.1 General considerations

A phase diagram is a type of graph showing the equilibrium conditions between the thermodynamically-distinct phases as a function of composition, temperature and pressure [2]. Phases not only denote solid, liquid and gaseous states of pure elements or

compounds, but also refer to different crystal structures in the solid state. Phase transitions that occur with decreasing temperature at certain temperature values from gas to liquid and further to solid phase or in the solid state imply that the system tends to minimize the Gibbs free energy [2, 65]. Phase diagrams not only provide solubility data as a function of temperature, but they contain plenty of thermodynamic information on systems in equilibrium which can easily be interpreted without the use of complex laws, functions, or equations. They have been experimentally determined for lots of systems by numerous researchers over the years and provide an invaluable guide when synthesizing materials [35].

The result of mixing together two or more components, e.g. metals, may be quite complex. Whether two components are miscible depends on their atomic radii, crystal structure, electronegativities and valency. Relatively small concentrations of a solute metal in a given solvent metal may form a solid solution in which the crystal structure characteristic of the solvent is maintained, except for changes in the dimensions of the unit cell. Atoms of the solute component may replace those of the solvent in the structure if the atomic diameters of the two components are comparable, or, if the atomic diameter of the solute element is much smaller than that of the solvent, the solute atoms may occupy interstitial positions between the atoms of the solvent [65]. At higher solute concentrations, the different types of atoms may form a new phase with a crystal structure which differs from that of either component. Such stable configurations of unlike atoms are known as intermediate or intermetallic phases [65, 66].

In a binary phase diagram the temperature is plotted against the relative concentrations of the two components A and B showing the compositions of solid and liquid phases which are in equilibrium at various temperatures. The simplest type of phase diagram occurs if the components are completely miscible in the solid state (see figure 2.6 (a)). At temperatures and compositions corresponding to points above the curve *LMO* (the *liquidus* curve) the alloy consists of a single liquid phase. For temperatures and compositions corresponding to points below curve *LNO*, which is known as the *solidus* curve, the system exists as a mutual solid solution of the two components A and B. At temperatures and compositions between the two curves, the alloys consist of a mixture of liquid and solid phases. Within the area LMON at any given temperature between the freezing points of A and B, the compositions of solid and liquid phases are fixed, i.e. in figure 2.6 (a) at temperature T_3, the compositions of solid and liquid are p and q. Besides, at this temperature, an alloy of composition r consists of solid and liquid phases in the ratio rq/pr. Any alteration of temperature within this range causes the composition and ratio of solid and liquid in equilibrium with each other to change.

Systems with a limited mutual solid solubility are more complex (figure 2.6 (b)-(d)). In these systems horizontal isothermal boundaries indicate phase transformations involving three phases. The following common reactions may occur at these critical

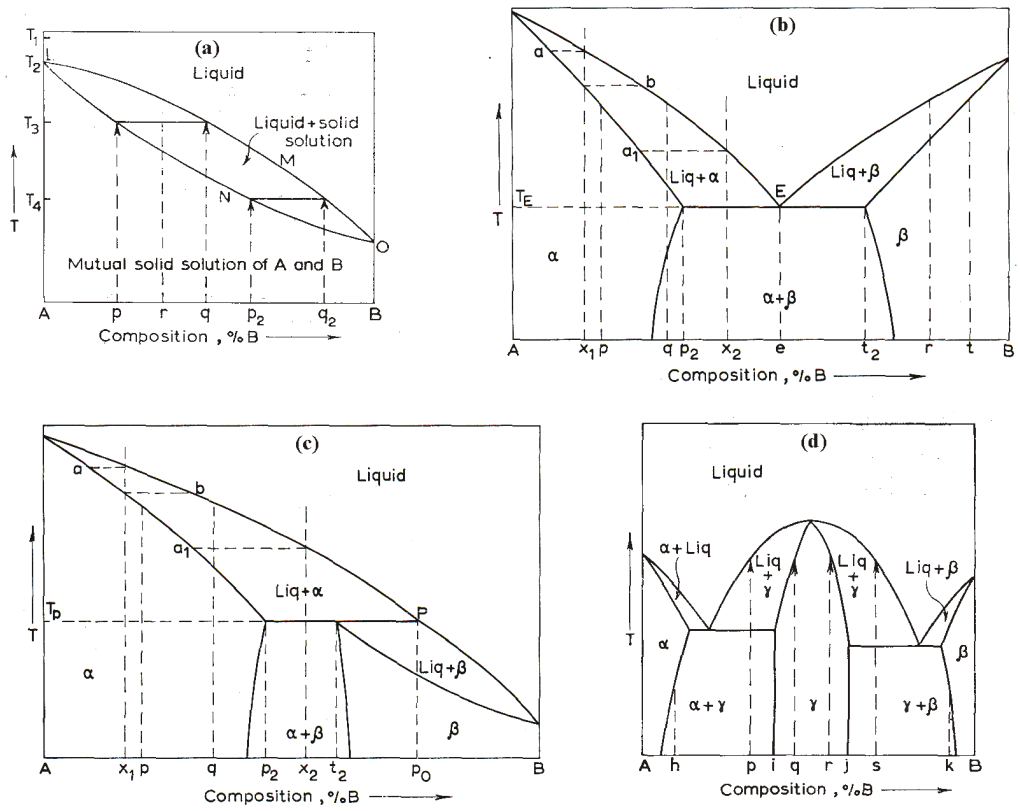

Figure 2.6: Binary alloy phase diagrams with complete solid miscibility (a) and with limited mutual solid solubility (b)-(d) [65].

isotherms, where α, β and γ are solid solutions and L denotes liquid phase [2, 65]:

$$Eutectic \quad L \rightarrow \alpha + \beta \tag{2.1}$$

$$Eutectoid \quad \gamma \rightarrow \alpha + \beta \tag{2.2}$$

$$Peritectic \quad L + \alpha \rightarrow \gamma \tag{2.3}$$

$$Peritectoid \quad \alpha + \beta \rightarrow \gamma \tag{2.4}$$

Figure 2.6 (b) displays an eutectic system. The point E is known as the eutectic point having the lowest melting point of the system [66]. Liquid of the eutectic composition directly solidifies at the eutectic temperature T_E to form a mixture of the two solid phases α and β (equation 2.1) of compositions p_2 and t_2 respectively, in the proportions et_2/p_2e. Left and right of the eutectic point a mixture of liquid and solid phases is formed before the complete solidification. In this case a peritectic reaction analogous to equation 2.3 takes place which means a liquid and a solid phase of fixed compositions react at a fixed temperature to form another solid phase. The corresponding reactions are: L+$\alpha \rightarrow \beta$ and L+$\beta \rightarrow \alpha$.

Figure 2.6 (c) also shows three phases in equilibrium at point P; liquid of composition p_0 is in equilibrium with α and β of compositions p_2 and t_2. The composition p_0 is known as the peritectic composition and the system therefore as the peritectic system.

At the peritectic point liquid of composition p_0 reacts with α of composition p_2 to form β of compositions t_2 (equation 2.3).

A system including an intermediate phase is illustrated in figure 2.6 (d). Intermediate phases are formed within certain composition ranges and have a crystal structure different from those of either of the terminal solid solutions [65]. The intermediate phase γ is able to dissolve limited amounts of both components A and B. In addition, the system contains two eutectic reactions, L $\rightarrow \alpha+\gamma$ and L $\rightarrow \gamma+\beta$ and peritectic reactions left and right of the eutectic points analogous to equation 2.3.

For some purposes, a relatively complex system may be considered as built up from the combination of simpler systems. Thus, figure 2.6 (d) is actually two diagrams of the type of figure 2.6 (b) placed side by side with the components being α and γ for the left side, and γ and β for the right side. Binary phase diagrams often contain not merely one, but a whole sequence of intermediate phases, some of which may be formed at maxima on the liquidus curve and others by peritectic reactions [65].

With decreasing temperature transformations in the solid state may take place similar to those already considered for the liquid$\rightleftharpoons$solid equilibrium. New phases may be formed in the solid state by a process analogous to an eutectic or a peritectic reaction known as an eutectoid (equation 2.2) or a peritectoid reaction (equation 2.4), respectively. In addition, transformation of one solid phase into another can occur. The simplest form of this type of transformation can be found in pure metals, e.g iron transforms in the solid state with decreasing temperature from the δ into the γ phase and further into the α phase [66].

2.4.2 Phase diagrams of carbon-vanadium, carbon-cobalt and carbon-copper

Figure 2.7 (a) shows the phase diagram for the system carbon-vanadium, which is based on Ref. [67–70]. This phase diagram belongs to the type described in figure 2.6 (d) but contains several intermediate phases. At elevated temperatures, only two intermediate phases (V_2C and VC) exist. Both phases exibit wide ranges of homogeneity. The V_2C phase is formed by a peritectic reaction between liquid and VC. Decreasing temperature results in a peritectoid reaction between V_2C and VC near 1320°C to form the V_4C_{3-x} phase. This phase is nearly invariant in stoichiometry in contrast to V_2C and VC. This invariance exists even though the phase is C deficient, with the crystal structure indicating an ideal stoichiometry of V_4C_3, but with a stoichiometry near V_3C_2 in reality. On this basis, the composition of the phase is referred to as V_4C_{3-x} [35]. At still lower temperatures, transformations within the phase fields of V_2C and VC occur, which yield in a range of stoichiometries with complicated phase relationships. The phase relationships for the region between 27 and 34 at.%C must be considered tentative. Although these relationships agree with the majority of the available experimental data, some uncertainties exist. Crystallographic data indicate that the V-rich portion

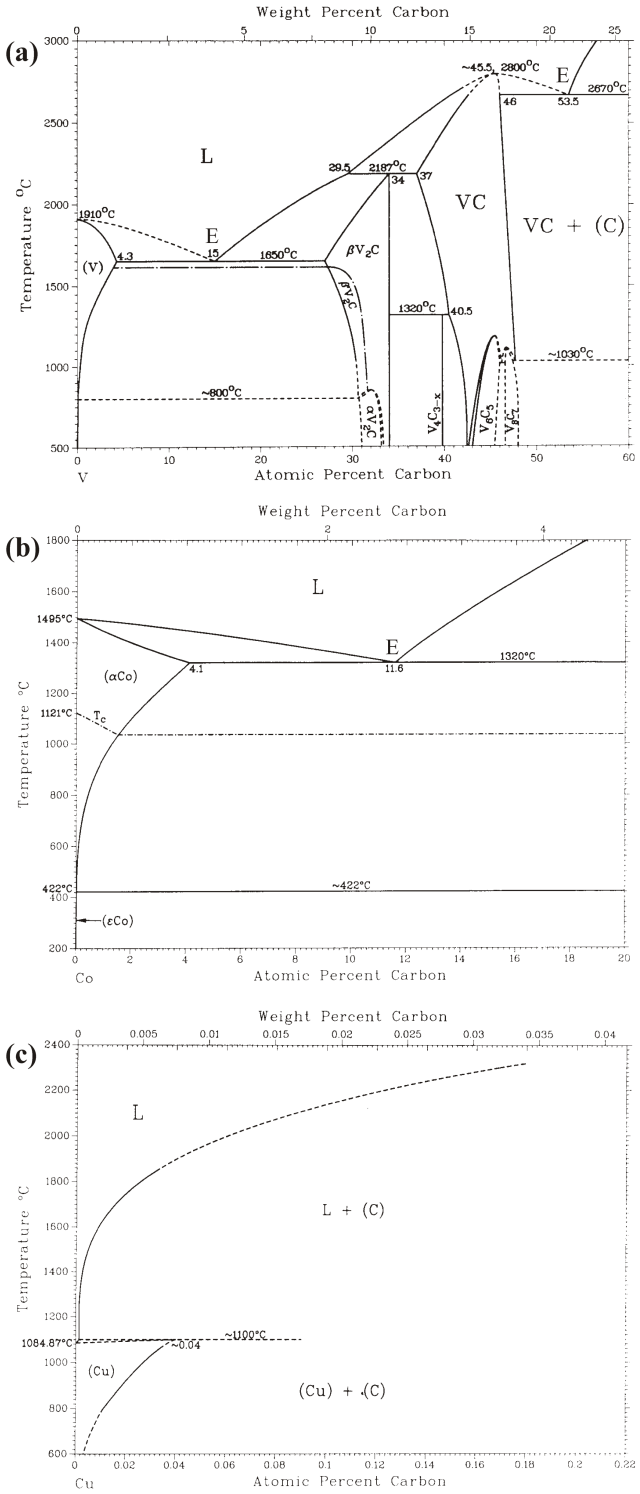

Figure 2.7: Binary phase diagrams of carbon-vanadium (a), carbon-cobalt (b) and carbon-copper (c) [35]. Solid lines denote experimental data, while dashed lines were derived from thermodynamic modeling. The eutectic point E is also indicated in the phase diagrams.

of the high-temperature form of V_2C differs in terms of space group symmetry in comparison to the C-rich high temperature form. On this basis, the C-rich part of the high-temperature region is labeled βV_2C, and the V-rich part is labeled $\beta' V_2C$. The β and β' phases exhibit a hexagonal crystal structure and their V sublattices are identical [35]. In contrast, VC exhibits a fcc (face-centered cubic) crystal structure which is of rock salt, NaCl, structural type.

The phase diagram for the system carbon-cobalt which is shown in figure 2.7 (b) is attributed to eutectic systems (figure 2.6 (b)). Liquid (L) with the eutectic composition of 11.6 at.% Co solidifies at the eutectic temperature of 1320°C to form a mixture of the two solid phases (αCo) and graphite. (αCo) exhibits a face-centered cubic (fcc) crystal structure and is therefore also referred to as fcc Co. In addition, at 421.5°C the (αCo) solid solution transforms into (ϵCo) and graphite by an eutectoid reaction [71]. The crystal structure of (ϵCo) is hexagonal closed-packed (hcp), therefore also labeled hcp Co. The solubility of C in the (ϵCo) phase at the eutectoid temperature is estimated to be 8.74×10^{-4}at.%C [72]. The Curie temperature T_C of the (αCo) solid solution, which is additionally shown in the phase diagram, decreases by the addition of C. Besides, three kinds of metastable cobalt carbides are reported in the literature [33, 72]: orthorhombic Co_3C, orthorhombic Co_2C and hexagonal $Co_{2-3}C$, which is also referred to as (ϵ'Co). These metastable phases in the Co-C system are known to be unstable at temperatures higher than about 300-420°C and transform into stable metallic cobalt and graphite phases [6, 22, 25, 33, 73]. Furthermore, another metastable cobalt carbide phase, named δ'-Co_2C, has been reported by Konno et al. [33], whose structure is a derivative of the δ-Co_2C or simply Co_2C structure. Orthorhombic cobalt carbide and hcp cobalt also can coexist, which is known as the MS II phase [22, 33].

The phase diagram for the system carbon-copper which is shown in figure 2.7 (c) represents a peritectic system (figure 2.6 (c)). The Cu-C system is based on the review of the experimental data of Ruff, Bever and McLellan [74–76] and was obtained by thermodynamic modeling. Solid lines denote experimental data, while dashed lines were derived from modeling. Solid Cu is formed by a peritectic reaction, L+(C) $\rightarrow$ (Cu), with the peritectic horizontal lying at a temperature of $\sim$1100°C, which is just above the melting point of Cu. Copper exhibits a fcc crystal structure. The solubility of C in the (Cu) solid solution at the peritectic temperature is about 0.04 at.%. For higher Cu contents two solid solutions exist, which are Cu and graphite (C), whereby the latter exhibits no reported solubility of Cu [35]. In addition, the preparation of the compounds Cu_2C_2 and CuC_2 was also reported [77]. These compounds were termed copper acetylides, because they result from the substitution of Cu for the hydrogen atoms of acetylen. Both compounds were reported to be very unstable [77].

2.5 Growth mechanisms of single- and multicomponent films

Film synthesis by low-temperature PVD generally takes place far from thermodynamic equilibrium. Microstructure during deposition therefore typically evolves in a competitive fashion and the kinetic limitations induced by low-temperature growth allow the controlled synthesis of metastable phases and artificial structures like multilayers and nanophase materials [78]. The growth processes which control microstructural evolution include nucleation, island growth, coalescence of islands, formation of a connected network with polycrystalline islands and channels, development of a continuous structure based on filling and shrinking of channels, and film growth [2, 78, 79]. These film growth processes depend on the type of atoms and the growth conditions such as substrate temperature, deposition rate, pressure during deposition and energy of incoming particles [2, 78, 80, 81]. Surface and bulk diffusion are the determining atomic processes controlling structure evolution. These processes are mainly affected by the substrate temperature and energetic particle bombardment which can be used to manipulate adatom mobilities and nucleation rates. The presence of alloying elements or impurities and their segregation to surfaces and grain boundaries can strongly influence the film morphology.

Figure 2.8 illustrates the atomic processes which take place on solid surfaces at vapor deposition. Atoms arrive on the surface with the rate R and depending on the value of their diffusion energy E_d, they start to move over the surface. During this process they can encounter other adatoms and form small clusters with the binding energy E_b [83] or attach to already existing clusters. Besides, nucleation kinetics is affected by the crystal structure of the substrate material, lattice defects, surface steps and surface contamination [78]. Diffusion of atoms and nucleation give rise to three basic growth modes [2, 82, 84] which are shown schematically in figure 2.9. These growth modes are distinguished in terms of surface and interface energies [82]. The Volmer-Weber mode describes 3D island growth and occurs when the adatoms are more strongly bound to each other than they are to the substrate. In the opposite case, where the adatoms are more strongly attracted by the substrate than by themselves, layer-by-layer or Frank-van der Merwe growth arises. The layer-plus-island or Stranski-Krastanov growth mechanism is an intermediate case of the preceding two modes. After the formation of

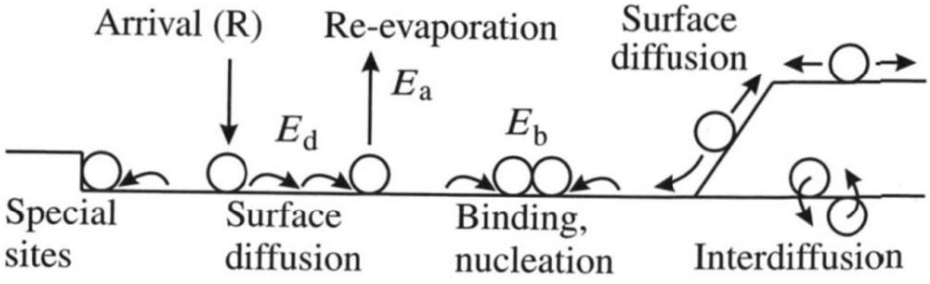

Figure 2.8: Schematic view of possible atomic processes on solid surfaces [82].

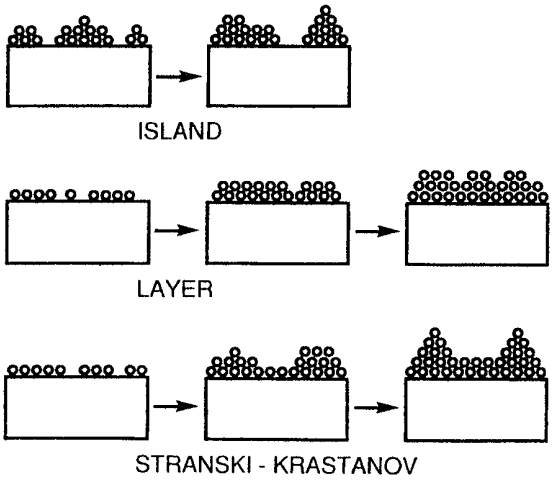

Figure 2.9: Schematic representation of the three basic modes of thin-film growth [2].

one or more monolayers, subsequent layer growth becomes unfavorable and islands are formed. As can be seen from figure 2.8, other atomistic processes like re-evaporation and interdiffusion occur during deposition.

The density of stable nuclei increases with time up to some maximum and then decreases due to coalescence of islands. During island coalescence, there is a strong driving force for coarsening through surface diffusion and grain boundary migration [78] in order to minimize the total surface and interface energy. Dependent on temperature and island size, coarsening can be very fast. This process is then termed liquid-like coalescence, which occurs either by rapid surface diffusion or by melting (for materials with a low melting point) of contacting islands in order to release surface and edge energy [78]. The presence of facets is an indication that liquid-like coalescence has occurred. Grain coarsening during coalescence of the contacting crystals is repeated until the local grain size becomes sufficiently large that grain boundaries are immobile. Another phenomenon of grain coarsening is Ostwald ripening, whereby large clusters grow at the expense of smaller ones without direct contact [2].

Extensive studies of the correlation between film structure and deposition parameters have been carried out over the past five decades leading to the development and refinement of so-called structure zone models (SZMs). These models systematically classify the structural evolution during physical vapor deposition in dependence of film growth parameters [2, 78, 80, 85–88].

The earliest of the SZMs was proposed by Movchan and Demchishin [85] in 1969. They observed that the microstructural evolution of evaporated metal and oxide coatings can be systematically represented as a function of the homologous temperature T/T_m, with T being the substrate temperature and T_m the melting point of the condensate. In subsequent years parts of existing structure zone diagrams have been revised and new variables have been suggested in order to create new SZMs for different deposition techniques and material systems [2]. An example of a refined SZM characterizing

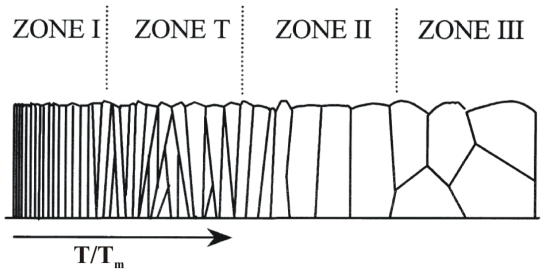

Figure 2.10: Revised structure zone model representing microstructural evolution during pure elemental film growth [81]. The zone T competitive grain growth is clearly visible.

microstructural evolution in pure elemental films is shown in figure 2.10. During film growth in the low temperature zone I regime nucleation dominates the film morphology and the film is composed of fibers of small diameter (1-10 nm). This structure belongs to the temperature interval $0 < T/T_m < 0.2$, where neither surface nor bulk diffusion are significant. In the transition zone T competitive grain growth takes place resulting in an inhomogeneous structure along the film thickness [78, 81]. Near the substrate, a fine-grained structure exists out of which V-shaped columns with the favored orientations slowly emerge and overgrow columns which are less preferred in terms of kinetic growth processes and/or, e.g., surface energy or internal stress. The upper part of thick films can be columnar. This zone belongs to the temperature interval $0.2 < T/T_m < 0.4$ in which surface self diffusion is remarkable, while grain boundary migration is strongly limited. In zone II grain growth additionally occurs by bulk diffusion through grain boundary migration in lateral directions in order to reduce interface and surface energy. The film is composed of columns penetrating from the bottom to the top of the film, whereby grain boundaries are nearly perpendicular to the film plane. This zone is characteristic for high substrate temperatures ($T/T_m > 0.4$). Zone III structures are characterized by equiaxed (globular) grains indicating that the crystal growth has been blocked periodically. This kind of structure is generally attributed to the high temperature range. However, as will be shown below, the development of this film morphology can be based on the presence of inhibitors and can exist at every substrate temperature with different grain sizes [81].

It is generally agreed that surface and bulk diffusion are the most determinant atomic processes of the structure evolution. However, there might be other significant influences. Co-deposition of active impurities such as water vapor, hydrocarbons and oxygen, is hardly avoidable. These unintentionally incorporated atmospheric contaminants may modify the conventional film structures even at very low concentrations and lead to the development of peculiar structural features [81]. It should be noted that the intentional co-deposition of dopants beyond their solubility limit or alloying elements above the required stoichiometry have similar effects on the structure evolution as active impurities. Besides, these additives may enhance the thermal and process stability of thin films [78].

Following this, extended SZMs have to consider the process-induced segregation of

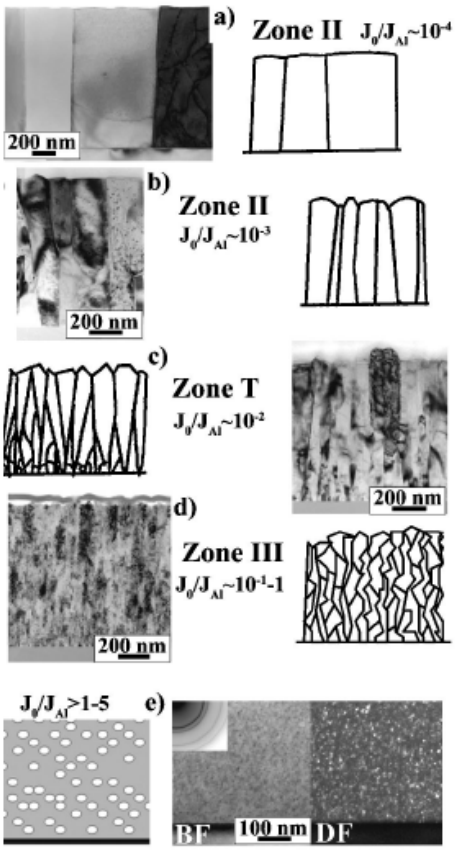

Figure 2.11: TEM images with corresponding schematic diagrams showing the microstructure of Al films deposited by thermal evaporation on amorphous SiO_2 at room temperature as a function of incident O and Al flux ratio J_O/J_{Al} [78, 81].

co-deposited impurity (additive) species, with the aim to represent the temperature dependent structures at various levels of impurity concentrations [81]. Figure 2.11 illustrates the changes of the structure and orientation of oxygen containing aluminum films deposited at room temperature, which corresponds to zone II in the basic SZM, as a function of increasing oxygen concentration. Oxygen exhibits a low solubility in Al and segregates to surfaces and grain boundaries which greatly reduces the surface mobility of Al atoms and also the grain boundary mobility. At very low oxygen concentration (figure 2.11 (a)) the grain growth in the coalescence stage is not limited remarkably and the zone II columnar structure develops. The width of columns decreases with increasing oxygen concentration due to its segregation to grain boundaries (figure 2.11 (b)). The resulting texture is still zone II, but with less degree of preferred orientation of the grains. At higher oxygen concentrations (figure 2.11 (c)), the grain growth is limited already at the coalescence stage and the zone T competitive grain structure develops [78, 81]. When the oxygen concentration further increases, the epitaxial growth of individual crystals is periodically interrupted by the formation of an oxygen layer which completely covers the crystal surface. The formation of a surface covering layer, sometimes referred to as covering growth, causes repeated nucleation [89]. The composite film is composed of three dimensional equiaxed (globular) grains with random orientation separated by an amorphous aluminum oxide tissue phase ac-

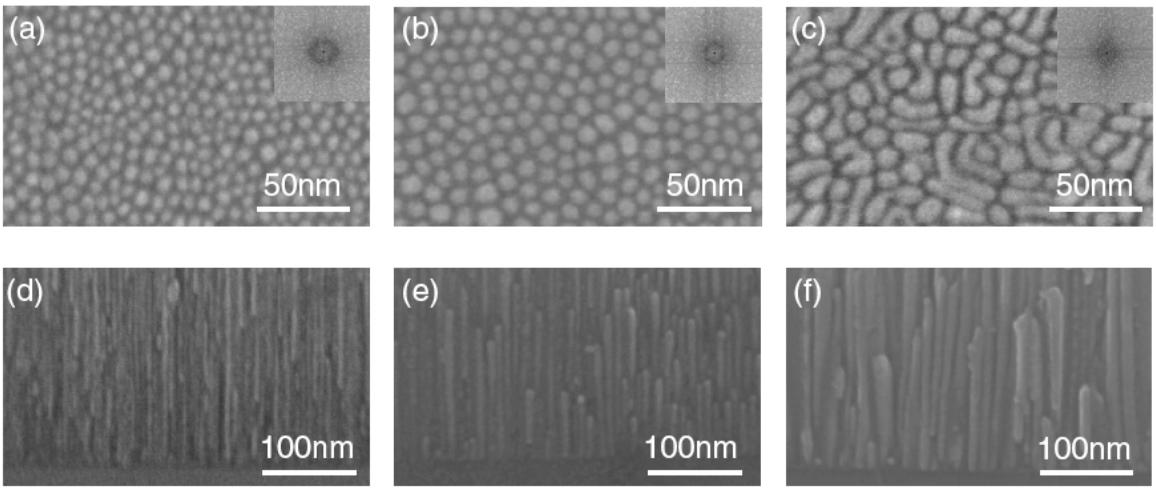

Figure 2.12: Plan-view and cross-sectional SEM images of phase separated Al-Si films prepared at deposition rates of 5.5 ((a) and (d)), 2.7 ((b) and (e)), and 1.0 nm/s ((c) and (f)) [92].

cording to zone III (figure 2.11 (d)). As the oxygen concentration is further increased above the Al concentration (J_O/J_{Al} >1-5), the role of oxide and metal phases is reversed and the film is composed of metallic grains dispersed in an oxide matrix. At even higher oxygen concentrations amorphous aluminum oxide films are formed. Besides, additives or impurities can not only inhibit but also promote the structure evolution during physical vapor deposition [78]. For example, the addition of Sn to Al promotes the formation of larger grains [90] in contrast to O and Pt [91] which decrease the initial grain size. This presents new possibilities for the controlled formation of micro- and nanostructures [81].

From the above explanations it follows that the morphology of binary films is significantly more complex than for single component films. In systems with limited solid solubility of the film components A and B phase separation can occur. Phase diagrams of binary systems which induce a phase separation are of the eutectic and peritectic type. Surface diffusion of the different atomic species occurring during the deposition process is responsible for the phase separation into dispersed phase and matrix [93]. The interplay of surface diffusion and growth rate influences the film morphology [92, 93]. The former feature is associated with the fact that activation energies for surface diffusion are typically by at least a factor of two smaller than those for bulk diffusion [93] and the deposition is most often performed at low temperatures (relative to the melting point of the compound). Besides, adatom mobilities depend in addition to the substrate temperature on the type of diffusing atoms and differ over surfaces of different phases [2]. On the other hand, the externally imposed deposition rate causes that the surface is constantly buried and incorporated into the bulk. Figures 2.12 (a)-(f) show plan-view and cross-sectional scanning electron microscopy (SEM) images of Al-Si films prepared at different deposition rates. In these SEM images, the bright parts indicate Al-rich columnar structures and the dark areas are amorphous Si matrixes including a small amount of Al. The images clearly show that the grain size,

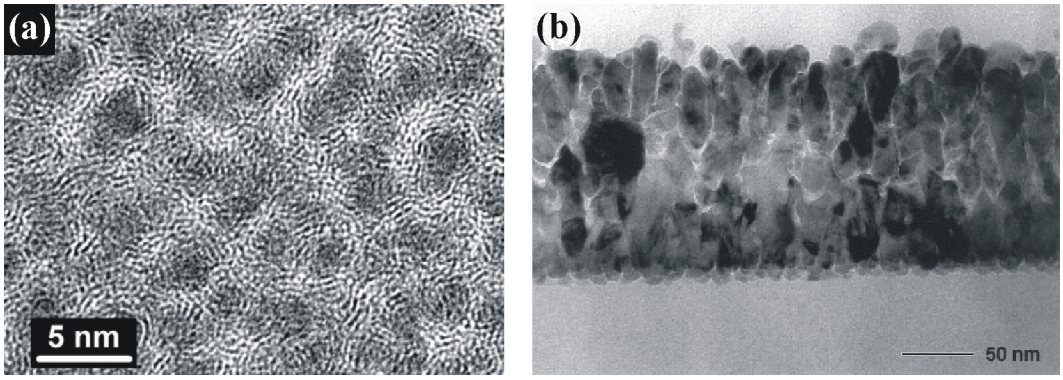

Figure 2.13: (a) Plan-view HRTEM image of a C:Fe film grown at 300°C. Iron-rich particles are encapsulated by graphite-like carbon layers [23]. (b) Cross-sectional TEM image of a C:Co film grown at 400°C [25].

shape, and elongation are influenced by the surface diffusion length. The observations are consistent with a three-dimensional simulation of phase separation in binary thin films using a modified Cahn-Hilliard equation [92, 94, 95]. Numerous simulation studies on the morphology during thin film growth of phase separated systems have been performed to understand the growth mechanism and it has been shown that different nanoscale compositional patterns can be formed which are controlled by the deposition conditions and film compositions [92–94, 96, 97].

2.6 Carbon:transition metal nanocomposites

The granular morphology of carbon:transition metal nanocomposite films is generally obtained via co-deposition of carbon and a TM, which are either nonmiscible or exhibit a limited mutual solid solubility. Ion beam sputtering [4, 10, 20, 22], magnetron sputtering [5, 17, 18, 25], pulsed filtered cathodic vacuum arc deposition [6, 9], pulsed laser deposition [16, 27], and plasma-assisted chemical vapor deposition [28–31] have been reported to be able in producing such encapsulated structures. Surface diffusion assisted phase separation which occurs during thin film growth of the two components with limited miscibility results in the formation of metallic or carbidic nanoparticles dispersed in the carbon matrix (figure 2.13). A large variety of C:TM nanocomposites has been synthesized employing transition metals which exhibit a different chemical affinity to carbon. Some of them form very stable carbides (e.g. Ti, V, W, Zr) [15, 16, 27, 32, 98–100], while others are practically immiscible with carbon (e.g. Ag, Cu) [10, 14, 23, 24]. Weak carbides formers (e.g. Fe, Co, Ni) exhibit a moderate but nevertheless considerable affinity to carbon which results in the formation of metastable carbides [20, 22, 25, 101, 102]. In dependence of the deposition conditions, the shape of nanoparticles can vary between nanocolumns with a height similar to the film thickness [103, 104], elongated [10, 17, 18, 20, 25, 32] and globular particles [17, 18]. The embedding carbon matrix can be amorphous [6, 16, 18, 23], graphite-like with graphene layers curved into a cylindrical shape encapsulating nanocolumns or elongated nanoparticles

[6, 10, 18, 20, 23, 25], and fullerene-like (FL) with a spherical-like curvature encapsulating globular nanoparticles [17, 18]. The following subsections give a brief literature overview on the structural investigations of C:V, C:Co and C:Cu nanocomposite films which will be studied in this work.

2.6.1 C:V nanocomposite films

Although there is a growing interest in the use of hard transition metal carbides and nitrides as functional coatings [105, 106], very few studies exist about the structural characterization of films and coatings in the vanadium-carbon system. In 1992, the microstructure of thick (8-10 μm) V-C coatings deposited by reactive dc magnetron sputtering of a vanadium carbide target in an Ar-C_2H_2 mixture has been investigated [99]. The carbon concentration in the films was adjusted by the acetylene gas flow ranging from 47-73 at.%. The substrate temperature was about 300°C at the beginning of the deposition and decreased exponentially to ∼180°C at the end of the deposition. X-ray diffraction and selected area electron diffraction revealed that the nanoparticles are of the vanadium carbide fcc phase. Cross-sectional dark-field TEM imaging showed the presence of elongated grains for the films with a low carbon content (∼50 at.%) while with increasing carbon concentration the grain size decreased and the shape changed to a globular structure. Recently, Aouni et al. [98] investigated the structure of C:V films over a wide range of carbon concentration between 1 and 69 at.%. The films were deposited at RT by reactive dc magnetron sputtering of a vanadium target in an Ar-CH_4 mixture. XRD measurements showed that the structure of the dispersed phase strongly depends on the carbon content. Up to 17 at.% carbon, the films are composed of the bcc vanadium solid solution supersaturated with carbon, and for carbon concentrations above 32 at.% the fcc VC structure is present. In between these values the β-V_2C phase is present. The studies by the above presented groups only addressed the characterization of the dispersed phase, while no investigation on the carbon phase has been done.

Recently, the influence of vanadium on the carbon bonding structure in C:V composites during thin film growth and subsequent annealing was investigated by Raman spectroscopy [100]. The films were deposited at RT by dual magnetron sputtering containing between 1.5 and 19 at.% V. The samples were postannealed at temperatures in the range of 700-1300 K. The study showed that the addition of the metal during film growth enhances the formation of sixfold ring (graphitic) clusters in comparison to pure carbon films, while postannealing results in carbide crystallite formation and growth which destroys the initial carbon structure and reduces the aromatic cluster size.

2.6.2 C:Co nanocomposite films

In 1994 Konno and Sinclair provided a detailed description of the structural evolution of annealed C:Co films prepared by magnetron sputtering at RT describing the crystallization behavior of amorphous Co-C alloys by in situ transmission electron microscopy and differential scanning calorimetry [33]. The films had a carbon content between 5 and 95 at.% and were annealed up to 500°C. For the films containing less than 40 at.% carbon metastable cobalt carbide was formed by annealing at 250-350°C. Upon further annealing at 380-420°C the carbide phase decomposed into hcp cobalt and graphite-like carbon. For alloys with more than 40 at.% carbon the carbon phase remained amorphous.

Two years later Hayashi et al. reported about the structure of C:Co composites grown by ion beam sputtering at 200°C with carbon concentrations of 40-60 at.% which were subsequently annealed at temperatures between 250 and 350°C [4]. The as-grown films exhibit an amorphous structure while annealing resulted in the transformation into crystalline cobalt particles encapsulated in graphite-like carbon as shown by TEM.

Stimulated by this work many investigations on C:Co composites were based on the structural characterization employing XRD and TEM, and their magnetic properties in order to establish structure-property relationship. Delaunay et al. studied the structure of C:Co films prepared by ion beam sputtering at elevated substrate temperatures (100-300°C) with carbon contents of 27-57 at.% and by postdeposition annealing at 300-400°C [22, 107]. For the films with 57 at.% carbon grown at 200°C metallic cobalt grains embedded in graphite-like carbon were obtained. For the films with lower carbon content the matrix was amorphous. Postdeposition annealing above 300°C also resulted in the formation of graphite-like carbon encapsulating the metallic nanoparticles in these films. Besides, the MS II phase which is composed of an orthorhombic cobalt carbide and hcp Co phase was found in the films with low carbon content ($\leq$ 36 at.%) grown at 100 and 200°C. The metastable cobalt carbide decomposed upon annealing into hcp Co and graphite-like carbon.

The formation of metastable cobalt carbide has also been reported by annealing amorphous Co-C alloys grown at RT by magnetron sputtering [5] or pulsed filtered vacuum arc deposition [6, 101, 108] at annealing temperatures (dependent on composition) between 250 and 350°C as shown by XRD or TEM. The Co concentration was in the range of 44-80 at.%. Upon further annealing between 350 and 400°C the metastable carbide phase decomposed into hcp Co and graphite-like carbon. Mi et al. also investigated the structural modification of C:Co films grown by magnetron sputtering at RT with Co contents of 30-40 at.% [26]. Annealing at 300-450°C caused the crystallization of amorphous cobalt, the increase in grain size and the graphitization of the carbon matrix. The coexistence of hcp and fcc Co at 450°C which is higher than the phase transformation point of 425°C is reported. In contrast, for C:Co films with a Co concentration between 18 and 39 at.% grown by pulsed filtered vacuum arc the carbon phase remained amorphous after annealing at 400°C [9].

Konno and Sinclair [25] investigated the structure of C:Co films grown by magnetron sputtering at temperatures in the range of 200-400°C with carbon contents of 38-62 at.%. TEM analysis showed that the grain size depends on the substrate temperature and film composition. Up to 300°C the films are composed of amorphous cobalt carbide and graphite-like carbon while at higher temperatures metallic Co is present. Besides, cross-sectional TEM imaging revealed the columnar structure of the grains and their three dimensional separation by graphite-like carbon layers (figure 2.13 (b)).

In Ref. [104] the microstructural evolution of Co nanoparticles encapsulated in a diamond-like carbon matrix synthesized at RT by plasma-assisted magnetron sputtering in an Ar/CH_4 gas mixture is reported. A bias voltage of -500 V was applied during the deposition and the Co content in films was 35-78 at.%. With increasing Co content the nanostructure develops from slightly elongated nanoparticles to self-assembled nanorods with a height equal to the film thickness as shown by cross-sectional TEM. The Co grains exhibit an amorphous-like structure. During annealing by electron beam radiation the Co grain structure was transformed to a crystalline structure (ϵ-Co) and also the amorphous DLC matrix transformed to graphite-like carbon [109].

Raman spectroscopy has been employed to study the structural modification of the carbon matrix in annealed C:Co composites grown at RT by pulsed filtered vacuum arc deposition [6, 9]. The Co content in the films was between 18 and 70 at.% and annealing was carried out at temperatures up to 500°C. It has been shown that for Co-rich films (60-70 at.% Co) carbon graphitization occurs at lower annealing temperatures of around 400°C. The observed tendency is similar to the crystallization behavior of amorphous carbon in a-C/Co/a-C trilayer thin films upon annealing [110]. The films were prepared by dc magnetron sputtering at RT with a Co layer thickness of 7-21 nm and a C layer thickness of 65 nm, respectively. In situ and ex situ TEM showed that a-C in contact with cobalt transforms into polycrystalline graphite upon heating above 500°C, which was further confirmed by Raman spectroscopy. Differential scanning calorimetry revealed that the graphitization occurred at lower annealing temperatures for the films with the thicker Co interlayer.

2.6.3 C:Cu nanocomposite films

Cabioc'h et al. published in 1999 a detailed study on the microstructure of C:Cu thin films [24]. The films were grown by ion beam sputtering at substrate temperatures in the range of -200-600°C with atomic carbon concentrations varying from 16 to 96 %. TEM observations revealed the presence of copper nanoparticles homogeneously distributed in the carbon matrix. The formation of graphene layers encapsulating the copper precipitates occurred for the films grown at RT if the Cu content was above 55 at.% and for all the films synthesized at 300°C independently of the Cu concentration which demonstrated the strong catalytic effect of copper on low temperature graphitziation of carbon during the deposition. The nanoparticles exhibit an elongated shape in the direction of the thin film growth as shown by grazing incidence small angle X-ray

scattering (GISAXS).

Many studies were based on the structural characterization of copper/hydrogenated amorphous carbon composite films grown by a hybrid technique combining microwave plasma-assisted chemical vapor deposition from methane-argon or acetylene-argon gas mixtures [28–31]. The carbon content in the films was varied in the range of 20-75 at.% for the former gas mixture and between 7.5 and 99 at.% for the latter. X-ray diffraction revealed the presence of fcc Cu phase as well as a decrease in the copper grain size with increasing carbon content in the films. Besides, the microstructure of copper crystallites is also dependent on the hydrocarbon gas precursor as determined by GISAXS measurements [28]. Raman spectroscopy revealed that the size of graphitic carbon clusters depends on the carbon content in the films and the gas precursor [111].

Recently, the structure of a-C/Cu composite films deposited by dc magnetron sputtering has been investigated [112]. The films were grown in the temperature range of RT-500°C, with Cu contents of 20 and 55 at.%, applying different substrate bias from floating potential to -200 V. XRD measurements revealed an increase in the size of Cu crystallites with Cu content in the films and negative substrate bias voltage.

Onoprienko et al. [113] reported in a recent study that C:Cu films deposited by dc magnetron sputtering at RT with a Cu content of 8 at.% are amorphous with copper atoms uniformly distributed over the film volume. Postdeposition annealing at 600°C resulted in the precipitation of copper particles within the film and the increase in grain size with annealing time due to coalescence. The coalescence occurred by the mixed mechanism of bulk and surface diffusion of Cu.

3 Film deposition and annealing

3.1 Ion beam sputter deposition

Ion beam sputtering (IBS) was used for the deposition of carbon:transition metal (C:TM) nanocomposite thin films. Despite of its simplicity this technique provides a high and independent control over the synthesis parameters ion type, ion flux and energy as well as substrate temperature. Thus, it is suitable for fundamental research, but suffers from a low film growth rate. For the sputtering process a Kaufman-type ion beam source [114–116], which is shown in figure 3.1, was used. This source consists of a plasma ignited in a closed volume. The plasma is sustained by a dc discharge. On one side of the closed volume are two grids, a screen grid and an accelerator grid. The inner grid is on cathode potential. Therefore the ions are extracted from the source and accelerated. The second grid, which is on a negative potential, further accelerates the ions and is responsible for the formation of a broad beam with a low divergence. Figure 3.2 shows the potential shape inside and outside the source. The plasma inside the source is close to anode potential. Because of the positive bias of the source, the ions have energy with respect to ground, and thus can be used to sputter targets which are either grounded or on floating potential. In the latter case, an electron-emitting filament called neutralizer is used to limit the charge buildup at the target.

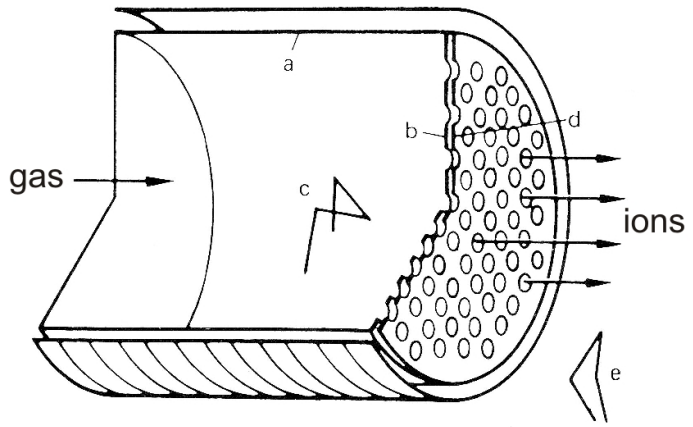

Figure 3.1: Kaufman broad-beam ion source: (a) anode, (b) screen grid, (c) cathode, (d) accelerator grid, (e) neutralizer [114].

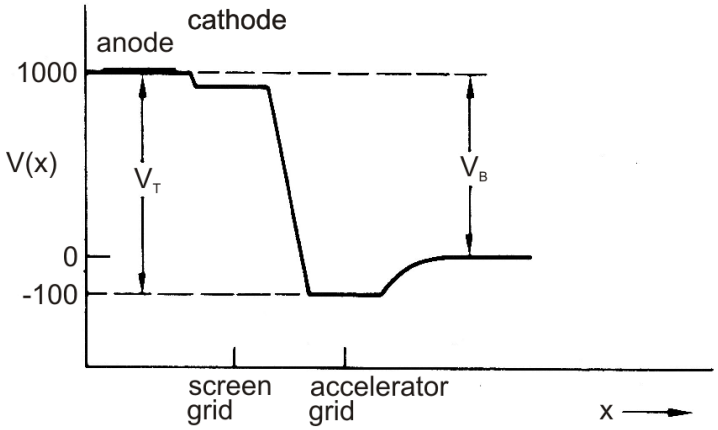

Figure 3.2: Potential shape V(x) inside and outside the source [114]. x-direction corresponds to axial direction. V_T total voltage, V_B beam voltage.

3.2 Experimental set up

The deposition chamber that was used in this work is schematically shown in figure 3.3. A 3 cm Kaufman-type ion source as described above generates an Ar ion beam which is directed toward a 6 inch (or 4 inch) pyrolitic graphite target (99.99% purity) at a distance of ∼18 cm. The ions impinged at an angle of 23° with respect to the target normal. A metal stripe made of vanadium (99.9% purity), cobalt (99.9% purity) or copper (99.99% purity) is attached on the graphite target with a length slightly exceeding the target diameter. In this way, carbon and the metal are sputtered simultaneously. The metal content in the growing film was adjusted by the width of the stripe. The Co atomic ratio in the films is found to be ∼15, ∼30, and ∼40 at.% for the depositions performed with Co stripe widths of 2.8, 4, and 5.5 mm on the graphite target, respectively. These approximate TM atomic fraction will be used in the following for the denotation of the samples. For Cu, a stripe width of 1.4 and 3.3 mm results in a TM content of ∼15 and ∼30 at.%. Similar metal contents are obtained for V employing a stripe width of 2.3 and 7.3 mm, respectively. The VC reference films were grown using a V stripe 14.6 mm in width. The deposition chamber was evacuated by a turbo-molecular pump to a base pressure below $4x10^{-5}$ Pa, except for C and VC films (p=6-$9x10^{-5}$ Pa). Prior to the experiments, the chamber walls and the substrate holder were heated for at least 3 hours in order to promote the removal of weakly bonded adsorption layers (water vapor, hydrocarbons and oxygen). The chamber walls were heated to approximately 80°C by employing a heating cable which was wound around the chamber. The substrate holder was warmed-up to 400°C in order to enhance the desorption of atmospheric contaminants from the water-cooled surface. The argon feed gas (99.999999 % purity) was introduced through a mass flow controller and the argon flux was adjusted in order to achieve a gas pressure during sputter deposition of $\sim 7.5x10^{-3}$ Pa. The total ion beam sputtering current and energy were kept constant at 40±1 mA and 1 keV, respectively. The substrates were located on a substrate holder facing the target at a distance of ∼14 cm and were heated with

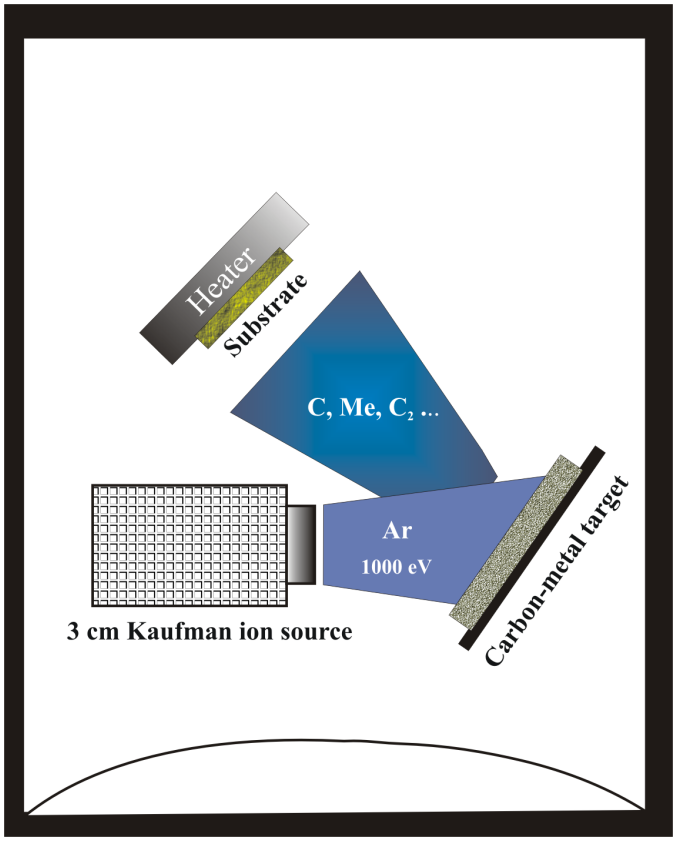

Figure 3.3: Schematic view of the ion beam sputtering deposition system.

a boron nitride heater placed on the backside of the substrate holder. The substrate temperature (T_s) was monitored by a thermocouple, which was in contact with the substrate holder having a similar temperature as the substrate. Before each deposition, the target was pre-sputtered for 15 min. A shutter, placed in front of the sample, was then removed without interruption of the sputtering process and the depositions were performed for 60 min, resulting in a film thickness of ∼100 nm. The films were grown on the substrate in a temperature range of RT-500°C. It should be noted that for the thin films grown without additional heating the sample temperature increased slowly during the experiments and reached a value of ∼45°C at the end of the deposition process. In the following, these samples will be denoted for simplicity reasons as grown at RT. For comparative analysis, a series of samples was deposited at identical conditions but without the metal stripe on the graphite target, termed carbon reference films in the following text. C and C:TM films were deposited on thermally grown SiO_2 (∼500 nm) on Si substrates, in order to avoid metal loss due to inward diffusion at higher temperatures (>200°C) [117]. For TEM observations, predominantly thinner films were grown with a thickness between 20 and 50 nm.

For annealing experiments C and C:TM films were deposited at a substrate temperature of 200°C. Post-deposition annealing of the samples in the temperature range of 300-700°C was performed with a boron nitride heater in a vacuum furnace with a base pressure below $4x10^{-4}$ Pa and a pressure during annealing of less than $2x10^{-3}$ Pa.

The desired annealing temperature (T_a) was reached in less than 5 min and then kept constant for 60 min. The temperature was controlled with a thermocouple, which was in contact with the sample holder.

4 Film characterization

In order to obtain a closer understanding of the nanostructural evolution during the growth of C:TM films and the structural changes upon post-deposition annealing, it is required to combine techniques which are capable to characterize both constituents of the nanocomposite - dispersed phase and the matrix. The complementary analysis of both phases demands the use of a set of analysis techniques. The dispersed phase was investigated by X-ray diffraction (XRD) and transmission electron microscopy (TEM) in combination with selected area electron diffraction (SAED). The carbon matrix was studied employing TEM and Raman spectroscopy. The film composition and depth profiles were obtained by elastic recoil detection analysis (ERDA).

4.1 Elastic recoil detection analysis

The carbon and transition metal contents of the C:TM films, the contamination by the light elements H, N and O, and the depth profiles of the atomic ratio of the film constituents were determined by elastic recoil detection analysis. ERDA is based on the detection of atoms that are elastically scattered out of the thin film exposed to an ion beam. The measurements were performed with 35 MeV Cl^{7+} ions impinging at an angle of 15° relative to the film surface. The elastically recoiled target atoms were detected with a Bragg ionization chamber placed at a scattering angle of 31°. The Bragg detector allows to identify the atomic number Z and the energy of the recoils, the latter being related to its escape depth. The error of measurement is ∼1 at.% for elemental concentrations above 10 at.% and approximately 10% for lower concentrations. The depth resolution is 10-15 nm for heavy elements and 15-20 nm for light elements such as C, N and O. Hydrogen was detected with a separate standard Si solid barrier detector (Canberra) at a scattering angle of 38°. In this case, an aluminum foil was employed to stop heavier recoils and backscattered Cl^{7+} ions. The depth resolution for H is about 80 nm. Therefore the profile seems to extend above the surface and changes only gradually. Quantitative concentration spectra as a function of the depth profiles are achieved by fitting the measured spectra with a layer model using the software NDF. Details of the experimental set up and analysis of the elemental depth profiles are given in [118, 119].

4.2 X-ray diffraction

The crystalline structure of the nanoparticles was investigated by X-ray diffraction. During X-ray diffraction the X-rays impinge on a set of atomic planes with distance d at an angle Θ with them. The X-rays are diffracted on the atomic planes and interfere with each other. Constructive interference will occur, when the scattering waves come out in phase. This will happen if the phase shift between two adjacent beams is $n\lambda$. From the position of diffraction peaks in the XRD patterns the lattice distances can be calculated according to Bragg's law [120]:

$$n\lambda = 2dsin\Theta, \tag{4.1}$$

where n is the order of a diffraction.

From the full width at half maximum (FWHM) B of diffraction peaks the crystallite size t can be estimated employing the Scherrer equation [121]:

$$t = \frac{K\lambda}{B\ cos\Theta}, \tag{4.2}$$

where B is measured in radian (rad). Note that whether a value of K = 0.9 or 1 is used depends on the shape(s) of the crystallites assumed to be in the sample. The additional broadening in diffraction peaks beyond the inherent peak widths due to instrumental effects has to be considered. A second cause of broadening due to stress in the films can complicate the estimation of the crystallite size [120].

A most common technique for analyzing thin films is grazing incidence diffraction (GID), also referred to as grazing incidence angle asymmetric Bragg (GIAB) geometry [122–124]. Figure 4.1 compares the grazing incidence angle geometry used for thin films with the more common $\Theta/2\Theta$ or Bragg-Brentano geometry used for bulk analysis. In the conventional symmetric Bragg-Brentano geometry, a parafocusing arrangement is used where the X-ray source and the detector are at the focal points of the incident and diffracted beams, respectively. On the other hand, the thin film arrangement exhibits an asymmetric geometry. The incident and diffracted beams are made nearly parallel by means of a narrow slit on the incident beam and a long Soller collimator on the

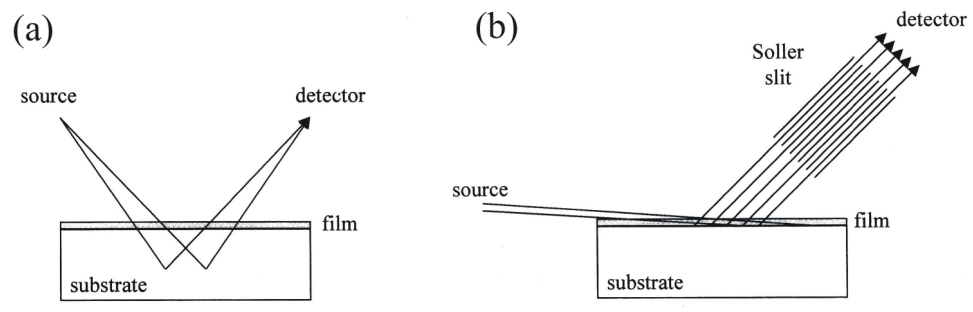

Figure 4.1: Geometries for (a) bulk and (b) thin films analysis [122].

detector side. As the source and the specimen remain fixed during the measurement, the probed area on the sample surface and the penetration depth of the X-ray beam into the specimen are not changed. The incident glancing angle is close to the critical angle for total reflection, which increases the path length of the X-ray beam through the film and decreases the penetration depth in the specimen. This helps to increase the diffracted intensity, while at the same time the diffracted intensity from the substrate is reduced. With regard to the penetration depth, the GID geometry is approximately two orders of magnitude more surface sensitive than the standard $\Theta/2\Theta$ geometry, although it should be remembered that this occurs together with a significant loss in intensity, because of the restricted dimensions of the incident beam, the lower penetration depth and the non-focusing geometry [122].

It should be remarked that the crystallite size obtained employing the Scherrer formula is measured in the direction of the scattering vector. For the Bragg-Brentano geometry the scattering vector is always perpendicular to the sample surface, while for GID it changes with the detector position. This is important in case of elongated crystallites.

The phase structure of the nanoparticles in C:TM thin films was analyzed employing a D5000 (Bruker-AXS) diffractometer with Cu-Kα radiation (λ=0.15406 nm) in grazing incidence geometry. The incident angle was 1° and patterns were measured in the range of 2Θ from 30 to 100° in steps of 0.1°.

4.3 Transmission electron microscopy

The morphology of the C:TM films was investigated by cross-section (cs) and plan-view (pv) transmission electron microscopy (TEM) and high resolution transmission electron microscopy (HRTEM). The combination of pv- and cs-TEM enables the determination of the three-dimensional (3D) size, shape and distribution of the nanoparticles in the carbon matrix.

TEM is based on the absorption and scattering of transmitted electrons. The high resolution in TEM methods is a result of the small wavelengths of the electrons, e.g. electrons of 300 keV energy have a wavelength of 0.022 $\mathring{A}$. Figure 4.2 shows the principle construction of a TEM and illustrates the differences between bright-field (BF) and dark-field imaging (DF). An electron gun emits electrons, which are projected onto the specimen by electromagnetic lenses. When penetrating through the specimen, the electrons are elastically and inelastically scattered. The former gives rise to diffraction patterns. The transmitted electrons pass through a series of postspecimen lenses. The electron beam is magnified by projection lenses and imaged on a detector. As can be seen from figure 4.2, BF-imaging excludes all diffracted beams and only the direct beam is magnified and imaged. This is achieved by placing a suitable sized aperture in the back focal plane of the objective lens. On the other hand, during DF-imaging one of the diffracted beams is chosen by means of an aperture which blocks the direct

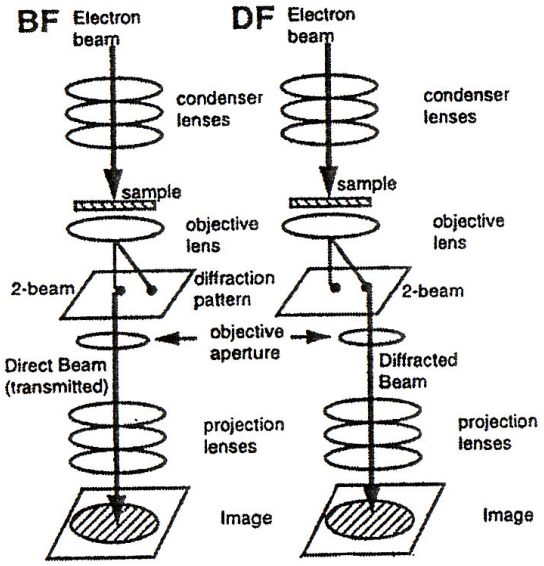

Figure 4.2: Measurement principle of transmission electron microscopes for bright-field (BF) and dark-field (DF) imaging [2].

and the other diffracted beams.

For (HR)TEM imaging a JEOL 3010 300 kV microscope and a FEI Titan 300 kV microscope were used, respectively. In addition, selected area electron diffraction (SAED) patterns were recorded which yield information on the nanoparticle phase and the degree of crystallinity of the matrix and the nanoparticles. Spotted arrays indicate crystalline material, while the presence of diffraction rings of varying sharpness and width indicate about polycrystalline and amorphous materials [2]. In preparation for cs-TEM images two 5 x 5 mm^2 pieces of the sample were glued with the film face together. This sandwich structure is first mechanically thinned and finally sputtered with Ar ions of 1 keV at an angle of incidence of 2° (ion milling). For pv-TEM images the sample is thinned from the backside by stepwise removing the substrate with the procedure described above.

4.4 Raman spectroscopy

4.4.1 Principle of Raman spectroscopy

Raman spectroscopy is a spectroscopic technique used in condensed matter physics and chemistry to study vibrational, rotational and other low-frequency modes of a molecule or solid [125]. It can be described as the inelastic scattering of light by matter, whereby the light is monochromatic and usually comes from a laser in the visible, near infrared or near ultraviolet range. When a photon interacts with a molecule it can be elastically or inelastically scattered. In both cases the molecule will be excited into a virtual state.

If elastic scattering occurs the molecule relaxes back into its ground state by emitting a photon with the same energy as the incoming photon. This type of scattering is known as Rayleigh-scattering. In the case of inelastic scattering the photon gives energy to or removes energy from the molecule. Photons, which undergo inelastic loss of energy give rise to Stokes scattering whilst photons undergoing inelastic gain of energy give rise to anti-Stokes scattering. The energy gained by the molecule in Stokes scattering appears as vibrational energy and where a molecule exhibits excess vibrational energy above the ground state, it is this energy which is lost to the anti-Stokes scattered photons [125]. Generally, the difference in energy is recorded as the difference in wave number between the incoming and the scattered light, which is known as the Raman shift.

Raman spectroscopy is based on the change in polarizability of a molecule or crystal by a phonon [126]. When a molecule is placed in an electric field, its electrons are displaced relative to its nuclei and thus develop an electric dipole moment. A fluctuating electric field will induce a fluctuating dipole, which will emit or scatter radiation of the same frequency. As long as the polarizability is constant with time an incoming electromagnetic wave will propagate straight according to the Huygens principle and elastic scattering occurs [126]. This is no longer the case, if the polarizability is modulated by a vibrational induced change of the inter-atomic distance. In this case the light will be scattered with frequencies ν_0 (Rayleigh scattering) and $\nu_0 \pm \nu_v$ (Raman scattering), where ν_0 is the frequency of the electromagnetic radiation and ν_v is the modulation frequency. In a solid the incoming photon excites an electron from the valence to the conduction band which will undergo some scattering processes before recombining with the hole in the valence band under emission of the scattered photon. If a one-phonon scattering event occurs, it is called a first-order Raman process [127]. The scattering by two phonons with the same frequency or with different frequencies, which are called overtone or combination Raman modes, and the scattering by a phonon and a defect is referred to as a second-order Raman process [127]. For a Raman process energy and momentum conservation are valid. As k_i, the electronic wave vector of the incident light, is in the visible range of the magnitude 10^5 cm^{-1}, the momentum of the light is small when compared with the first Brillouin zone (BZ) [126, 128]. This means the photo-excited electron has to go back to its original k state to recombine with the hole [127]. Due to this restriction only a q≈0 phonon wave vector can be observed in the first-order Raman process, which means a phonon from the center of the BZ. In the second-order process two scattering events with phonon wave vectors q and -q occur. Non-zone center phonon modes (q $\neq$ 0) can therefore be observed in the second order Raman spectra. The Raman effect is an inherently weak effect, typically 10^{-8} of the intensity of the incident laser light [125]. However, if either the excited or the scattered electron is in a real electronic state, the scattered intensity is increased by several orders of magnitude in comparison to conventional Raman spectroscopy [126]. This is know as resonant Raman spectroscopy. In a real electronic state, which is also called an eigenstate, the electrons exhibit a much longer life time than in a virtual state. Accordingly, the Raman cross section and for this reason the scattered intensity is increased [128]. In this work, the Raman spectra were taken under the resonance condition. In the following, resonant Raman spectroscopy will be denoted for simplicity reasons as Raman spectroscopy.

4.4.2 Raman spectroscopy of carbon

Raman spectra are sensitive to the chemical structure and long range order of carbon materials. The Raman spectra of all carbons show several common features in the 800-2100 cm^{-1} region, the so-called G (graphite) and D (disorder-induced) peaks. According to the fundamental selection rule q≈0 [56] only phonon wave vectors from the center (Γ-point) of the BZ are allowed in single crystals. This gives rise to the G mode, situated in the wavenumber range of 1500-1630 cm^{-1}. The G peak is due to the in-plane bond stretching vibrations of all pairs of sp^2 carbon atoms in both ring and chain structures [56]. The D peak around 1350 cm^{-1} is due to the breathing modes of sp^2 carbon atoms in sixfold aromatic rings [56]. For a finite size of the crystallites the fundamental selection rule is relaxed and non-zone center phonons contribute to the Raman spectra. The D peak arises as resonant Raman coupling by a strong enhancement of the Raman cross section of the phonon wave vector q, when it equals the wave vector k of the electronic transition excited by the incident photon. This is known as the quasi selection rule k=q [56] involving phonons from the boundary of the BZ around the K point where the band gap equals the photon energy. The origin of the D peak has been successfully explained by a so-called 'molecular' approach [129, 130] and a solid-state double resonance approach [128, 131]. The former one is based on the lattice dynamics of small aromatic clusters and their Raman spectra. Double resonant Raman scattering can be explained in the following way: The defect-induced Raman process consists of four steps including excitation of an electron-hole pair, inelastic scattering of the electron by a phonon, elastic scattering by a defect, and recombination of the excited electron and the hole by emitting the scattered photon [132]. The second and third step can be interchanged. The process is double resonant if two of the three intermediate states are real states and is therefore much stronger than single resonances due to the large scattering cross-section. The solid-state approach additionally explains the excitation-energy dependence of the D peak, the overtone spectrum and the difference between Stokes and anti-Stokes scattering [128, 132]. The different forms of carbon can be classified according to the D and G mode. In general, depending on the sp^2 and the sp^3 concentration, three classes of disordered and amorphous carbons can be distinguished, namely nanocrystalline graphite (nc-graphite), amorphous carbon (a-C) and tetrahedral amorphous carbon (ta-C) [56]. With decreasing sp^2 content, the chemical bonding structure of carbon phases changes, which allows the characterization of all three classes by their Raman spectra. The D peak is not present in single crystalline graphite [133, 134] or in completely amorphous carbons (ta-C) [42, 135]. For the former, the D peak is absent because the changes in bond length and thus polarizability cancel over the infinite crystal [133], while in ta-C no ring structures are present. The D mode becomes active in the presence of disorder [56, 129, 130, 133, 136], which is related with a finite size of the crystallites. Its intensity is determined by the concentration of defects and the probability of finding a sixfold ring in the cluster [56, 133, 137]. Therefore, the D line is the fingerprint of graphitic carbon structures.

A phenomenological spectra-structure relationship is provided by the three stage model [42, 56] which is shown in figure 4.3 (a). The model starts form a perfect

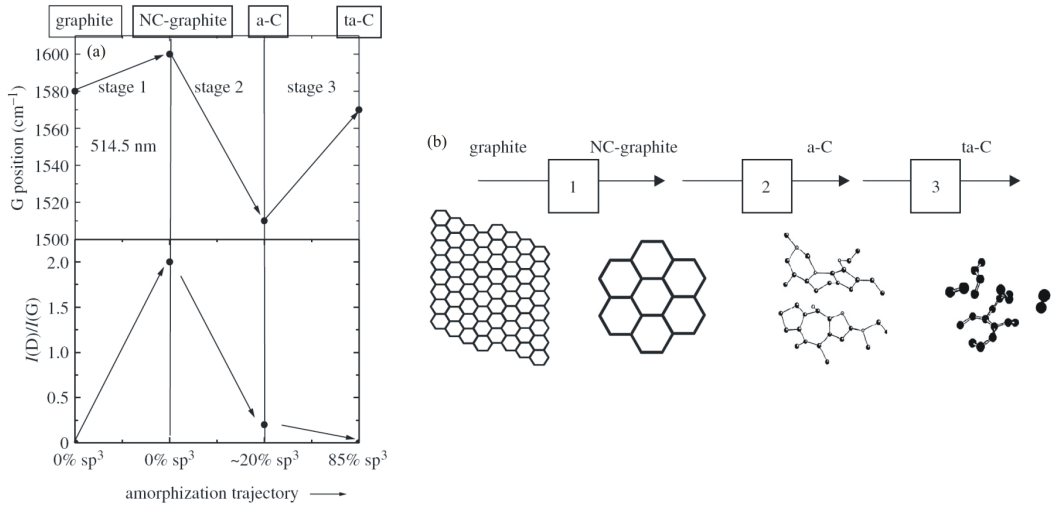

Figure 4.3: (a) Three-stage model of the variation of the Raman G position and the D to G intensity ratio, I(D)/I(G), with increasing disorder for 514.5 nm excitation [56]. (b) Variation of the sp^2 configuration in the three amorphization stages [135, 138].

infinite graphite sheet and considers how the introduction of a series of defects, namely bond-angle disorder, bond-length disorder and hybridization, which decrease the size of graphitic clusters affect the peak parameters. As one passes from ordered graphite to nanocrystalline graphite, amorphous carbon, and finally to sp^3 bonded ta-C, the sp^2 groups become smaller, then topologically disordered consisting of nonplanar rings, and finally change from ring to chain configurations. This path is called the *amorphization trajectory* [139] and consists of three stages from graphite to ta-C, as illustrated in figure 4.3 (a) and (b). The carbon bonding structure in these stages is characterized by the evolution of G peak position and I_D/I_G ratio. The Raman spectra depend on

(1) clustering of the sp^2 phase,

(2) bond-length and bond-angle disorder,

(3) presence of sp^2 rings or chains ,

(4) the sp^2/ sp^3 ratio.

Stage 1 corresponds to the reduction of the in-plane correlation length L_a within an ordered graphite layer. The G peak position moves from 1581 cm^{-1} to ~1600 cm^{-1} due to the appearance of a second peak, D', at ~1620 cm^{-1}, which corresponds to a maximum in the vibrational density of states (VDOS) of graphite [56]. The D peak appears and increases in intensity as the grain size L_a decreases following the Tuinstra-Koenig (TK) relation [133]:

$$L_a = 44 \times (I_D/I_G)^{-1} \tag{4.3}$$

for the excitation laser wavelength of 515.5 nm. The TK relation is valid until the cluster reaches a critical size of 20 $\mathring{A}$ [56].

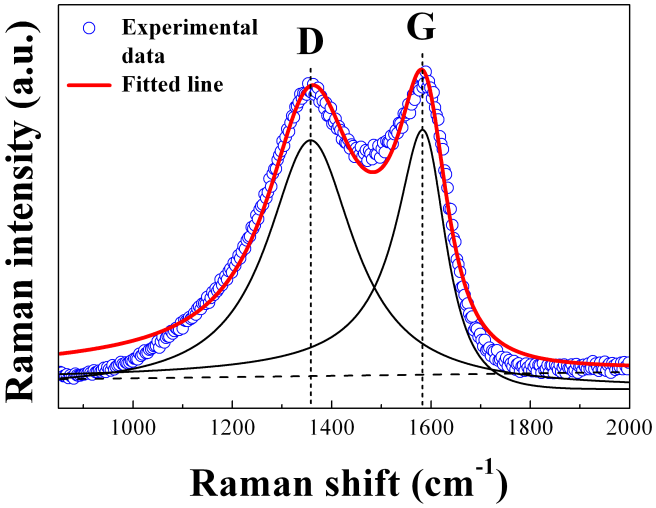

Figure 4.4: Fitted Raman spectra of a C:Co (∼30 at.%) composite film grown at 500°C. The fitting model uses a linear baseline, that is fixed at the measured points of lowest intensity, a symmetric Lorentzian D line and an asymmetric BWF line for the G peak.

Stage 2 is the introduction of topological disorder in the graphite layer. The bonding is still mainly sp^2, but bond-angle and bond-bending disorder and the presence of non sixfold rings result in weaker bonds that soften the vibrational modes. Thus, the G peak decreases to ∼1510 cm^{-1}. The TK relation is no longer valid and the I_D/I_G ratio decreases with decreasing cluster size L_a according to [56]:

$$L_a = [(I_D/I_G)/0.0055]^{\frac{1}{2}}. \tag{4.4}$$

and is proportional to the number of ordered aromatic rings.

Stage 3 is the conversion of sp^2 sites to sp^3 sites and the consequent change of sp^2 configuration from rings to chains. As olefinic C=C bonds are shorter than aromatic bonds, the G peak shifts upwards to ∼1570 cm^{-1}. I_D/I_G=0 due to the absence of aromatic rings.

In order to obtain a more quantitative understanding of the structural changes of the films in dependence of metal type, metal content and growth temperature the Raman spectra were fitted. There is no unique procedure in the literature used to fit the Raman spectra of carbon-based films in the wave number region 850-2000 cm^{-1}. Different fitting procedures for the fitting of the D and G peaks are possible comprising simple two Lorentzian [140, 141]or two Gaussians shapes [141–143], combination of Lorentzian and Gaussian shapes [144], and Lorentzian (D mode) and Breit-Wigner-Fano (BWF) (G mode) shapes [20, 56, 145]. In this work, the main criteria for the choice of the fitting procedure was the capability to fit all the spectra (C and C:TM) with the same type of functions. The combination of a linear background, a symmetric Lorentzian line for the D peak and an asymmetric BWF line for the G peak was found to be a good compromise between the fitting quality and the capability to fit all the Raman spectra.

An example is shown in figure 4.4. The intensity I as a function of wavenumber k for the BWF line shape is described by the following expression [56, 145]:

$$I(k) = \frac{I_0[1 + 2(k - k_0)/q\Gamma]^2}{1 + [2(k - k_0)/\Gamma]^2}, \tag{4.5}$$

with the intensity maximum I_{max}

$$I_{max} = I_0 \times [1 + 1/q^2] \tag{4.6}$$

positioned at [56]

$$k_{max} = k_0 + \Gamma/2q, \tag{4.7}$$

where I_0, k_0 and Γ are the peak intensity, peak position and full width at half maximum (FWHM), respectively, and q^{-1} is the BWF coupling coefficient. In the limit $q^{-1} \rightarrow 0$, the Lorentzian line shape is recovered. In the following, the intensity maximum defined by equation 4.6 will be used to denote the intensity of the G and D peaks, the position defined by equation 4.7 as the G and D peak positions, the width of the G peak as the parameter Γ in equation 4.5 and the width of the D peak as the FWHM. In the implantation and annealing studies of graphite and glassy carbon [140, 145] the limit of Γ_G/q$\rightarrow$0 has been identified as the point where in-plane graphene ordering is complete and three-dimensional ordering begins. Following this Γ_G/q (the coupling parameter) can be used to quantify the in-plane graphitic order.

4.4.3 Raman spectroscopy set up

Visible Raman spectra were recorded on a LAB Ram HR 800 spectrometer (Jobin Yvon, France) coupled to a BH2 microscope with a 50 fold magnifying objective (Olympus, Germany) using the second harmonic of a Nd:YAG solid state laser at 532 nm for excitation. The system was equipped with a 300 line/mm transmission grating and a Peltier cooled CCD detector. The spot size was $\sim$9 μm^2 and the laser power on the sample was 2 mW, except for some annealed C:Cu films with a laser power of 0.2 mW, giving $\sim$0.2 and $\sim$0.02 mW/μm^2. The spectral resolution was 3 cm^{-1}. The scattered light was collected in a 180° back scattering geometry. No sample degradation was detected under the used conditions. For each sample, two spectra were recorded at different positions of the sample, which were averaged to achieve better statistics. No significant differences among the single spectra from the same sample were observed.

5 Results and discussion

In the following, the investigation of the structural evolution in carbon:transition metal nanocomposite thin films during growth and the changes upon annealing is presented. In the first part of this chapter the effects of growth temperature, metal type and content on the phase structure and morphology of the dispersed phase, and on the bonding structure of embedding carbon medium are reported in sections 5.1.1, 5.1.2, 5.1.3, and 5.1.4. Section 5.1.5 summarizes and discusses the results from sections 5.1.1-5.1.4. In the second part the modification of phases and morphology of the nanocomposite as a result of annealing are presented and discussed in section 5.2.

5.1 Phase separation during film growth

5.1.1 Film composition and depth profiles

ERDA measurements at different locations of the samples show a uniform deposition in terms of the total amount of deposited metal and carbon atoms per unit area. Typical ERDA depth profile examples are presented in figure 5.1 (b)-(i) for the carbon and VC reference films, and C:TM (TM=V, Co, Cu) nanocomposite films with metal contents of ∼15 and ∼30 at.% grown at 300°C. It should be noted that natural ERDA depth units are 10^{15} atoms/cm^2. From the profiles two regions can be identified consisting of the deposited film followed by the SiO_2 substrate as schematically shown in figure 5.1 (a). The apparent smeared elemental distribution near the film surface and the non-sharp interface between the film and the SiO_2 substrate are due to the finite ERDA depth resolution. Moreover, the ERDA depth resolution decreases when the probing depth increases which results in an apparently broader interface region in comparison to the surface broadening and also a broader interface for thicker C:TM films in terms of the film areal density. It can be seen that both major film constituents - carbon and TM - are essentially homogeneously distributed over the film thickness. This is observed for all TM containing films deposited in the temperature range of RT-500°C, except for C:Co (∼30 at.%) and C:Co (∼40 at.%) films grown at 500°C (see figure 5.2 (b) and (c)) reflecting the thermodynamic tendency of the metal to segregate on the surface (see section 5.2). C:Ni (∼30 at.%) films grown at 500°C also show such a concentration gradient [147]. No metal surface segregation at the highest growth temperature of the study was observed for the other C:TM films, neither for the film with ∼15 at.% Co (figure 5.2 (a)) nor for the composites containing Cu and V, respectively. At the

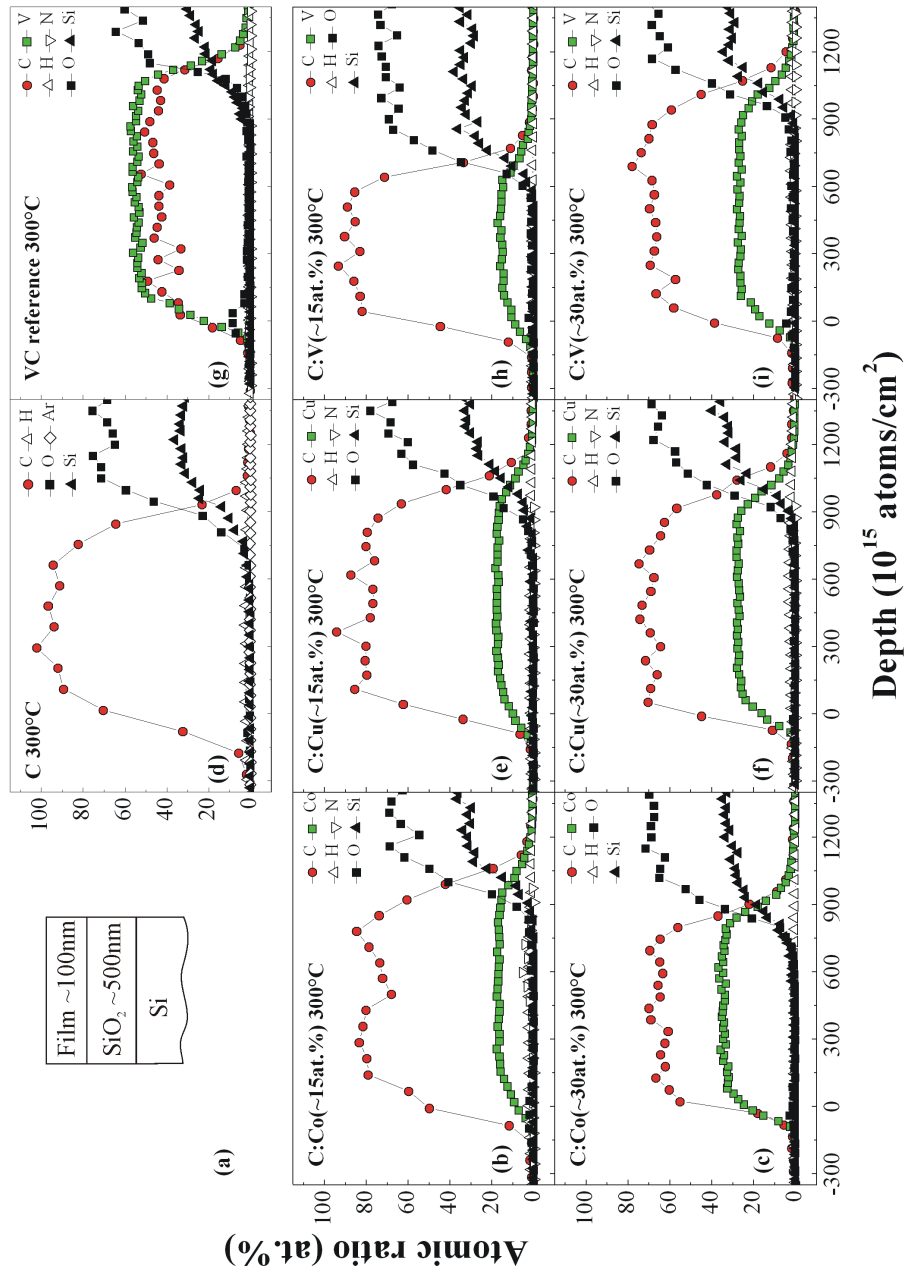

Figure 5.1: (a) Schematic drawing of a sample consisting of film and SiO_2/Si substrate. ERDA depth profiles of C:Co (∼15 at.%) (b), C:Co (∼30 at.%) (c), carbon reference (d), C:Cu (∼15 at.%) (e), C:Cu (∼30 at.%) (f), VC reference (g), C:V (∼15 at.%) (h) and C:V (∼30 at.%) (i) films grown at 300°C. The ERDA depth profiles of carbon reference, C:V (∼30 at.%), C:Co (∼15 at.%) and C:Cu (∼30 at.%) films are extracted from Ref. [146].

interface the C and TM atomic ratios decrease rapidly to zero, indicating that there is no significant inward diffusion of C or TM into the substrate. This is observed for films. The fluctuations in the ERDA depth profiles for light elements (C, O, N and Si) are due to the measurement statistics, as the scattering cross-section scales with Z^2, where Z is the atomic number of the target atom.

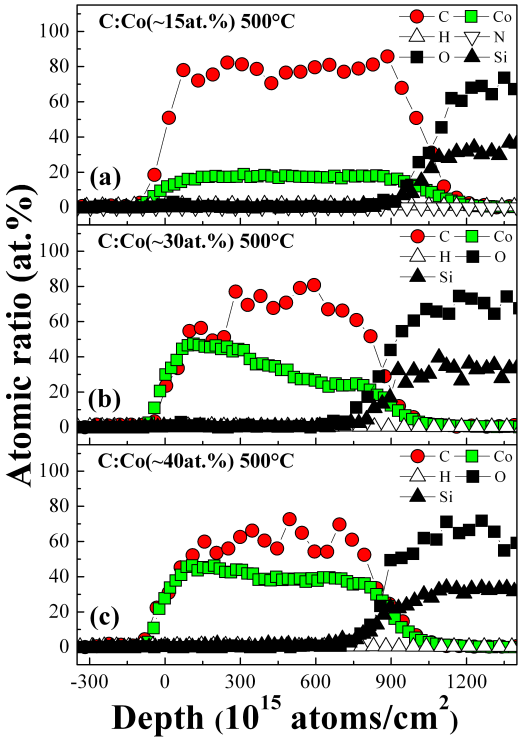

Figure 5.2: ERDA depth profiles of C:Co(∼15 at.%) (a), C:Co(∼30 at.%) (b), and C:Co(∼40 at.%) (c) films grown at 500°C.

The total film areal density t or the total amount of atoms deposited per unit area was calculated by integrating the atomic ratios of every film constituent over the film depth and then summing all the integrals of each constituent. The atomic ratio of a particular constituent was obtained by dividing the depth integral of the constituent by t. The results of the film areal densities t, atomic ratios of major film constituents and impurities of carbon reference and C:TM films grown at RT, 300 and 500°C are summarized in table 5.1. In addition, the values for the VC reference film grown at 300 and 500°C are shown. The ratio of TM areal density, t_{TM}, and the sum of carbon areal density, t_C, and TM areal density is also presented. The table shows that the amount of impurities such as oxygen or hydrogen is low in comparison to carbon and TMs, except for some samples deposited at RT. Their origin should be due to the presence of water and hydrocarbons in the residual gas, which adsorb on the growing film and are trapped by subsequently deposited atoms. Adsorbed water and hydrocarbons on the water-cooled substrate holder and their desorption during sputtering and implementation in the growing film might explain the maximum hydrogen and oxygen content in the films deposited at RT. For oxygen, a low intensity peak can be identified near the surface for the metal containing films which most probably is related to the oxidation of metal species after exposure of the film surface to the air. The oxygen surface peak is more pronounced for C:V composites and VC reference films than for the other C:TM

Table 5.1: Film areal densities t, compositions and $t_{TM}/(t_{TM} + t_C)$ ratios of the carbon reference, C:Co (∼15, ∼30 and ∼40 at.%), C:Cu (∼15 and ∼30 at.%), and C:V (∼15 and ∼30 at.%) films grown at RT, 300 and 500°C. The values of VC reference films grown at 300 and 500°C are additionally shown.

Film type	Film areal density t	Atomic ratio (at.%)						$t_{TM}/(t_{TM} + t_C)$
	(10^{18} cm^{-2})	C	O	H	N	Ar	TM	
C RT	0.95	93.7	0.6	5.0	0.4	0.3		
C 300°C	0.92	95.8	0.0	3.9	0.0	0.3		
C 500°C	0.89	95.4	0.0	4.6	0.0	0.0		
VC reference 300°C	1.18	43.9	2.1	0.7	0.5	0.0	52.8	0.55
VC reference 500°C	1.12	44.3	2.2	0.4	0.0	0.0	53.1	0.55
C:Co (∼15 at.%) RT	1.14	73.9	3.6	5.7	0.5	0.0	16.3	0.18
C:Co (∼15 at.%) 300°C	1.05	77.6	1.3	3.3	1.6	0.0	16.2	0.17
C:Co (∼15 at.%) 500°C	1.07	79.3	1.1	2.3	0.0	0.0	17.3	0.18
C:Co (∼30 at.%) RT	0.91	62.9	1.4	1.6	0.0	0.0	34.1	0.35
C:Co (∼30 at.%) 300°C	0.91	64.4	0.4	0.7	0.0	0.0	34.5	0.35
C:Co (∼30 at.%) 500°C	0.90	63.2	0.9	0.8	0.0	0.0	35.1	0.36
C:Co (∼40 at.%) RT	0.86	58.6	0.2	1.3	0.0	0.0	39.9	0.41
C:Co (∼40 at.%) 300°C	0.82	56.5	0.1	0.9	0.0	0.0	42.5	0.43
C:Co (∼40 at.%) 500°C	0.92	59.3	0.1	0.9	0.0	0.0	39.7	0.40
C:Cu (∼15 at.%) RT	1.13	74.9	0.7	5.5	1.8	0.0	17.1	0.19
C:Cu (∼15 at.%) 300°C	1.05	80.3	0.0	2.1	0.2	0.0	17.4	0.18
C:Cu (∼15 at.%) 500°C	1.06	74.5	4.6	2.7	0.6	0.0	17.6	0.19
C:Cu (∼30 at.%) RT	0.97	70.3	1.5	4.4	1.0	0.0	22.8	0.25
C:Cu (∼30 at.%) 300°C	1.03	69.3	0.0	3.4	0.4	0.0	26.9	0.28
C:Cu (∼30 at.%) 500°C	1.07	65.0	2.8	2.9	0.3	0.0	29.0	0.31
C:V (∼15 at.%) RT	0.79	82.8	0.8	2.1	0.0	0.0	14.3	0.15
C:V (∼15 at.%) 300°C	0.75	82.8	0.8	1.1	0.0	0.0	15.3	0.16
C:V (∼15 at.%) 500°C	0.65	81.1	0.4	1.4	0.0	0.0	17.1	0.17
C:V (∼30 at.%) RT	0.99	64.6	4.9	6.2	1.1	0.0	23.2	0.26
C:V (∼30 at.%) 300°C	1.06	69.2	1.5	2.6	0.5	0.0	26.2	0.27
C:V (∼30 at.%) 500°C	1.11	70.2	1.9	1.9	1.0	0.0	25.0	0.26

films. Some Ar incorporation has been detected only for the carbon reference films, originating from the sputter gas.

5.1.2 Dispersed phase: XRD investigations

C:Co films: Figure 5.3 (a)-(c) presents the X-ray patterns of C:Co composite films with Co contents of ∼15, ∼30, and ∼40 at.% grown at substrate temperatures in the range of RT-500°C. It should be noted that these patterns and all further presented XRD patterns are intermitted between 53° and 58° in order to blind out the (311) reflection from underlying Si at 56° that is observed in some of the patterns. No lines from the composite films are present in this angle range. For the C:Co (∼40 at.%) film grown at 500°C the coexistence of hcp and fcc Co can be clearly identified. At 41.7° a small diffraction peak is observed which can be assigned to the (100) reflection from the hcp Co phase. Further diffraction peaks are observed at 44.4°, 47.6°, and

∼51.5° corresponding to reflections from $(002)_{hcp}$ or $(111)_{fcc}$, $(101)_{hcp}$, and $(200)_{fcc}$, respectively. At higher diffraction angles further peaks are observed at ∼76°, ∼92° and ∼98° corresponding to reflections from metallic Co. The coexistence of both metallic Co phases is consistent with the observations in the literature [25]. In pure bulk Co the phase transition hcp Co-fcc Co occurs at 421.5°C [151]. The coexistence of hcp and fcc Co at 500°C in C:Co nanocomposite thin films shows that the temperature of phase transformation is shifted to a higher value in the Co-C system in comparison to pure bulk cobalt. When the deposition temperature decreases to 400°C, the sharp features in the XRD patterns disappear. The broad diffraction peak with the peak maximum close to 45° is a result of the superposition of three peaks from the hcp Co phase, namely the (100), (002) and (101) reflection. Further decrease in deposition temperature leads to the broadening of this peak. Besides, the peak maximum is shifted by ∼3° to lower diffraction angles when the temperature decreases from 400°C to RT which is attributed to a lattice parameter change. The broad peak below 400°C might be assigned to the metastable orthorhombic cobalt carbide (δ'-Co_2C) phase [33] which forms in the Co-C system at the conditions far away from thermodynamic equilibrium. Also cobalt carbide and hcp Co might co-exist in the so-called MS (metastable) II phase [22, 33]. Cobalt carbide becomes unstable at temperatures higher than about 300-420°C [6, 22, 25, 33]. The main downward peak shift is observed between 400 and 300°C most probably as a result of the formation of carbide phase. Besides, it might be expected that the strong increase in peak width below 400°C is in addition to the formation of smaller grains due to the superposition of several reflections from

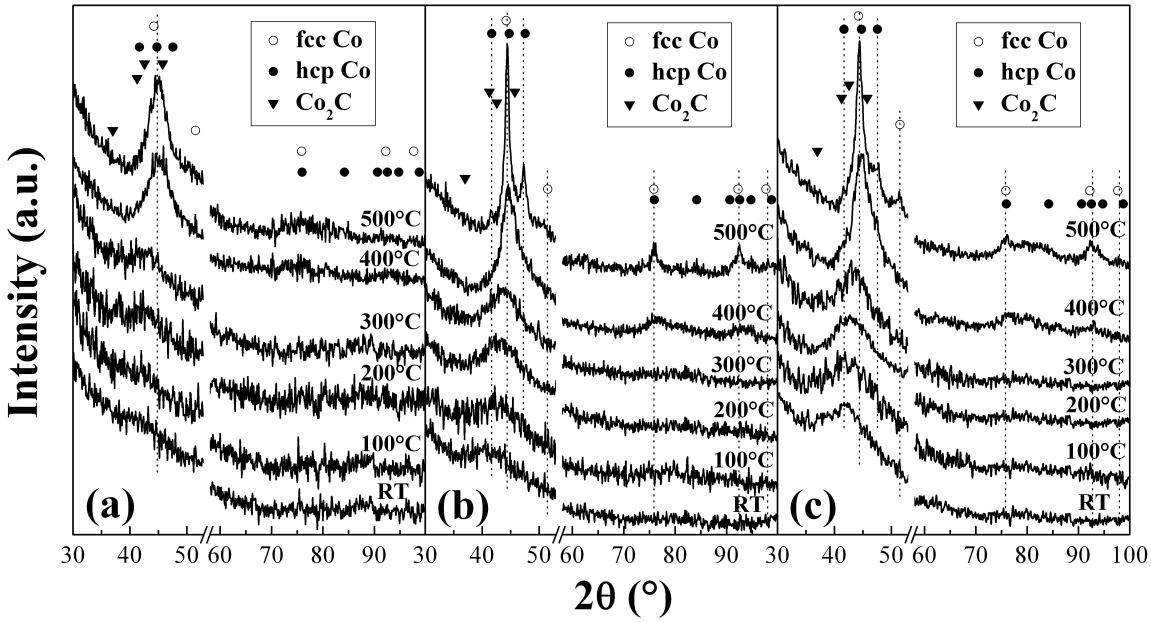

Figure 5.3: XRD patterns of C:Co (∼15 at.%) (a), C:Co (∼30 at.%) (b), and C:Co (∼40 at.%) (c) composite thin films grown at different substrate temperatures. The symbols represent the positions of the XRD peaks of Co_2C, hcp and fcc Co [148, 149]. The dotted lines indicate the peak positions of metallic Co. The XRD patterns of C:Co (∼30 at.%) films are extracted from Ref. [150].

Table 5.2: Saturation magnetization measured at 5k and estimated fraction of metallic Co in C:Co (∼40 at.%) composite thin films grown at different substrate temperatures. The values for the saturation magnetization for the samples grown at 200-500°C are extracted from Ref. [19].

T (°C)	Magnetization (μ_B/Co)	Metallic Co (%)
RT	0.18	11
100	0.29	17
200	0.35	21
300	0.55	32
400	1.15	68
500	1.29	76

the coexisting cobalt carbide and hcp Co phases. In addition, the overlapping of the peaks and the temperature dependent ratio of carbidic and metallic phase might result in an apparent shift of the overall features toward lower diffraction angles with decreasing temperature. The above observations lead to the assumption that cobalt carbide is the majority phase below 400°C and hcp Co exists as the minor phase, if existing at all. The presence of cobalt carbide at low temperatures has also been reported in Refs. [6, 25]. Besides, X-ray absorption spectroscopic investigations on C:Co films clearly identified a transition from carbidic to metallic Co when the growth temperature increases from RT to 500°C [146] which confirms the present tendencies. Investigations of the magnetic properties of C:Co composite films by superconducting quantum interference device (SQUID) magnetometry showed that cobalt carbide is the major phase up to 300°C, while above that temperature metallic Co becomes the dominating phase [19]. A comparison of the saturation magnetization in C:Co composite films with the value of fcc or hcp Co of around 1.7 μ_B/Co allows estimating the fraction of metallic Co in the samples as listed in table 5.2. Therewith, SQUID measurements revealed the presence of metallic Co at temperatures as low as RT, although their quantity is strongly reduced. This indicates the presence of the MS II phase [33] in a temperature dependent quantity below 400°C, and confirms the above assumptions.

For lower Co contents similar observations can be made as for the C:Co (∼40 at.%) films. From figure 5.3 it becomes obvious that the width of diffraction peaks increases as the metal content in the films decreases which is a hint for the formation of smaller grains. In the C:Co (∼15 at.%) film grown at 500°C both metallic Co phases can not be distinguished due to the presence of a broad diffraction peak emerging from the small grain size and the superposition of several reflections from the hcp and fcc Co phase. In addition, figure 5.3 clearly shows that with decreasing deposition temperature the width of diffraction peaks increases which indicates about a decrease in grain size. However, one should keep in mind that for the C:Co (∼ 30at.%) and C:Co (∼ 40at.%) films grown below 500°C, and for the C:Co (∼15 at.%) films in the whole temperature range the superposition of reflections from several Co phases results in a further peak

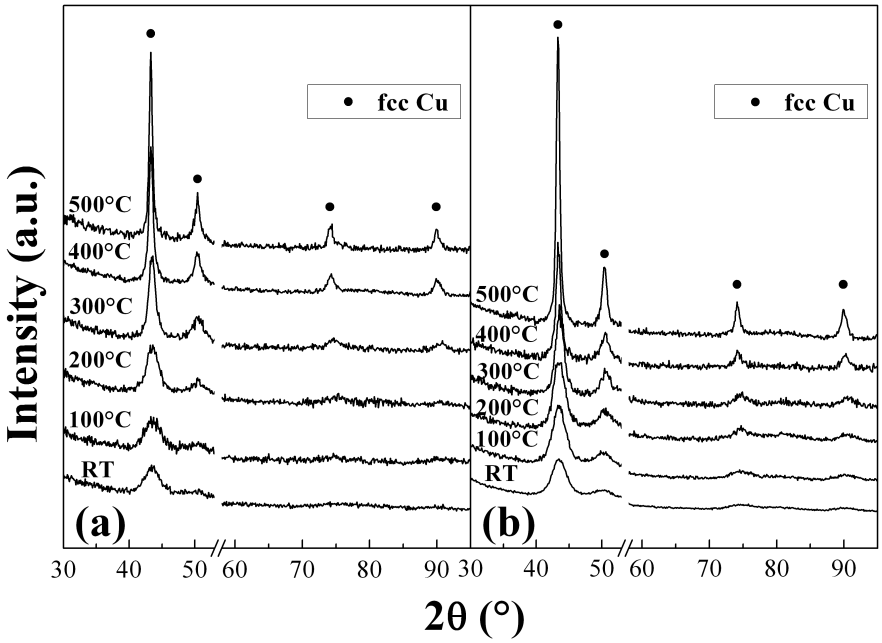

Figure 5.4: XRD patterns of C:Cu (∼15 at.%) (a) and C:Cu (∼30 at.%) (b) composite thin films grown at different substrate temperatures. The symbols represent the XRD peaks of fcc Cu [152]. The XRD patterns of C:Cu (∼30 at.%) films are extracted from Ref. [146, 150].

broadening, thus hindering any analysis of the grain size.For the C:Co (∼ 30at.%) and C:Co (∼ 40at.%) films grown at 500°C the grain size estimated from the (111) peak width of fcc Co in the XRD patterns by the Scherrer formula is in the range of 5-7 nm. It should be noted that the relatively high background intensity of the XRD patterns and the presence of several diffraction peaks from metallic Co in a small angle range complicates the deconvolution of the patterns.

C:Cu films: Figure 5.4 presents the X-ray patterns of C:Cu composites with metal contents of ∼15 and ∼30 at.% grown at substrate temperatures in the range of RT-500°C. The C:Cu films show features characteristic for the fcc copper phase in the whole temperature range for both Cu contents. Copper exhibits a very low miscibility with carbon which prevents the formation of carbide phases. Consequently, even at the lowest growth temperature used in the present study a complete demixing of copper and carbon occurs and Cu crystallites are formed. This is consistent with the observations on C:Cu composites found in the literature at similar Cu contents and growth temperatures [24]. The patterns clearly show that an increase in temperature results in a narrowing of the diffraction peaks which indicates grain coarsening. The size of Cu crystallites estimated from the Scherrer formula which is summarized in table 5.3 quantifies the observed tendency. Besides, the table reveals that the crystallite size is independent of the Cu content. The grain size of C:Cu (∼30 at.%) films grown at 500°C is larger than those of corresponding C:Co films.

Table 5.3: Size of Cu crystallites estimated from the (111) and (200) peak widths in the XRD patterns by the Scherrer formula for C:Cu (∼15 at.%) and C:Cu (∼30 at.%) composite thin films grown at different substrate temperatures.

T (°C)	Crystallite size (nm)	
	C:Cu (∼15 at.%) films	C:Cu (∼30 at.%) films
RT	3±1	3±1
100	3±1	4±1
200	4±1	4±1
300	6±2	6±2
400	10±2	10±2
500	13±3	14±3

C:V films: The XRD patterns of C:V nanocomposite films and VC reference films grown at different substrate temperatures are shown in figure 5.5. The VC reference films show sharp diffraction peaks typical for the rock salt structure with the peak positions corresponding to those of fcc VC from the database International Center for Diffraction Data [153]. The presence of the fcc VC phase in sputter deposited V-C coatings has also been reported in the literature [98, 99]. The diffraction patterns show no remarkable changes with growth temperature indicating a constant size of VC crystallites (see table 5.4). C:V (∼30 at.%) nanocomposites show broad peaks at the positions of those of VC reference films which is a hint for the formation of smaller crystallites. The peaks at 37.4°, 43.4° and 63.1° can be assigned to the (111), (200) and (220) plane of fcc VC, while the broad feature between 70° and 80° arises from the superposition of the (311) and (222) reflections at 75.7° and 79.7° of this phase [153]. No significant changes in the width and intensity of the diffraction peaks are observed in the whole temperature range, except for the C:V (∼30 at.%) film deposited at RT showing very broad peaks, which indicates about the low effect of the growth temperature on the grain size. The estimated size of VC crystallites by the Scherrer formula shown in table 5.4 confirms this observation. It should be noted that for the C:V composites the low signal to noise ratio complicates the determination of the FWHM making it impossible for the C:V film grown at RT. Thus, the calculated grain size represents only a rough estimation. When the V content decreases to 15 at.% the diffraction peaks further broaden (see figure 5.5 (a)). In contrast to C:V (∼30 at.%) composites and VC reference films, the C:V (∼15 at.%) films show a decreasing width of the diffraction peaks when the growth temperature increases indicating about the formation of larger grains at higher temperatures. Owing to the very broad features in the XRD patterns it is not possible to estimate the size of VC crystallites below 400°C. At RT and 100°C the patterns have a featureless appearance indicating that the actual crystallite size is below the detection limit of XRD. It has been reported in the literature that at such low V contents no carbide particles are formed during the deposition at RT [100]. Thus, the evolution and sharpening of diffraction peaks at higher growth temperatures could be due to the formation and growth of small carbide crystallites.

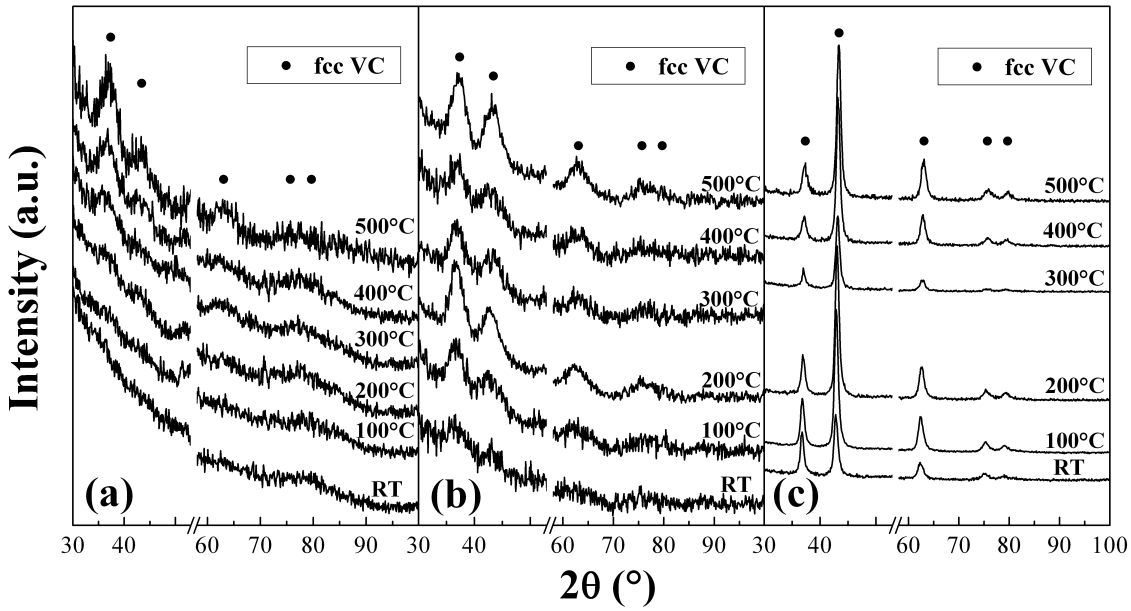

Figure 5.5: XRD patterns of C:V (∼15 at.%) (a) and C:V (∼30 at.%) (b) composite thin films, and VC reference films (c) grown at different substrate temperatures. The symbols represent the positions of the XRD peaks of fcc VC [153]. The XRD patterns of C:V (∼30 at.%) films are extracted from Ref. [146, 150].

In summary, C:V and C:Cu nanocomposite films show the presence of vanadium carbide and metallic copper, respectively, in the whole temperature range of the study. In contrast, in C:Co films cobalt carbide is the majority phase up to 300°C, while metallic Co becomes the dominant phase at higher growth temperatures. At 500°C hcp and fcc Co coexist. All C:TM nanocomposites show an increase in grain size with TM content and growth temperature with the exception of C:Cu films for the former. Only for C:V (∼30 at.%) films the influence of the growth temperature is insignificant. For any TM content at the highest growth temperature the grain size decreases in the order Cu > Co > V, i.e. reverse to their carbon chemical affinity.

Table 5.4: Size of VC crystallites estimated from the (111) peak width in the XRD patterns by the Scherrer formula for C:V (∼15 at.%) and C:V (∼30 at.%) composite thin films, and VC reference films grown at different substrate temperatures.

T (°C)	Crystallite size (nm)		
	C:V (∼15 at.%) films	C:V (∼30 at.%) films	VC reference films
RT	-	-	12±2
100	-	2±1	12±2
200	-	2±1	12±2
300	-	2±1	11±2
400	1±1	2±1	10±2
500	1±1	2±1	10±2

5.1.3 Structure and morphology of the films: TEM investigations

This chapter presents the results on the film morphology and phase structure of C:Co, C:Cu and C:V composites during growth studied by the means of plan-view and cross-sectional transmission electron microscopy in combination with selected area electron diffraction. The first part of this chapter considers the metal content dependence of C:Co films on the morphology of the dispersed phase and the matrix while in the second and third part the study of the influence of the metal type is presented.

C:Co films: The cs-TEM images of C:Co composite films grown at RT, 300 and 500°C with cobalt contents between 15 and 40 at.% are shown in figure 5.6. The images show that all the films belong to zone III in the structure zone model suggested by Barna and Adamik [81] for composite films grown by physical vapor deposition. The films are composed of dark grains surrounded by brighter areas. Judging from the atomic number, Z, of Co and C (Z=27 and 6, respectively), the dark grains are metal-rich particles, while brighter areas represent the carbon matrix. This is valid to all further BF-TEM images of the C:TM nanocomposite films, because V and Cu (Z=23 and 29, respectively) also exhibit significantly higher atomic numbers than C. At RT Co nanoparticles exhibit a globular shape. The TEM images reveal an increase in grain size with Co content. In C:Co (∼15 at.%) films the nanoparticles have a diameter of ∼2 nm, while for a Co content of ∼40 at.% grains up to 4 nm in diameter are formed. The shape of Co nanoparticles changes with increasing growth temperature to an elongated structure in the direction of the thin film growth. The cs-TEM images of figure 5.6 (b), (e) and (h), which show the film morphology at a growth temperature of 300°C, clearly demonstrate that the growth proceeds in a more aligned manner with a higher aspect ratio for higher Co concentrations in the films. In addition to their length, the width of elongated nanoparticles also increases concomitantly with temperature. In C:Co (∼15 at.%) films, slightly elongated nanoparticles are present with a length of 2-5 nm and a width of ∼2 nm (average aspect ratio 1.5), while C:Co (∼40 at.%) films show columnar-like nanoparticles with a length of 6-10 nm and a width of 4-6 nm (average aspect ratio ∼2). The plan-view (pv) TEM images in figure 5.7 additionally point out the increase in nanoparticle diameter with Co content. When the growth temperature further increases up to 500°C, the elongated structure of Co nanoparticles becomes more pronounced. However, as can be seen from figure 5.6 the growth of nanocolumns is always interrupted, and repeated nucleation occurs even for the highest Co concentration of ∼40 at.%.

Plan-view high-resolution TEM imaging (see figure 5.7 (b)) shows that the nanoparticles are encapsulated by graphite-like carbon (GLC). The latter appear as curved fringes which follow the boundaries of the nanoparticles. Depending on the interparticle distance, three- to five-layer thick graphitic shells with the spacing of 0.34 nm fill the space between Co-rich nanoparticles. However, no layered structures are visible in the pv-TEM image of figure 5.7 (a), when the contrast between the particles and the carbon matrix is low. This is associated with the lower thickness of this sample in comparison to the sample of figure 5.7 (b). The thicker sample generates a darker image due to overlapping of different grains. It should be noted that during sample

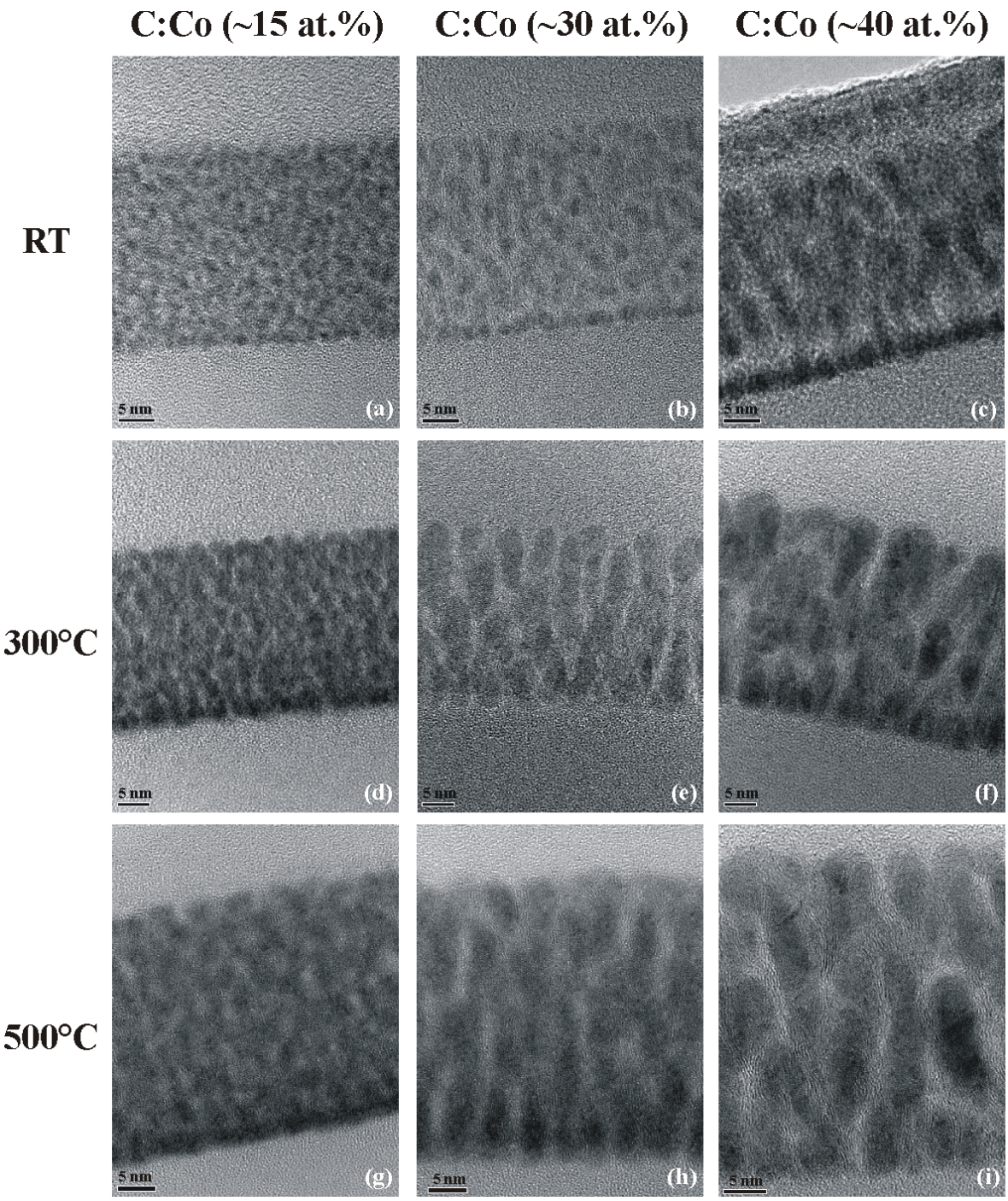

Figure 5.6: Cross-sectional high-resolution bright-field TEM images of the C:Co (∼15 at.%) ((a)-(c)), C:Co (∼30 at.%) ((d)-(f)) [150], and C:Co (∼40 at.%) ((g)-(i)) composite thin films grown at RT, 300 and 500°C.

preparation (ion milling) for TEM imaging the carbon matrix is modified by the ion beam and in the outer regions of the sample carbon becomes amorphous while the inner remains unchanged. This can lead to a complete amorphization of carbon if the sample is too thin and might explain the absence of layered ordering of the matrix observed in the image of figure 5.7 (a). The cs-TEM images of figure 5.6 show the presence of

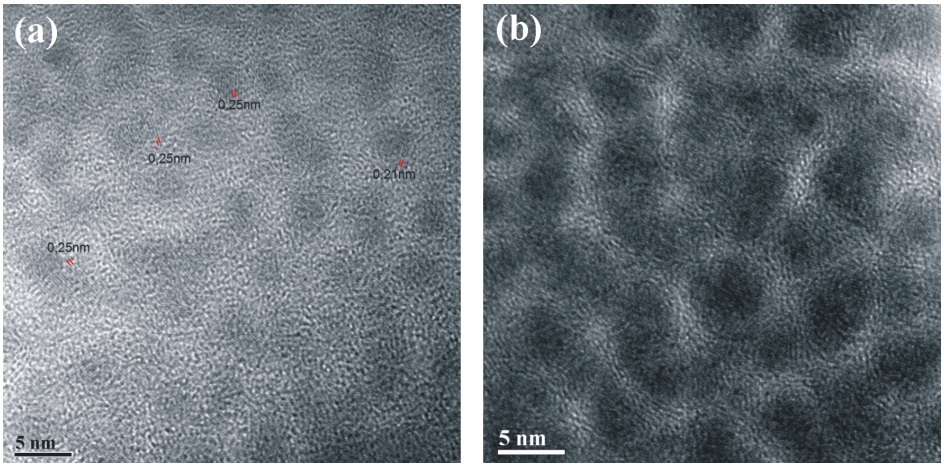

Figure 5.7: Plan-view high-resolution bright-field TEM images of the C:Co (∼15 at.%) (a) and C:Co (∼40 at.%) (b) composite thin films grown at 300°C [19]. Image (a) shows lattice fringes in the nanoparticles corresponding to the cobalt carbide or metallic Co phase.

graphitic planes following the surface of the nanoparticles for the samples grown at 300 and 500°C. No such layered ordering of the matrix is observed at RT indicating the transition from amorphous to graphite-like carbon between RT and 300°C. Delaunay et al. [22] have reported similar morphologies in their C:Co films prepared by IBS. Besides, similar carbon structures produced by magnetron sputtering have also been reported in the literature [25, 26].

The SAED patterns of the C:Co (∼30 at.%) film grown at RT and 300°C show broad rings (see figure 5.8 (a) and (b)). The innermost ring corresponds roughly to the d-spacing of (002) graphite, while the other two rings, the outermost being hardly visible, may consist of several unresolved rings. In this case, the nanoparticle phase can not be determined unambiguosly which makes it impossible to clarify if carbidic and metallic phases coexist at T≤300°C. The broad diffraction rings have been associated in the literature with an amorphous-like phase [6, 11, 22, 25, 26, 33]. In addition, at RT no lattice fringes in the cobalt-rich grains could be identified, suggesting that the grains are amorphous. This is consistent with the lack of driving force for the crystallization in C:Co alloys grown at this low temperatures [33] in contrast to C:TM systems with a strong tendency to form carbides as for C:V or C:Ti nanocomposites [32, 154, 155]. In contrast, the pv high-resolution TEM image of the C:Co (∼15 at.%) composite thin film grown at 300°C in figure 5.7 (a) shows lattice spacings of 0.21 and 0.25 nm in the Co-rich grains. The first value can be assigned to the (111) plane of cobalt carbide or to $(100)_{hcp}$ Co, and the second one to the (110) plane of cobalt carbide. In figure 5.7 (b) no lattice images of the grains can be observed due to overlapping of different grains because of the larger sample thickness, as already mentioned above. The diffuse diffraction rings for the sample grown at 300°C might therefore be assigned to the superposition of several rings from the hcp or cobalt carbide phase, or lattice distortions due to interstitial carbon [11, 22, 33]. On the other hand, the SAED pattern of the C:Co (∼30 at.%) film grown at 500°C shows numerous sharp rings which can be attributed to the hcp and fcc cobalt phase demonstrating the coexistence of both metallic phases, and a broad ring at the graphite (002) position. The presence of sharp

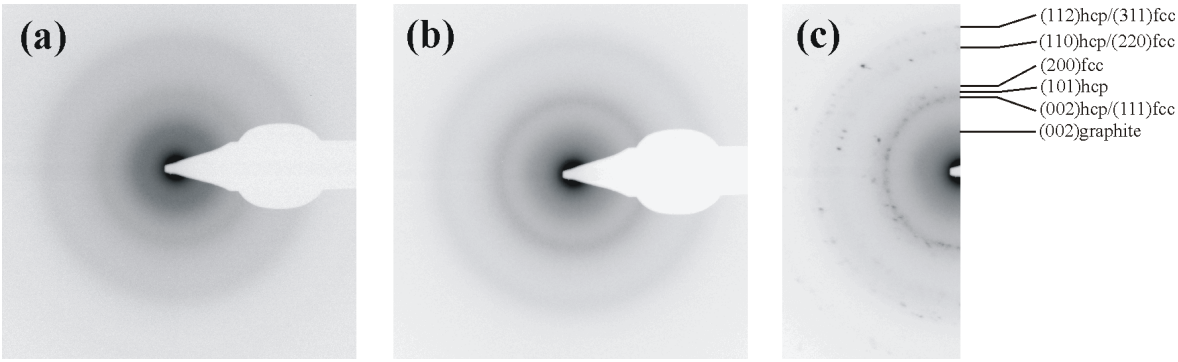

Figure 5.8: SAED patterns of the C:Co (∼30 at.%) composite thin films grown at RT (a), 300 (b) and 500°C (c). In the diffraction pattern, the rings are indexed with $(hkl)_{hcp}$ and $(hkl)_{fcc}$ for the hexagonal cobalt and the face-centered cubic cobalt phase, respectively.

rings confirms the grain coarsening at higher temperatures already observed in the cs-TEM images of figure 5.6.

In summary, TEM observations of C:Co films reveal a growth transition from globular to elongated nanoparticles between RT and 300°C. In addition, the length and diameter of elongated nanoparticles increase concomitantly with Co content and growth temperature. Besides, at T≥300°C curved graphitic planes encapsulating the nanoparticles are observed while at RT the carbon phase has a featureless appearance which indicates that the transition from amorphous to GLC occurs between these two temperatures.

C:Cu films: Figure 5.9 (a)-(c) shows the cs high-resolution TEM images of C:Cu (∼30 at.%) composite thin films prepared at RT, 300 and 500°C, (d)-(f) are the corresponding SAED patterns. The nanoparticles are crystalline grains. According to electron diffraction analysis the crystals are of fcc Cu [152]. The SAED patterns are composed of an innermost broad ring at the d-spacing of (002) graphite and numerous sharp rings due to the fcc Cu phase. It should be noted that at 300 and 500°C two additional diffraction rings are present corresponding to the (110) and the (210) plane of fcc Cu. These reflections are normally forbidden in fcc copper (all Miller indices are either even or uneven). Their origin might be related to some dissolved carbon atoms which remain trapped in the Cu phase. The interstitial carbon atoms might cause lattice distortion and the break down of symmetry rules for the perfect crystal giving rise to forbidden reflections. At RT the nanoparticles exhibit a fine-grained structure similar to C:Co films, except that the grain size of ∼4 nm is slightly larger than that of the C:Co film with a similar metal content (grain size of ∼3 nm). The shape of Cu nanoparticles also changes with increasing temperature to a more elongated structure in the direction of the thin film growth and becomes more pronounced at the highest growth temperature of this study (figure 5.9 (c)). At 300°C the elongated shape of nanoparticles is less pronounced in the C:Cu films than in the C:Co films with a similar metal content. This is related to the larger width of elongated particles in the case of Cu while in both types of films the grains exhibit a similar height resulting in a lower aspect ratio of the Cu particles. By comparing the cs-TEM images of both

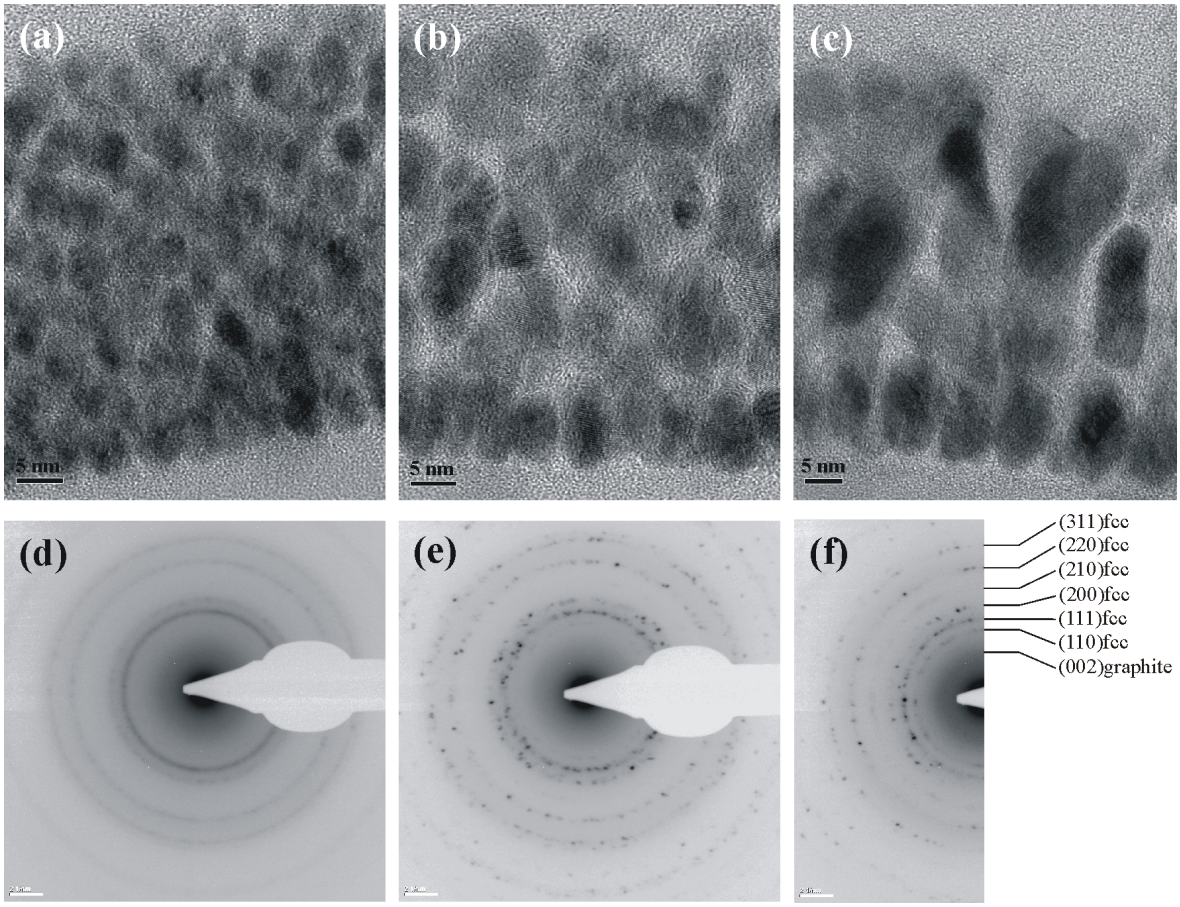

Figure 5.9: Cross-sectional high-resolution bright-field TEM images of the C:Cu (∼30 at.%) composite thin films grown at RT (a), 300 (b) and 500°C (c) [150] and corresponding SAED patterns ((d)-(f)). In the diffraction pattern, the rings are indexed with $(hkl)_{fcc}$ for the face-centered cubic copper phase.

types of films grown at 500°C, it becomes evident that Cu grains exhibit a broader size distribution. For C:Cu films, the elongated columns have a width of 6-12 nm and a length of 10-20 nm, while elongated Co columns show a width of 4-6 nm and a length of 7-13 nm. However, no columns with their height equal to the film thickness are observed in the given temperature range similar to the C:Co films.

Cross-sectional high-resolution TEM imaging shows that the carbon phase has a featureless appearance at RT (see figure 5.9 (a)). The pv high-resolution TEM image in figure 5.10 of the C:Cu film prepared at 300°C shows Cu nanoparticles of sizes in the range of 4-7 nm which are encapsulated by graphite-like carbon layers indicating that the transformation from amorphous carbon to GLC occurs between RT and 300°C. This has also been reported elsewhere in the literature [24]. The planes appear as curved fringes being parallel to the surface of copper nanoparticles. In dependence of the interparticle distance at some locations only a few graphitic planes are visible, while at other locations stacked graphitic planes with a thickness of ∼3 nm are present. The latter indicates that the majority of the carbon matrix has a layered ordering with its layers filling the space between Cu nanoparticles. For a larger distance from the

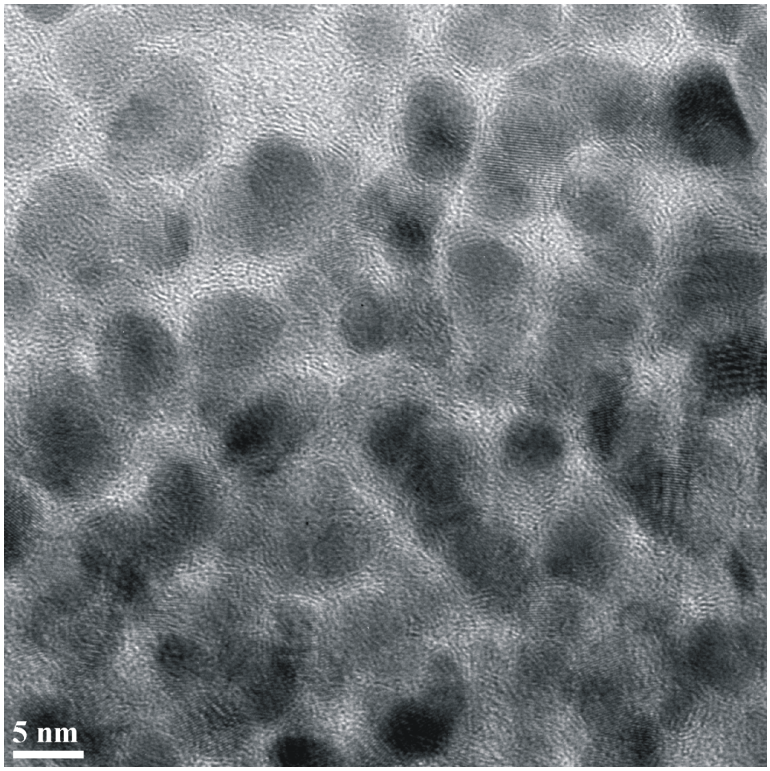

Figure 5.10: Plan-view high-resolution bright-field TEM image of the C:Cu (∼30 at.%) composite thin films grown at 300°C.

nanoparticles the carbon phase has a featureless appearance indicating the transition to an amorphous structure (see the relatively large carbon area in the upper part of figure 5.10). The layered structure can be additionally seen in the cs-TEM images of the samples grown at T≥300°C (figure 5.9 (b) and (c)).

Finally, TEM observations combined with selected area electron diffraction confirm the presence of fcc Cu in the whole temperature range as observed by XRD. Concerning the film morphology, C:Cu films showed a similar growth temperature dependence as C:Co films, except that Cu grains are larger and exhibit a broader size distribution at 500°C.

C:V films: Figure 5.11 shows the cs high-resolution TEM images of the C:V (∼30 at.%) thin films deposited at RT, 300 and 500°C. At RT the crystalline particles exhibit a fine-grained structure with a diameter of 1-2 nm. The globular shape of nanoparticles is preserved until the highest deposition temperature of this study of 500°C and their size only slightly increases with temperature up to ∼3 nm. The fine-grained structure of vanadium carbide is consistent with the HRTEM observations on carbon-rich V-C films deposited by magnetron sputtering [99]. At 300 and 500°C, high-resolution cs-TEM imaging reveals the presence of curved graphitic (graphene) shells encapsulating the nanoparticles (see inset of figure 5.11 (b) and (c)) even though the small grain size complicates their observation. At RT the tissue phase appears amorphous indicating the transition from an amorphous structure to a layer-like ordering of the carbon matrix between RT and 300°C similar to the observed tendency in C:Co and C:Cu composites.

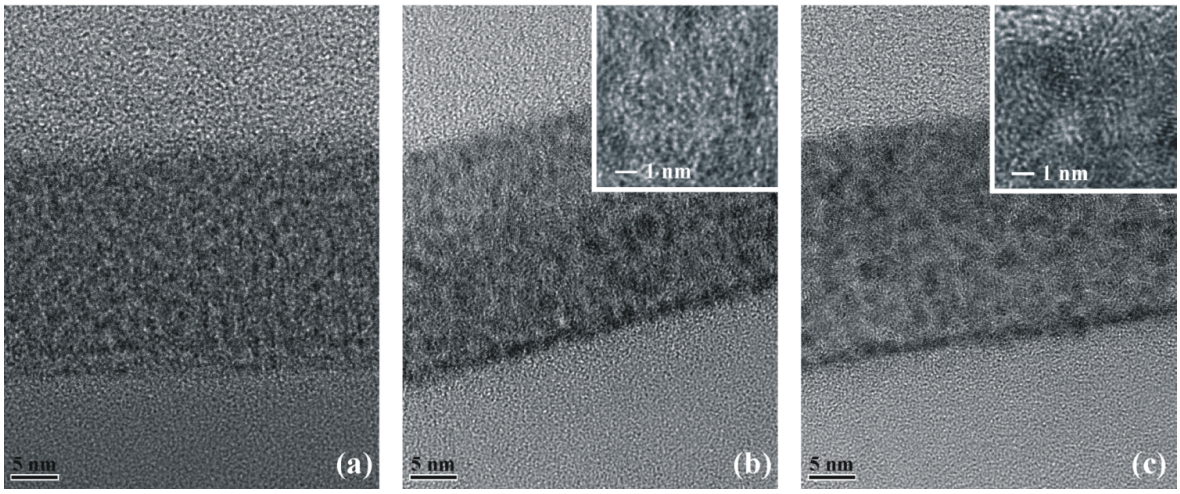

Figure 5.11: Cross-sectional high-resolution bright-field TEM images of the C:V (∼30 at.%) composite thin films grown at RT (a), 300 (b) and 500°C (c) [150].

The pv high-resolution TEM image of a C:V (∼30 at.%) film deposited at 300°C is shown in figure 5.12 (a). The grains have a size of ∼2 nm. Besides, lattice fringes in the VC grains are clearly observed which indicates about their crystalline structure. Fast Fourier transformation (FFT) of the image tells, that the crystallites are vanadium carbide, which confirms the XRD observation. The observed lattice spacings are close to the (111), (200) and (220) reflections of the fcc VC phase [153]. Besides, the innermost halo is roughly at the d-spacing of (002) graphite. However, the graphitic layers of carbon are only visible in a few places of the image. This is associated with the small grain size which imposes a strong curvature of the graphene layers. Standing graphitic planes are well visible in the TEM, while in the case of globular particles a decreasing grain size results in a stronger curvature of the layers which leads to a decrease in the intensity of the projected graphitic planes in the TEM image. This also explains why the curved planes are hardly visible in the cs-TEM images.

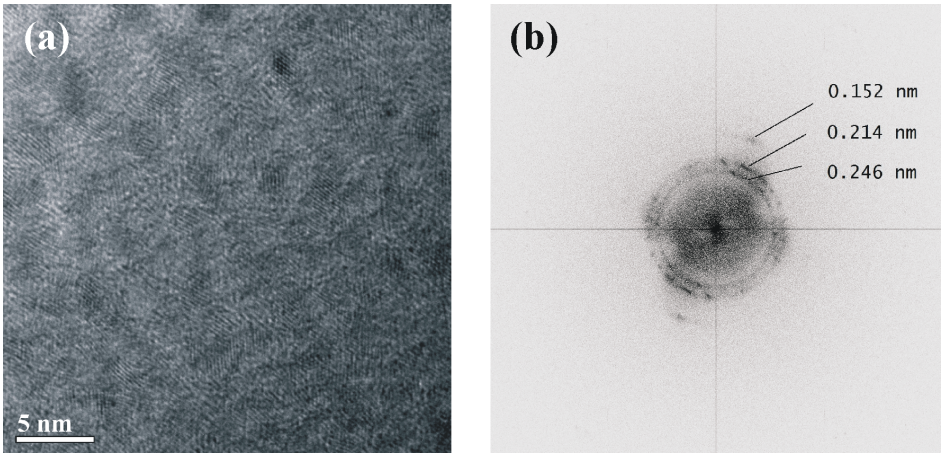

Figure 5.12: Plan-view high-resolution bright-field TEM image (a) and corresponding FFT (b) of the C:V (∼30 at.%) composite thin films grown at 300°C.

In summary, the nanoparticles in C:V films exhibit a fine-grained structure in the whole temperature range and show a very low growth temperature dependence which is in contrast to the behavior in C:Co and C:Cu films and might be related to the formation of stable VC grains. A transition from an amorphous carbon matrix to curved graphitic planes encapsulating the nanoparticles is observed between RT and 300°C.

The estimated grain size from the width of diffraction peaks in the XRD patterns employing the Scherrer equation and the size obtained by TEM imaging of C:TM films containing ∼30 at.% metal show in general a good agreement. It should be noted that the calculations of the grain size by the Scherrer formula, which represents only a rough estimation of the grain size, were based on a cubic shape of the crystallites, whereas Cu and Co grains are elongated at T≥300°C. Furthermore, for GID the direction of the scattering vector in which the crystallite size is measured varies with the detector position, i.e. the deviation from the surface normal increases with the 2Θ value. This explains why in the case of elongated crystallites the size obtained by the Scherrer formula is smaller than the observed particle height by cs TEM. The estimated size of Co crystallites at 500°C is in the order of 5-7 nm, which is slightly below the height of Co grains (7-13 nm). The corresponding Cu crystallites exhibit an estimated size of 11-17 nm, while their height is 10-20 nm. As only low diffraction peaks (2Θ<50°) were used for the determination of the crystallite size, the deviation of the direction of the scattering vector from the surface normal is below 24,5° resulting in a small difference of the grain size obtained by XRD and cs TEM. However, the Co crystallites show a worse agreement between both analysis techniques than Cu crystallites which might be related for the former with the relatively high background intensity of the XRD pattern and the presence of several diffraction peaks from metallic Co in a small angle range complicating the deconvolution of the pattern.

Concluding, TEM investigations of the C:TM films show their composite structure in which a nanometer sized metallic or carbidic dispersed phase is embedded in a carbon matrix. C:Co and C:Cu films show a growth transition from globular to elongated nanoparticles between RT and 300°C but no nanocolumns are observed up to the highest temperature of this study of 500°C. In C:V films the globular shape is preserved up to 500°C and the grain size increases only slightly with temperature. For a metal content of ∼30 at.% the grain size decreases in the order: Cu > Co > V, which is reverse to their carbon chemical affinity. At T≥300°C all C:TM films are composed of globular or elongated metal-rich nanoparticles which are three-dimensionally separated by curved graphitic planes, while at RT carbon phase appears amorphous. The layered structure of the carbon matrix visible by HRTEM suggests sp^2-type ordering of the carbon matrix, since the presence of sp^3 bonds, even at a small overall content, creates crosslinking between the layers and breaks down the two-dimensional layered ordering. The layers can have graphene-like structure, which means the layers are formed mainly from sixfold aromatic rings or the layers consist of fullerene-like sp^2-bonded clusters having a significant amount of non-sixfold rings. The embedding medium does not exhibit a regular layered structure but consists of fragments of different dimension and curvature, which makes a quantification by employing only microscopic means difficult.

Raman spectroscopy, which will be the object of analysis in the next section, allows highlighting and in addition a quantification of the structural features of the embedding phase even if it appears amorphous or featureless in microscopy.

5.1.4 Carbon matrix: Raman spectroscopic investigations

General observation from Raman spectra

Figure 5.13 (a)-(d) shows the normalized Raman spectra of the carbon reference and of C:Co composite films with Co contents of ∼15, ∼30, and ∼40 at.% in the wavenumber range 700-1900 cm^{-1} measured with 532 nm excitation light. All further Raman spectra in this section are presented in the same wavenumber region. For comparative purpose the normalized Raman spectra of tetrahedral amorphous carbon (ta-C), nanocrystalline graphite and graphite are shown in figure 5.14. Tetrahedral amorphous carbon has a high content of sp^3 hybrids of ∼85% and localized sp^2 modes [56]. The Raman spectra of ta-C shows a broad asymmetric peak around 1540 cm^{-1}. A peak at ∼960 cm^{-1} from underlying Si substrate is also observed. The spectra of nanocrystalline graphite exhibit two sharp modes, the D and G peak, at 1350 and 1582.5 cm^{-1}, respectively. Graphite shows the single sharp G line at 1581 cm^{-1}.

In order to point out the effect of Co on carbon, the features present in the Raman spectra of carbon reference samples are discussed first (figure 5.13 (a)). At RT and 100°C the contribution of the D peak to the Raman spectra is very low and can be hardly resolved in the spectra, while it increases concomitantly with temperature. The RT Raman spectra are similar to those of amorphous carbon films grown at RT by IBS

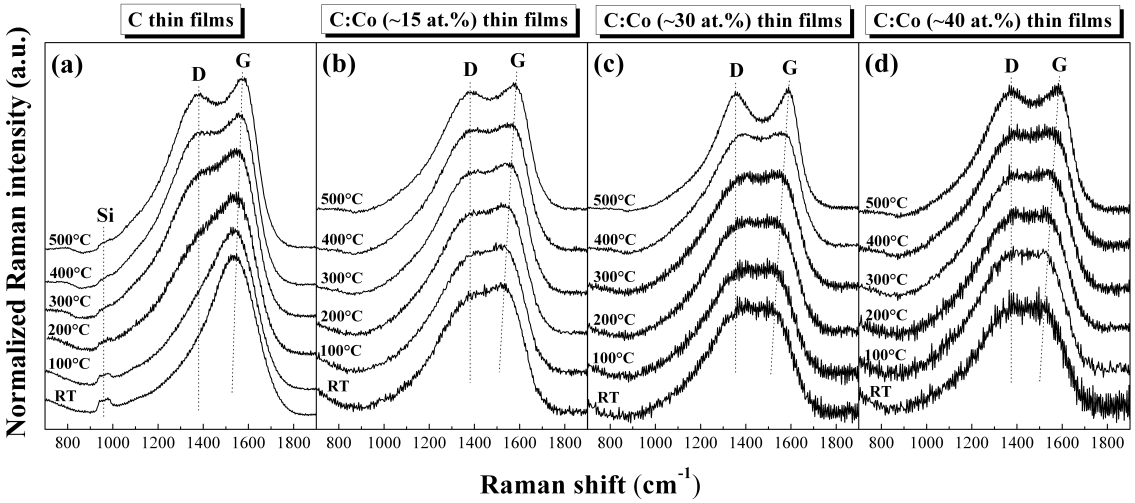

Figure 5.13: Normalized Raman spectra of C (a) [150], C:Co (∼15 at.%) (b), C:Co (∼30 at.%) (c) [150] and C:Co (∼40 at.%) (d) composite thin films grown at different substrate temperatures. The spectra were vertically shifted, but the original intensity ratios for each measured series are preserved.

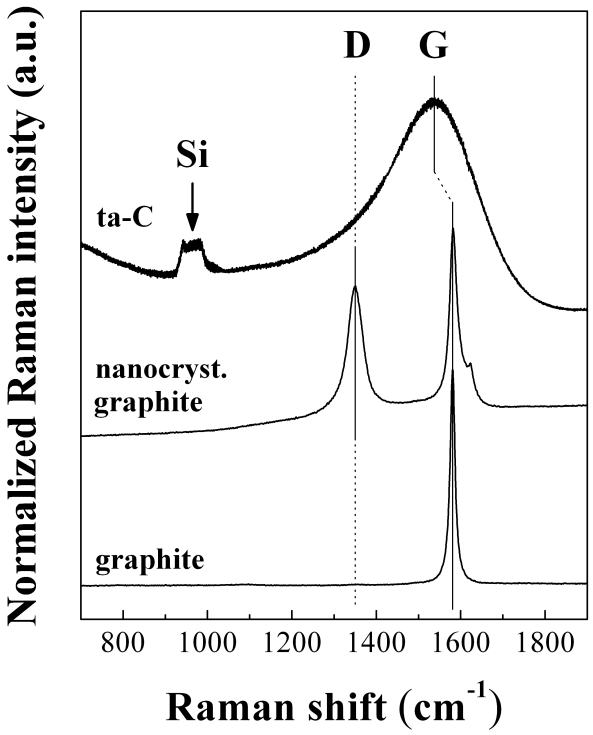

Figure 5.14: Raman spectra of tetrahedral amorphous carbon (ta-C), nanocrystalline graphite and graphite [156]. The spectra were vertically shifted, but the original intensity ratios for each measured series are preserved.

[157] and MS without additional bias [158]. The shape of the Raman spectra of the C film grown at RT resembles those of ta-C which indicates about a significant amount of sp^3-hybridized carbon. Above 100°C two individual contributions from the D and G peaks can be clearly observed. Both peaks become separated at 500°C. The G peak shift toward higher wavenumbers concomitantly with temperature should be noted.

On the other hand, the Raman spectra of C:Co composite films show an intense contribution of the D band already at RT (see figure 5.13 (b)-(d)) in contrast to the carbon reference films. No significant changes in the ratio of the peak intensities are observed with increasing temperature. Besides, the splitting of the D and G peak into individual peaks becomes slightly observable at 300°C in C:Co (∼15 at.%) films and at 400°C for higher Co contents, and can be clearly seen at 500°C. The shape of the Raman spectra differs among the respective Co contents, in particular at 500°C. For a Co content of ∼30 at.% the most pronounced separation of the D-G band is observed. In C:Co (∼15 at.%) films the G peak intensity is always slightly higher than the intensity of the D peak, while for a higher Co content in the films an almost equal peak intensity is observed over the whole temperature range of the study, except for C:Co (∼30 at.%) films grown at RT. Similar to carbon reference films, the G peak shifts toward higher wavenumbers concomitantly with temperature for all Co contents.

To emphasize the metal effect on carbon, figure 5.15 shows the normalized Raman

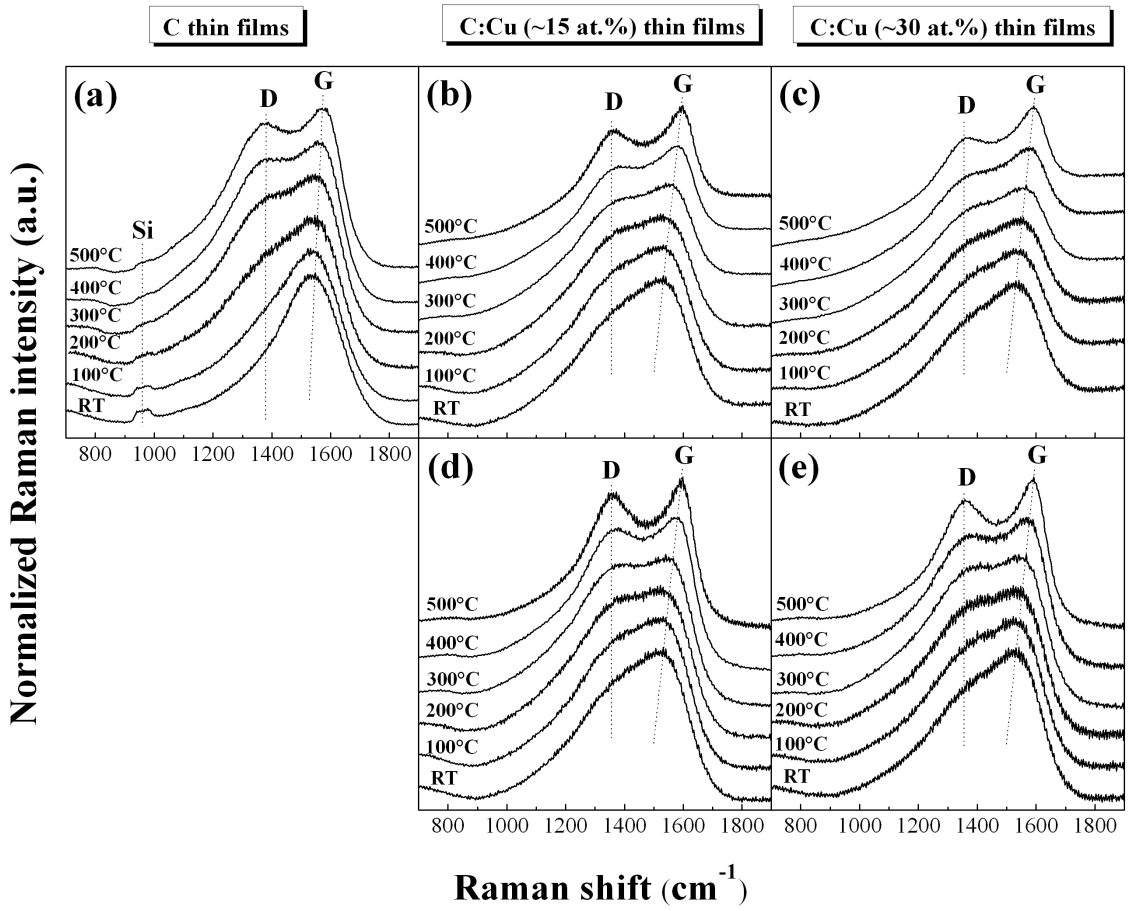

Figure 5.15: Normalized Raman spectra of C (a), C:Cu (∼15 at.%) ((b) and (d)) and C:Cu (∼30 at.%) ((c) [150] and (e)) composite thin films grown at different substrate temperatures. In (d) and (e) the photoluminescence background is subtracted from the spectra. The spectra were vertically shifted, but the original intensity ratios for each measured series are preserved.

spectra of C:Cu (∼15 at.%) and C:Cu (∼30 at.%) films together with the spectra of carbon reference films. Carbon luminescence contributes to the Raman spectra of C:Cu films. The higher background intensity at the end of the measurement range in comparison to the beginning for the composite films which is not observed for carbon reference and C:Co films clearly indicates about the superposition of the Raman spectra of C:Cu films by photoluminescence. It has been reported that copper is a prominent luminescence activator in II-VI compounds [159] and the effect of copper nanoparticles on the luminescence of films such as zinc oxide, alumina or silica glass has been reported [160, 161]. In order to avoid a misinterpretation of the C:Cu Raman spectra the luminescence background was subtracted (see figure 5.15 (c) and (d)). This is also important with regard to the fitting of the Raman spectra. In the following only the corrected Raman spectra will be considered. The Raman spectra of C:Cu composite films grown at low temperatures show a stronger contribution of the D band than carbon reference films, but a lower one than C:Co composites. Besides, the spectra for both Cu contents are very similar in the investigated temperature range. The intensity of the D peak relative to that of the G peak increases up to ∼300°C, while

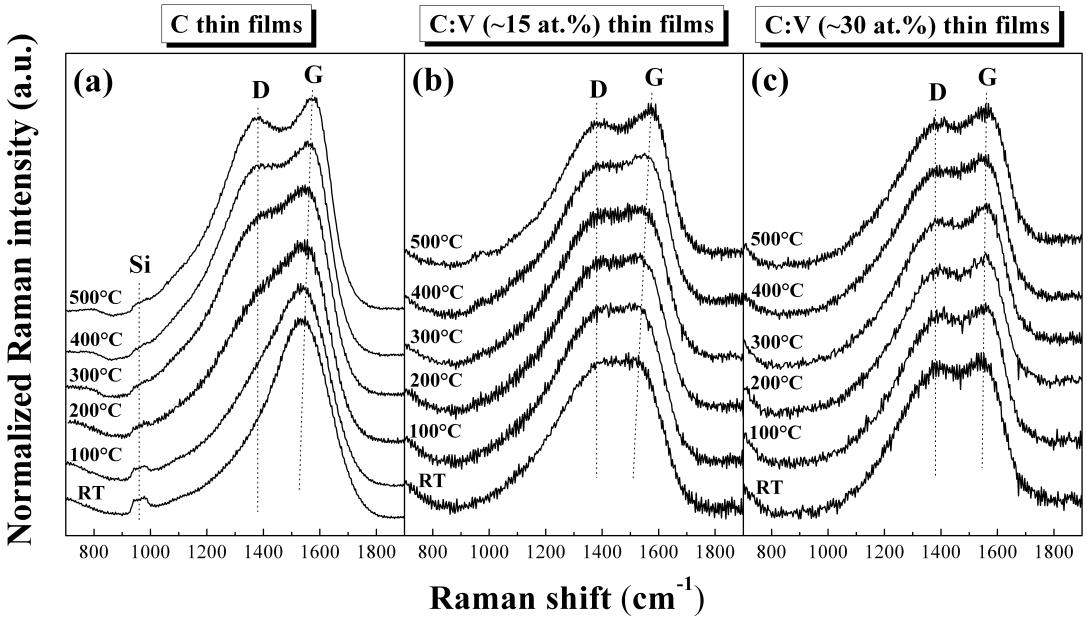

Figure 5.16: Normalized Raman spectra of C (a), C:V (∼15 at.%) (b) and C:V (∼30 at.%) (c) [150] composite thin films grown at different substrate temperatures. The spectra were vertically shifted, but the original intensity ratios for each measured series are preserved.

no considerable changes are observed at higher temperatures. The splitting of the D and G peaks into individual peaks becomes slightly observable at 300°C and can be clearly identified at 500°C. A more pronounced separation of the D-G band than in carbon reference films is observed at 500°C. Similar to carbon reference films and C:Co composites, a blue shift of the G peak with temperature is observed.

The normalized Raman spectra of C:V (∼15 at.%) and (∼30 at.%) films are shown together with the carbon reference spectra in figure 5.16 (a)-(c). Similar to C:Co films, the Raman spectra of C:V films exhibit a strong contribution of the Raman D band already at RT. In contrast to carbon reference films, C:V (∼15 at.%) composites show only little changes in the shape of the Raman spectra with temperature. Above 300°C two individual peaks start to emerge with the D peak intensity being slightly lower than that of the G peak. Besides, the G peak is shifted to higher wavenumbers with increasing temperature as in the case of carbon reference films. For C:V (∼30 at.%) films no considerable changes in the Raman spectra are observed with increasing temperature. On the other hand, the splitting of the D and G peaks into individual features is already observed at RT.

Fitting of Raman spectra

In order to obtain a more quantitative understanding of the structural changes of the films in dependence of growth temperature, TM type and content, the Raman spectra were fitted by a three line model as described in chapter 4 (see section 4.4.2). For

the fitting of the nanocrystalline graphite Raman spectrum an additional Lorentzian line for the peak ∼1620 cm^{-1} was used. In the following the discussion will focus on the position and width of the G peak and the intensity ratio of D and G peak I_D/I_G. These fitting parameters are plotted in figure 5.17 versus deposition temperature for both C reference and C:TM films. The corresponding G peak positions of ta-C, nanocrystalline graphite and graphite are also indicated in the figures in the form of horizontal lines for comparative purpose. Besides, for the sake of completeness, all the fitting parameters (D and G peak position and widths, coupling coefficient q and I_D/I_G ratio) are summarized in table 7.1-7.5 of appendix 7.1 for C reference films, C:TM composites, ta-C, nanocrystalline graphite, and graphite.

The G peak position increases concomitantly with temperature for carbon reference and C:TM films, except for C:V (∼30 at.%) films (figure 5.17 (a)-(c)). For carbon reference films the G peak shifts upwards from 1539 cm^{-1} at RT to 1575 cm^{-1} at 500°C. At the highest temperature its position is close to that of graphite or nc-graphite which is 1581 and 1582.5 cm^{-1}, respectively (figure 5.17 and Refs. [135, 162]). For C:Co composites deposited at RT, the G peak is down shifted with increasing metal content (1538 and 1518 cm^{-1} for ∼15 and ∼40 at.% Co in the films, respectively). The G peak position of C:Co (∼15 at.%) films almost coincides with that of pure carbon films in the whole temperature range, while the slope is larger for C:Co composites with a higher Co content. At 500°C C:Co (∼30 at.%) films exhibit a higher G peak position (1583 cm^{-1}) than the other Co contents (1576 and 1578 cm^{-1} for ∼15 and ∼40 at.% Co, respectively) and carbon reference films. All these values are close to that of graphite and nc-graphite. C:Cu composites exhibit a similar G peak position between RT and 300°C as pure carbon films, while at higher temperatures the G peak position is well above that of C reference films. At 500°C its position (1588 and 1584 cm^{-1} for C:Cu (∼15 at.%) and C:Cu (∼30 at.%) films, respectively) is close to that of graphite and nc-graphite. For C:V (∼15 at.%) films the G peak position behaves similar as for pure carbon films, except that the peak values are 2-6 cm^{-1} below that of the C reference films grown at the same temperature. For C:V (∼30 at.%) films the G peak shows a weak growth temperature dependence and varies between 1552 and 1565 cm^{-1}.

For carbon reference and C:TM films the G peak width shows an overall decrease when the temperature increases from RT to 500°C. This is not the case for C:V (∼30 at.%) films which show no considerable changes in the whole temperature range (figure 5.17 (f)). For carbon reference films the G peak width decreases almost linearly with temperature from 204 cm^{-1} at RT to 143 cm^{-1} at 500°C. For C:Co composites the films with the lowest Co content show the smallest decrease in G peak width when the temperature increases from RT to 500°C. Besides, for C:Co (∼15 at.%) and C:Co (∼40 at.%) films the width of the G peak decreases concomitantly with temperature, while for C:Co (∼30 at.%) films the width first slightly increases reaching a maximum at 200°C and then decreases at higher temperatures. At 500°C the C:Co (∼30 at.%) film exhibits the narrowest G peak (121 cm^{-1}), whose value is clearly lower than that of C:Co (∼15 at.%) (146 cm^{-1}) and C:Co (∼40 at.%) films (139 cm^{-1}), and of corresponding carbon reference films. C:Cu films grown at low temperatures have a

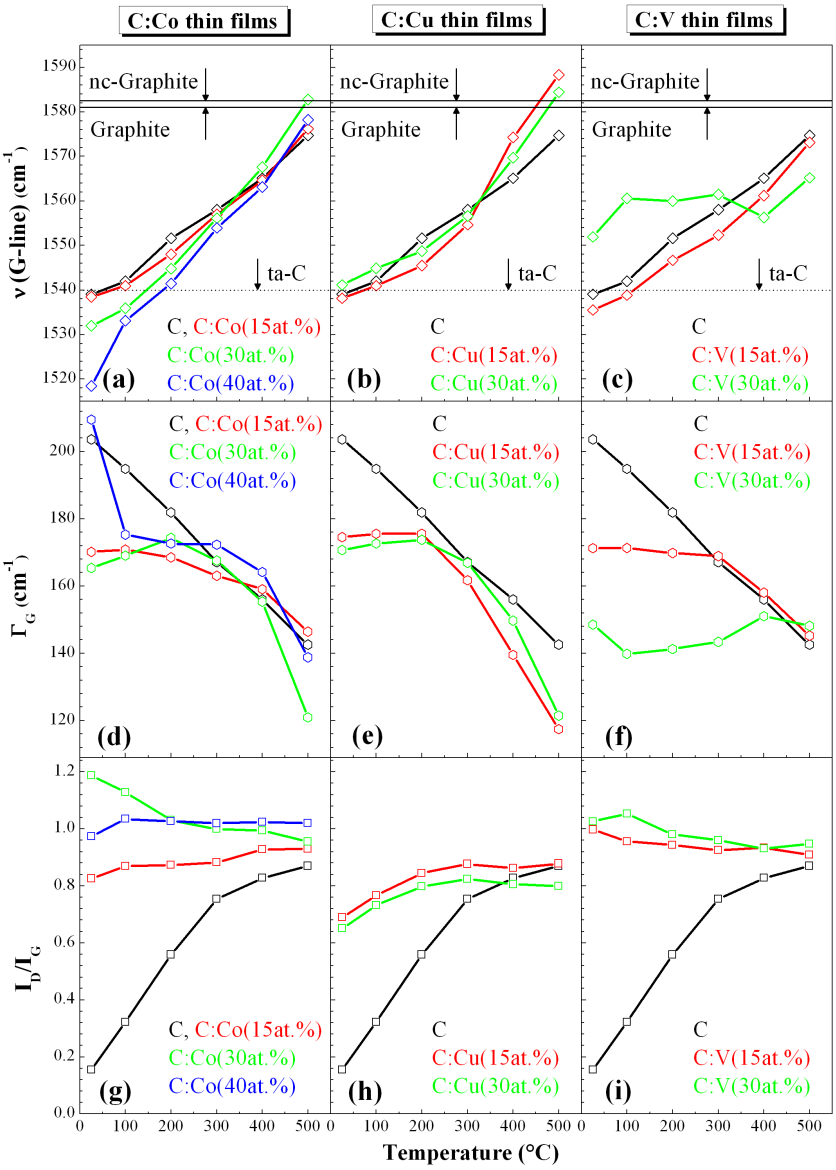

Figure 5.17: Position and width of the G peak and I_D/I_G ratio of C and C:TM thin films grown at different substrate temperatures. The lines are guide for the eye only. The corresponding G peak positions of nc-graphite, graphite and ta-C are additionally shown in the figures as horizontal lines for comparative purpose.

smaller G peak width than carbon reference films and show a similar behavior for both Cu contents in the whole temperature range. The G peak width slightly increases (from 171 to 174 cm^{-1} for C:Cu (∼30 at.%) films) or remains almost constant (∼175 cm^{-1} for C:Cu (∼15 at.%) films) when the temperature increases from RT to 200°C. Above 200°C the G peak width decreases concomitantly with temperature down to a value of 121 and 117 cm^{-1} at 500°C for C:Cu (∼30 at.%) and C:Cu (∼15 at.%) films,

respectively. For C:V (∼15 at.%) films the G peak width remains almost constant (∼170 cm^{-1}) between RT and 300°C, and decreases for higher temperatures having similar values as carbon reference films. In contrast, for C:V (∼30 at.%) films the G peak width varies slightly with temperature (140-150 cm^{-1}) but does not show any clear tendency.

For carbon reference films the I_D/I_G ratio increases concomitantly with temperature from 0.15 at RT to ∼0.9 at 500°C. C:Co composites grown at RT exhibit a significantly higher I_D/I_G ratio (0.8-1.2) than carbon reference films. Except for C:Co (∼30 at.%) films where I_D/I_G drops by ∼0.2 when the temperature increases from RT to 200°C, the peak intensity ratio shows only little variations with temperature. For C:Co (∼15 at.%) films, I_D/I_G slightly increases from 0.8 at RT to 0.9 at 500°C, whereas for (∼30 at.%) films I_D/I_G gradually decreases down to ∼1 at 500°C. Besides, in the C:Co (∼40 at.%) composites the I_D/I_G ratio of ∼1 remains almost constant. Among the C:Co composites the C:Co (∼15 at.%) films exhibit the lowest I_D/I_G value in the whole temperature range. At low temperatures (≤200°C) C:Cu composites have a clearly higher I_D/I_G ratio than carbon reference films, while its value is below that of C:Co composites. I_D/I_G slightly increases with temperature up to 300°C (from 0.7 and 0.65 to ∼0.9 and ∼0.8 for ∼15 at.% and ∼30 at.% Cu, respectively) while the peak intensity ratio remains almost constant at higher temperatures. In the whole temperature range of this study C:Cu (∼15 at.%) films have a slightly higher I_D/I_G ratio than C:Cu (∼30 at.%) films (figure 5.17 (h)). In C:V films the I_D/I_G ratio is ∼1.0 at RT, while it slightly decreases with temperature to ∼0.9 and ∼0.95 at 500°C for a V content of ∼15 and ∼30 at.% in the films, respectively.

In summary, all films C and C:TM films show an increase in G peak position and an overall decrease in G peak width when the temperature increases. An exception are C:V (∼30 at.%) films which exhibit a very weak growth temperature dependence. Below 300°C all C:TM films have a significantly higher I_D/I_G ratio than corresponding carbon reference films. The I_D/I_G value increases concomitantly with temperature for pure carbon films, while it remains almost constant for C:Co and C:V films. For C:Cu films I_D/I_G increases up to 300°C and remains constant at higher temperatures. Differences in the fitting parameters are observed among the respective TM types and contents.

5.1.5 Discussion

The results above demonstrate that the nanostructure of both composite constituents is strongly influenced by the growth temperature, metal type and content. For all C:TM films repeated nucleation occurs which prevents the formation of nanocolumns with a length equal to the film thickness. As film synthesis takes place far from thermodynamic equilibrium the nanostructure during thin film growth evolves in a competitive fashion between the thermodynamic and kinetic factors. Thermodynamically, the system tends to minimize its free energy by reducing the amount of matrix-inclusion interfaces, and

by the synthesis of crystalline material and stable phases as indicated by the phase diagram. On the other hand, the kinetic limitations induced by the low-temperature growth enable the synthesis of metastable phases or amorphous films, thus preventing the conversion to the more stable crystalline phase. Bulk diffusion is negligible because the film deposition takes place well below the melting point of the metal or the respective carbide and cs TEM imaging does not show any segregation phenomena. Thus, surface diffusion of the different atomic species determines the structure evolution during film growth and is responsible for the phase separation into dispersed phase and matrix. Many diffusion paths exist: C and TM self diffusion, diffusion of C on metal, diffusion of metal on carbon, and the diffusion of metal and carbon across the C/TM boundary. Accordingly, in the following it is to clarify which diffusion paths are the limiting factors determining the film structure. As the morphology of the dispersed phase depends on the growth conditions, the first part of the discussion considers the influence of growth temperature and Co content on the nanoparticle size and shape. In the second part, the effect of the metal type on the morphology of the inclusion phase is discussed. The third part addresses the graphitization behavior of the carbon matrix. In the fourth part, the growth regimes of C:TM films are summarized, and the results are discussed on the basis of the mutual chemical C-TM affinity and temperature activated adatom diffusivity.

Temperature-content dependence of the dispersed phase in C:Co films

At low growth temperatures metal adatom mobility is low and prevents Co atoms from diffusion and seeking out equilibrium lattice sites resulting in the formation of metastable cobalt carbide phase. With increasing growth temperature the amount of the more stable metallic Co phase as indicated by the phase diagram increases owing to the higher mobility of as-deposited atoms. The cobalt carbide phase does not exist above 300°C as confirmed by XRD and TEM which is associated with the weak covalent bonding between C and Co atoms and the increase in surface diffusivity. In addition to the chemical state, also the phase state changes with increasing growth temperature. The very broad diffraction peak in the XRD pattern and the absence of lattice fringes inside the Co-rich grains for the C:Co composite grown at RT are compatible with the amorphous structure as reported in the literature for C:Co or C:Ni nanocomposite films grown at low temperatures [5, 6, 20, 22, 25, 33, 34, 101]. At elevated temperatures the higher adatom mobility results in the formation of the thermodynamically more stable crystalline grains at T$\geq$300°C. Both phase transformations are associated with the release of free energy of the system [2].

At the initial stage of thin film growth the 3D island mode for Co [163] leads to the formation of metallic islands which serve as a sink for subsequently deposited metal atoms [2, 164, 165], thus the film growth kinetics is expected to follow the nucleation - growth - coalescence stages. On the other hand, encapsulation of the islands by the surrounding carbon phase takes place due to the layer-by-layer growth mode of carbon [21]. If carbon exhibits a moderate solubility in the metal, carbidic clusters can form as in the case of C:Co composites grown at low temperatures at the conditions

far from thermodynamic equilibrium. Present TEM results show that at RT repeated nucleation results in a fine-grained structure. XRD also indicates a small grain size. The average diffusion length, which is determined by the ratio of surface diffusivity and growth rate, is low and prevents the metal adatoms to reach the existing nanoparticles before being covered. In addition, amorphous carbon can easily trap the as-deposited metal atoms which further promotes the repeated nucleation [166–168]. Defects in the carbon phase act as effective nucleation centers, while contamination of the surface also affects nucleation kinetics [78].

The increase in adatom mobility with substrate temperature results in an elongation of the nanoparticles in the film growth direction and also increases the nanoparticle diameter. The formation of larger grains at higher growth temperatures is similar to the observations in single phase films [78, 81]. The temperature induced surface diffusivity allows more adatoms to reach the boundaries of coexisting phases before being covered by subsequently deposited atoms. The probability of forming a carbon surface covering layer on the growth surface of the nanoparticles is reduced and therefore also the degree of repeated nucleation. Besides, at T$\geq$300°C the carbon phase is composed of GLC layers. This can further increase metal adatom mobilities, as the metal adatom diffusivity on the GLC matrix is expected to be larger than that on the amorphous carbon [164]. The nucleation theory for single phase thin films predicts a lower nucleation density and the formation of larger islands with increasing substrate temperature which is consistent with the observed grain coarsening with increasing temperature in the C:Co composite films [169]. On the other hand, the presence of the carbon matrix prevents the lateral development of Co nanoparticles, while it promotes their evolution in the film growth direction, i.e. the lateral phase separation. Besides, the formation of carbidic phase up to 300°C does not hinder the elongated growth of nanoparticles which might be related to the weak nature of Co-C bonds.

For higher Co concentrations in the films the encapsulation probability of the nanoparticles by the carbon matrix is reduced resulting in a larger nanoparticle diameter and, in the case of nanocolumns, also in a larger column length. The fact that larger nanoparticles are formed in the films exhibiting a higher metal content indicates that carbon diffusion on metal is not a limiting factor for the phase separation. A similar conclusion was drawn for C:Ni nanocomposite films grown by ion beam co-sputtering on different types of substrates [3].

The increase in grain size with both temperature and metal content due to the higher adatom mobilities should be attributed to the tendency of the system to minimize the free energy by reducing the amount of matrix-inclusion interfaces. However, the absence of nanocolumns with a height equal to the film thickness even at the highest growth temperature and Co content suggests that the energy barrier at the TM/C interface is too large to allow all C atoms to diffuse across the boundary.

As for the C:Co composites of the present study a globular-elongated growth transition is observed with increasing temperature, it can be expected that a further increase in temperature and metal content would increase the column height and their diameter.

However, a higher growth temperature gives rise to surface segregation of the metal phase [147] which indicates the occurrence of bulk diffusion. On the other hand, for a higher metal content in the film the width of the carbon matrix between the grains is reduced and island coalescence can occur. The ERDA depth profiles of the C:Co films with Co contents ≥30 at.% grown at 500°C show a Co concentration pile up at the surface, while this is not observed for a metal content of ∼15 at.% in the films. Abrasonis et al. [147] also showed for C:Ni films grown at 500°C by hyperthermal ion deposition that a higher metal content promotes the metal surface segregation at higher temperatures. It should be noted that due to the bombardment of the growing film with incoming energetic ions the adatom mobility is enhanced and the metal surface segregation occurs at Ni contents as low as 7 at.% becoming significantly more pronounced for higher Ni concentrations. The vertical phase separation and the formation of a continuous metal layer for larger metal contents was assigned to the tendency of the system to minimize the free energy by lowering the amount of interfaces between matrix and inclusion phase. The tendency of metal surface segregation is strongly affected by the kinetic factors depending on the interplay of metal atom mobility and the tendency of the carbon matrix to encapsulate the particles [147], which explains the homogeneous Co depth distribution in the films with the lowest metal content.

The formation of well-aligned nanocylinders embedded in a matrix has been reported for Fe-$LaSrFeO_4$ [170], $BaTiO_3$-$CoFe_2O_4$ [171], Al-Si [92, 94], Al-Ge [172], and various metal silicide-Si or germanide-Ge systems [173] by using conventional PVD techniques such as sputtering or pulsed laser deposition. All these systems exhibit eutectic phase diagrams with terminal phases that have limited solid solubilities similar to the Co-C system. Therefore phase separation during deposition occurs for a composition within the two-phase region. In binary systems with a significantly lower eutectic temperature than in the system Co-C (1320°C) like Al-Si (577°C) [35] and Al-Ge (420°C) [35] nanorod formation is obtained already at RT indicating about a considerable surface diffusion length. It should be noted that the adatom mobility is inversely proportional to the melting point of the compound. Therefore, for material systems with a high eutectic temperature above 1000°C the temperature during sputter deposition must be increased up to 300°C and additional bias voltage (-20 V) must be applied to obtain similar structures as for the systems with a low eutectic temperature. This indicates that a certain adatom mobility is necessary for the formation of well-aligned nanocylinders [173].

Systems like $CrSi_2$-Si (1305°C) [35] or $HfSi_2$-Si (1360°C) [35] have an eutectic temperature comparable with the system Co-C and show the presence of nanorods while the latter does not. This might be associated with the different matrix materials. In C:Co films the carbon matrix grows in a two dimensional layer-by-layer mode [21]. Graphite-like carbon structures are formed at higher temperatures (≥300°C). Such GLC structures form closed shells covering the growth surface of the nanoparticles. This stops further growth of nanoparticles in the perpendicular direction and causes repeated nucleation. Similar observations have been reported for C:Ni films grown by magnetron sputtering at elevated temperatures [18]. Thus, carbon adatoms on the metal nanoparticle surfaces which reach the TM/C boundaries have a relatively high

energetic barrier to cross the boundary and tend to stay at the metal surface thus extending gradually the carbon network over the metal nanoparticle surface. On the other hand, amorphous silicon or germanium do not form planar structures while the matrix exhibits a 3D structure surrounding the sidewall of nanowires. Besides, Wang et al. reported about columnar growth of Co nanoparticles in DLC by plasma-assisted processing [103, 104]. However, they used magnetron sputtering with reactive gases and additional bias voltage (-500 V) resulting in energetic particle bombardment during film deposition and thus enhanced adatom mobilities. Babonneau et al. also showed that ion assistance promotes the elongated growth of nanoparticles [174]. With increasing Co content in the films, the Co nanostructure developed from slightly elongated nanoparticles to nanorods with their diameter increasing. It should be noted that in contrast to GLC the DLC matrix exhibits a significant amount of sp^3-hybridized carbon atoms which might explain the nanorod formation similar to those embedded in amorphous silicon or germanium.

Self-assembled iron nanowires embedded in $LaSrFeO_4$ matrix are formed by pulsed laser deposition at 760°C in vacuum through the decomposition of $La_{0.5}Sr_{0.5}FeO_3$ perovskite [170]. No surface segregation of iron is observed at such high deposition temperatures indicating that the matrix acts as a stabilizer. The observations presented on the formation of nanowires above pose a challenge for the growth of nanocolumns with a height equal to the film thickness in the presence of a carbon matrix containing a significant amount of sp^2-hybridized carbon atoms, as from one side it tends to encapsulate the metal-rich nanoparticles, while from the other side does not prevent metal surface segregation. This might be probably valid for other layered materials such as CN_x or BN.

The present results show that the nanostructural evolution during growth evolves as a competition between the metal atoms which tend to accumulate in order to form large clusters and the carbon matrix tendency to encapsulate those clusters. The kinetic constraints imposed by the relatively low growth temperature and the covering growth by the carbon matrix limit the grain coarsening and the metal surface segregation. The results strongly suggest that the carbon diffusion on metal is not a limiting factor determining the film structure.

Metal type dependence

The nanoparticles in C:Cu (∼30 at.%) films show a similar growth temperature dependence as those in C:Co films, except that Cu grains are larger for the C:TM films grown at similar metal content and temperature. This might be associated with the lower melting point of Cu in comparison to Co and to the lower affinity to carbon for the former [35, 61] both factors enhancing the metal adatom mobility on carbon. In the C:V (∼30 at.%) films the grain size is lower than in C:Co and C:Cu films indicating about an even lower adatom mobility. Besides, in contrast to C:Co and C:Cu films, the effect of the growth temperature on the grain size is very low in C:V films, because a narrower section from the homologous temperature range has been investigated in the

latter case. This becomes evident by the similarity of the grain size in the C:V film grown at 500°C and of the C:Co film grown at RT. Both facts are assigned to the strong V-C interaction being responsible for the high melting point of vanadium carbide of 2670°C [35, 61] and inducing an overall low adatom mobility. Thus, repeated nucleation occurs rather than the diffusion toward the existing islands and the fine-grained structure is preserved in the whole temperature range of RT-500°C. The size of VC crystallites is rather influenced by the metal content than by the growth temperature as observed by XRD. As vanadium forms very stable carbides, cobalt forms metastable carbides at low temperatures, while copper practically forms no carbides, the different carbide forming behavior and the observed tendencies of the grain size in the different types of films as a function of growth temperature and metal content strongly indicate that the metal adatom mobility is inversely proportional to their affinity to carbon.

The comparison of the grain size in C:Cu and C:Co films with ∼30 at.% metal content shows that the nanoparticle diameter in C:Cu films grown at RT is similar to those of elongated nanoparticles in C:Co films deposited at 300°C even though the lower growth temperature for the former type of film induces a lower average adatom mobility. This observation indicates that the diffusivity of metal on carbon and across the C/TM boundary is not a limiting factor determining the nanostructural evolution. Consequently, also the self diffusion of metal atoms is not a limiting factor. However, even though Cu adatom mobility is higher than those of Co adatoms also for C:Cu films no nanorods are formed up to the highest growth temperature of the study of 500°C suggesting that the diffusivity of carbon across the TM/C boundary is a limiting factor for the film structure.

On the other hand, the fine-grained structure in C:V films in the whole temperature range of the present study suggest that for elements with a strong affinity to carbon such as vanadium the metal diffusivity on carbon is a limiting factor determining the film morphology. It should be noted that C:Ti nanocomposite films with a Ti content of 20 at.% grown by magnetron sputtering in the temperature range of RT-800°C exhibit a columnar structure [32]. As Ti has a comparable affinity to carbon like V the presence of nanorods for the former might be related with plasma assistance of the growing film during magnetron sputtering in comparison to ion beam sputtering, thus imposing a higher adatom mobility. Furthermore, the increase in width of the TiC columns with deposition temperature is attributed to the higher maximum growth temperature of 800°C thus a higher adatom mobility when compared with C:V films.

Carbon graphitization

A phenomenological relationship between the Raman spectra and the carbon bonding structure is provided by the *three-stage model*, also named *amorphization trajectory*, proposed by Ferrari, Robertson and Rodil [42, 56, 138]. This model, which was already introduced in section 4.4.2, allows the characterization of the carbon bonding structure in C and C:TM films by two important spectroscopic parameters, the Raman G peak position and the intensity ratio of the D and G peaks, I_D/I_G.

Before starting the discussion of the Raman spectra and the obtained fitting parameters, it is important to point out two things. First, the carbon is not crystalline, neither in the carbon reference nor in the metal containing composite films. This becomes evident by comparing the Raman spectra of C and C:TM films (figure 5.13, 5.15, and 5.16) with that of nanocrystalline graphite (figure 5.14). Even at the highest growth temperature of 500°C the carbon structure in these films is far from nc-graphite. Second, sputtered hydrogen free a-C films always have a low sp^3-content ($\leq$20%) [42, 56]. Therefore, the carbon bonding structure in all the films belongs to stage 2 of the *three-stage model*. This stage, in terms of disorder, can be described as an intermediate state between nanocrystalline graphite and amorphous carbon. In this stage, the presence of the D band is connected to the presence of sixfold aromatic rings in the sp^2 phase, while the I_D/I_G ratio reflects the cluster size in disordered carbons [56]. According to the *three-stage model*, all C:TM films contain three types of carbon: graphitic and amorphous sp^2 carbon, and amorphous sp^3 carbon. Furthermore, according to the G peak position and I_D/I_G ratio, the predominant structure of the carbon phase in C:TM films consists of nc-graphite and a-C with approximately 10% sp^3 carbon [56].

The above presented Raman spectra of C:TM films (figure 5.13, 5.15, and 5.16) differ in shape when compared to carbon reference films, in particular at low temperatures, which clearly demonstrates the metal impact on the surrounding carbon matrix. In addition, the spectroscopic features of C and C:TM films change differently when varying the growth temperature which implies that the carbon phase undergoes different pathways toward graphitization. Besides, also among the different types of composite films and for the different metal contents differences in the shape of the Raman spectra are observed which are reflected by their fitting parameters and indicate differences in the sp^2 bonding structure of the matrix.

The carbon reference film deposited at RT (G peak at 1539 cm^{-1}, I_D/I_G=0.15) belongs to the end of stage 2 of the *amorphization trajectory* which is amorphous carbon. Such structures are characterized by a completely disordered, almost fully sp^2-bonded carbon network consisting of distorted sixfold rings and rings of other orders with ~20% sp^3 hybridized carbon [56]. The small size of sixfold ring clusters is an indication for the low self diffusion of carbon atoms at RT. The small cluster size is additionally indicated by the blue shift of the D peak, which is close to 1390 cm^{-1} (see appendix 7.1, table 7.1), compared to the D band position of graphite-like carbon or nanocrystalline graphite (1350-1360 cm^{-1}) [42, 56, 138], because smaller clusters result in the D line blue shift [56]. Carbon tends to graphitize with the increase in growth temperature due to the higher adatom mobility as indicated by the increase in I_D/I_G ratio (increase in sixfold ring cluster size) and G peak position (increasing order within the clusters).

At RT, HRTEM observations do not show any layer-like structures of the carbon matrix. However, Raman spectroscopy highlights that some local sixfold ring clustering takes place which is promoted by the presence of the metal. Thus, although surface diffusion is strongly limited and the nanoparticle growth is dominated by nucleation it still enhances the sixfold ring clustering significantly. Furthermore, such a considerable

enhancement also occurs for relatively low (∼15 at.%) metal contents in the composite films suggesting that the metal-rich nanoparticles, even at a small size, act as effective templates for nucleation and growth of graphitic carbon clusters. The catalytic activity of various transition metals at low concentrations has also been reported in Ref. [100]. At higher temperatures, when surface diffusion becomes significant both techniques, Raman and HRTEM, show the features characteristic for a layer-like ordering of the carbon matrix.

At low deposition temperatures (≤200°C) the transition metal significantly enhances the sixfold ring clustering of the carbon phase since the I_D/I_G ratio is clearly higher than in corresponding carbon reference films. Similar observations have been reported for Ni [20, 158, 175]. The enhancement occurs independently of the nanoparticle size, shape, and phase (metallic or carbidic), and TM content, if carbon is present in excess because the Raman spectra of VC reference films do not show any features characteristic for amorphous or ordered carbons coexisting with the metal carbide nanoparticles. The degree of enhancement, i.e. the size of the graphene-like sp^2-bonded carbon clusters, depends on the transition metal type and content, and decreases for ∼30 at.% metal in the order Co > V > Cu. The differences in sixfold ring clustering between C and C:TM films are the largest at RT and become smaller at higher temperatures due to the temperature induced clustering in carbon reference films. In C:Cu films the increase in I_D/I_G ratio up to 300°C also indicates the temperature mediated sixfold ring clustering, while the cluster size remains constant at higher temperatures. For C:V and C:Co films the cluster size is almost independent of the growth temperature.

According to equation 4.4 the cluster size in C and C:TM films is always below 1.5 nm. However, the HRTEM images of C:Co and C:Cu films grown at T≥300°C show graphene layers that are significantly larger than this value. Therefore, the I_D/I_G ratios corresponding to distances below 1.5 nm have to be attributed rather to defects within the layers [131]. The curvature of the layers might also explain the discrepancy between the size of graphitic crystallites obtained from Raman and TEM [110]. As TEM does not show any layer-like ordering at RT, in this case I_D/I_G might be associated with the size of graphene-like (sixfold ring) sp^2-bonded clusters.

The catalytic graphitization of carbon by various transition metals has been known for a long time [176, 177] and also their importance as catalysts in the synthesis of carbon nanotubes [178–181] is well known even if there is still a discussion about the detailed mechanism. Konno et al. suggested that graphite-like carbon in sputter deposited C:Co films is produced via decomposition of cobalt carbide phase during the deposition [25, 33]. However, this would only explain the graphite formation in systems forming metastable carbides. In contrast, investigations on C:Co films in this study and on C:Ni films by Abrasonis et al. [20] show an enhanced aromatic clustering independently from the Co and Ni phase state. In many cases the graphite formation is referred to as metal mediated crystallization or, in the case of carbides, carbide mediated crystallization based on a dissolution-diffusion-precipitation mechanism [10, 177]. The proposed view of this process is that carbon atoms dissolve into the metal, thus supersaturating it with respect to the more stable crystalline phase due to the higher

free energy of the amorphous state. The supersaturation at the carbon/metal interface leads to a concentration gradient being the driving force for C diffusion through the metal and the precipitation on the surface as graphite [110]. However, the significant bulk diffusion of carbon atoms and precipitation on the nanoparticle surface would prevent the pronounced elongated structure of nanoparticles reported in the literature [18, 20, 25] and observed in this study for C:Co and C:Cu films. In addition, transition metals (T, V, Zr, W, Co, Ni, and Cu) significantly enhance the sixfold ring clustering of the carbon phase in sputter deposited C:TM films already at RT [20, 100, 150, 158] where adatom mobilities are strongly limited, i.e. bulk diffusion can be neglected. Carbon atom surface diffusion on metal-rich particles is proposed to be a key step during carbon nanotube growth [178–181] and is proposed to be responsible for the enhanced sixfold ring clustering during the growth of C:Ni composites [20]. The results of the present study from the complementary analysis of dispersed phase and matrix by TEM and Raman spectroscopy strongly suggest a similar mechanism to explain the enhanced aromatic clustering by vanadium, cobalt, and copper. Within this picture the metal nanoparticle surfaces act as templates or fast diffusion paths to enhance the ring structure nucleation and growth.

HRTEM shows that the graphitic planes follow the boundaries of metal-rich nanoparticles which points out that the excess carbon atoms as-deposited on metal surfaces diffuse toward the grain boundaries of the nanoparticles where carbon segregates by forming graphene layers. The so-formed graphitic planes might provide a platform for graphitic nanostructure formation and subsequent layers can built up laterally, which is confirmed by TEM observations (see figure 5.7 (b) and 5.10). In addition, investigations on carbon:metal, boron nitride:metal or carbon nitride:metal nanocomposites show that graphitic, CN_x (carbon nitride) or BN (boron nitride) planes which follow the boundaries of the nanoparticles are formed for different metals like Fe [21, 174, 182, 183], Ni [17, 18, 20, 102], Co [4, 22, 25, 150], Cu [24, 150] and Ag [10, 23] confirming the assumption above that the metal-rich nanoparticles serve as a platform or a template for the formation of layered structures.

The pv-TEM image of the C:Cu film grown at 300°C shows that graphene layers have formed only near the interface between the of Cu nanoparticles and the carbon phase while the latter appears amorphous for a larger distance to the nanoparticles. This observation indicates that graphitization occurs mostly at the interface consistent with the proposed mechanism that carbon surface diffusion on metal-rich nanoparticles and not bulk diffusion of carbon in the metal is responsible for the graphitic clustering.

The fact that metal-rich nanoparticles act as effective templates for nucleation and growth of carbon graphitic structures at temperatures as low as RT while on the other hand the sixfold ring clustering is strongly retarded in pure carbon films indicates that the carbon surface self diffusion is significantly lower than the diffusion of carbon on metal.

The curved graphitic shells grow parallel to the surface of the nanoparticles whose spatial arrangement limits the size and imposes curvature of the layers which prevents

the formation of large planar graphitic structures and explains why the carbon bonding structure in C:TM films is far from nanocrystalline graphite. Accordingly, the morphology of the dispersed phase (nanoparticle size and shape) strongly influences the bonding structure of the carbon matrix [146] which is reflected by their Raman spectra.

This becomes evident by comparing the changes in the carbon bonding structure with increasing growth temperature in carbon reference and C:V (∼30 at.%) films. In pure carbon films there are no spatial restrictions which hinder the growth of planar graphitic structures. Thus their formation and growth with increasing temperature is observed by Raman spectroscopy (increase in G peak position and I_D/I_G ratio). However, in these films the carbon bonding structure is far from nanocrystalline graphite which is related to the low surface mobility of carbon atoms as the growth temperature is well below 1000°C where the significant graphitization in pure carbon occurs [10, 102]. In the C:V films the carbidic nanoparticles enhance the sixfold ring clustering of the carbon phase at temperatures as low as RT, but on the other hand the fine-grained structure imposes a high degree of curvature of the layers which results in a significant amount of non-sixfold rings in the sp^2-coordinated basal planes which redshifts the G peak (∼1560 cm^{-1}) in comparison to graphite or graphite-like carbon, changing the structure of the carbon matrix rather to the fullerene-like than to the graphene-like. Besides, the overall low upward shift in G peak position with growth temperature is assigned to the slight increase in grain size, i.e. less degree of curvature of the layers resulting in a slightly higher amount of sixfold rings in the clusters. This indicates that the nanoparticle imposed curvature stabilizes the carbon phase but also results in a low degree of graphitization.

On the other hand, for C:Co and C:Cu films the increase in grain size and the formation of elongated nanoparticles at higher growth temperatures results in a lower degree of curvature of the layers and therefore a lower ratio of non-sixfold atomic structures which is indicated by the upward shift of the G peak. In C:V (∼15 at.%) films the increasing ratio of sixfold rings (upward shift of the G peak) concomitantly with temperature should also be related to the formation and growth of carbide crystallites as indicated by XRD measurements.

At 500°C the C:TM films exhibit different G peak positions and widths suggesting that the degree of ordering within the aromatic clusters depends on both the TM type and content. The Raman spectra of C:Cu and C:Co (∼30 at.%) films prepared at the highest temperature of this study show a better separation of the D-G band and a higher G peak position being slightly above that characteristic for graphite than the other films which indicates a higher ratio of sixfold rings in the clusters for the former. This might be related to the influence of the morphology of the dispersed phase on the structure of the carbon matrix as mentioned above. In C:Co nanocomposite films grown at 500°C, the clearly better separation of the D-G band and the higher G peak position for a Co content of ∼30 at.% than for the other Co atomic ratios (figure 5.17 (a),(d)) indicates a higher degree of ordering of the graphene-like sp^2-bonded clusters and suggest optimal conditions for the growth of carbon graphitic structures for an intermediate cobalt content. The observed tendencies indicate that the interface effects are maximized

at this intermediate Co content for the given growth conditions (deposition rate and temperature). At a low TM atomic ratio the increase in metal content results in a higher amount of interfaces, while for higher TM contents this increase leads to grain coarsening which reduces the concentration of interfaces [21, 22, 25]. Such a behavior might explain the optimal mechanical properties of the C:TM nanocomposites observed at a certain C/TM composition [15, 16] as the interfacial phase is expected to stabilize the cohesion of the whole nanocomposite structure [184] with the maximum enhancement at an optimal ratio of matrix, interface, and dispersed phase.

Growth regimes of C:TM films deposited by IBS

Figure 5.18 summarizes the growth regimes of C:TM films grown by IBS as a function of the mutual chemical C-TM affinity and growth temperature. At low growth temperatures the surface mobility of the adatoms is low, thus the repeated nucleation dominates the nanostructure formation and all C:TM films show the presence of globular nanoparticles (NPs) embedded in an amorphous carbon matrix. The Cu and V rich nanoparticles are crystalline while those in the C:Co films exhibit an amorphous structure. For the C:Cu and C:Co films, an increase in the ad-atom surface diffusivity results in the formation of elongated nanoparticles and an increase in the nanoparticle diameter accompanied with the formation of a GLC matrix. For C:V films, the increase in the substrate temperature results in the increase of the nanoparticle diameter while retaining the globular morphology. For C:V films, the VC grains are encapsulated by FLC matrix for T$\geq$300°C. Concerning the chemical state, Cu (V) is metallic (carbidic) in the whole temperature range while Co shows a carbidic$\rightarrow$metallic transition when the surface ad-atom diffusivity increases. In addition, the nanoparticle diameter or ad-atom mobility at a given temperature decreases when the C-TM affinity increases.

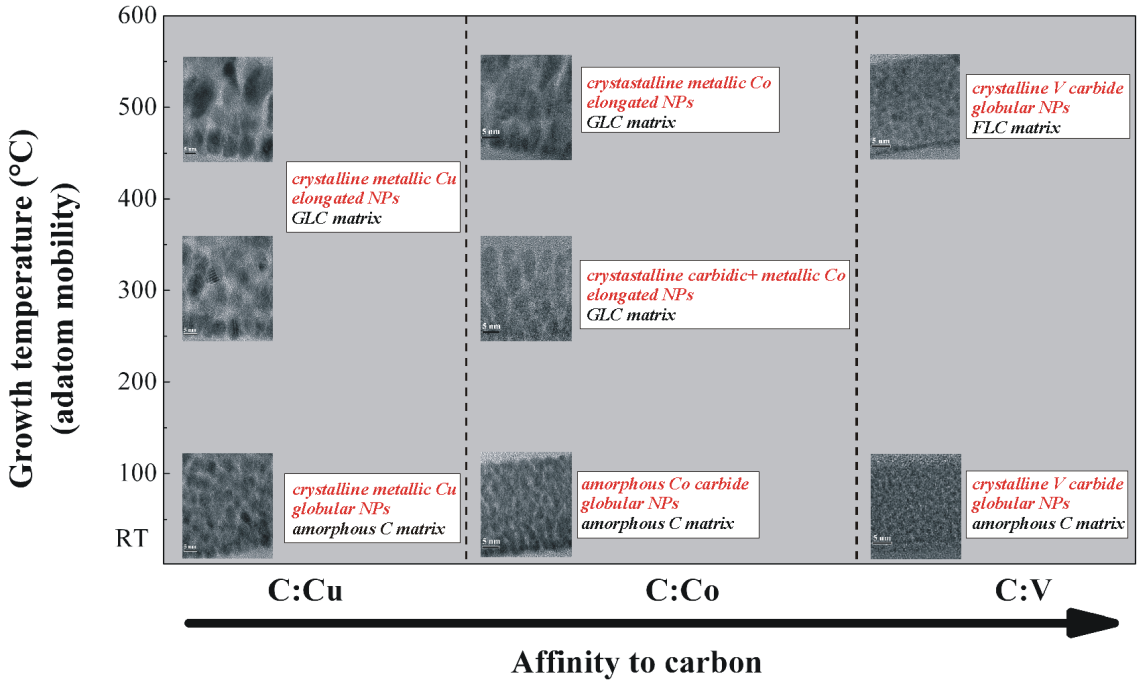

Figure 5.18: Structure zone diagram for IBS grown C:TM films as a function of the mutual C-TM chemical affinity and substrate temperature. NPs denotes nanoparticles.

5.2 Phase separation during post-deposition annealing of the nanocomposite thin films

Carbon and C:TM films, which were deposited at T_s=200°C, were postannealed at T_a=300-700°C. The effects of annealing on the film depth profiles, phases, and morphology of the films are described in sections 5.2.1, 5.2.2, 5.2.3, and 5.2.4. In section 5.2.5 the results from sections 5.2.1-5.2.4 are summarized and discussed.

5.2.1 Film composition and depth profiles of annealed samples

Figure 5.19 shows the ERDA depth profiles of C:TM films deposited at T_s=200°C and of the C:TM films which were postannealed at T_a=700°C. The film areal densities and atomic ratios of the major film constituents and impurities of as-deposited C:TM films are summarized in table 5.5.

The ERDA depth profiles of as-deposited films show a homogeneous distribution of carbon and TM over the film thickness consistent with the observations reported in section 5.1.1. The amount of impurities in the film is low in comparison to carbon and the metal (see table 5.5). In addition, at the film-substrate interface the concentrations of both major film constituents decrease rapidly to zero. The ERDA depth resolution and the origin of impurities in the films were already discussed in section 5.1.1. The C:Co and C:Cu films annealed at 700°C show an inhomogeneous depth distribution profile (figure 5.19 (b) and (d)). A metal concentration pile up is observed at the film surface and a depletion at the interface (∼0 at.% of TM). The TM atomic ratio increases up to a maximum value of ∼60 and ∼100 at.% for the annealed C:Co and C:Cu films, respectively. The above observations indicate that significant bulk diffusion of the metal occurs in C:Co and C:Cu films at T_a=700°C which alters the initial film structure. ERDA measurements show that annealing at 500°C leads to a slight surface segregation of the metal in the C:Cu composite (see figure 5.20). The corresponding C:Co sample exhibits no considerable changes in comparison to the as-deposited film which is a hint that the C:Co composite structure is thermally stable at least up to 500°C and bulk atomic transport phenomena occur at higher annealing temperatures. The slightly higher Cu content near the surface at 500°C might be associated with the lower melting point of copper in comparison to cobalt, i.e. a higher diffusivity. It

Table 5.5: Film areal densities t, compositions and $t_{TM}/(t_{TM} + t_C)$ ratios of C:Co (∼35 at.%), C:Cu (∼40 at.%), and C:V (∼35 at.%) films as-deposited at 200°C.

Film type	Film areal density t (10^{18} cm^{-2})	Atomic ratio (at.%) C	O	H	TM	$t_{TM}/(t_{TM} + t_C)$
C:Co (∼35 at.%) 200°C	0.91	64.7	0.7	0.9	33.7	0.34
C:Cu (∼40 at.%) 200°C	0.80	56.3	0.6	1.8	41.3	0.42
C:V (∼35 at.%) 200°C	0.93	61.1	1.0	1.1	36.8	0.38

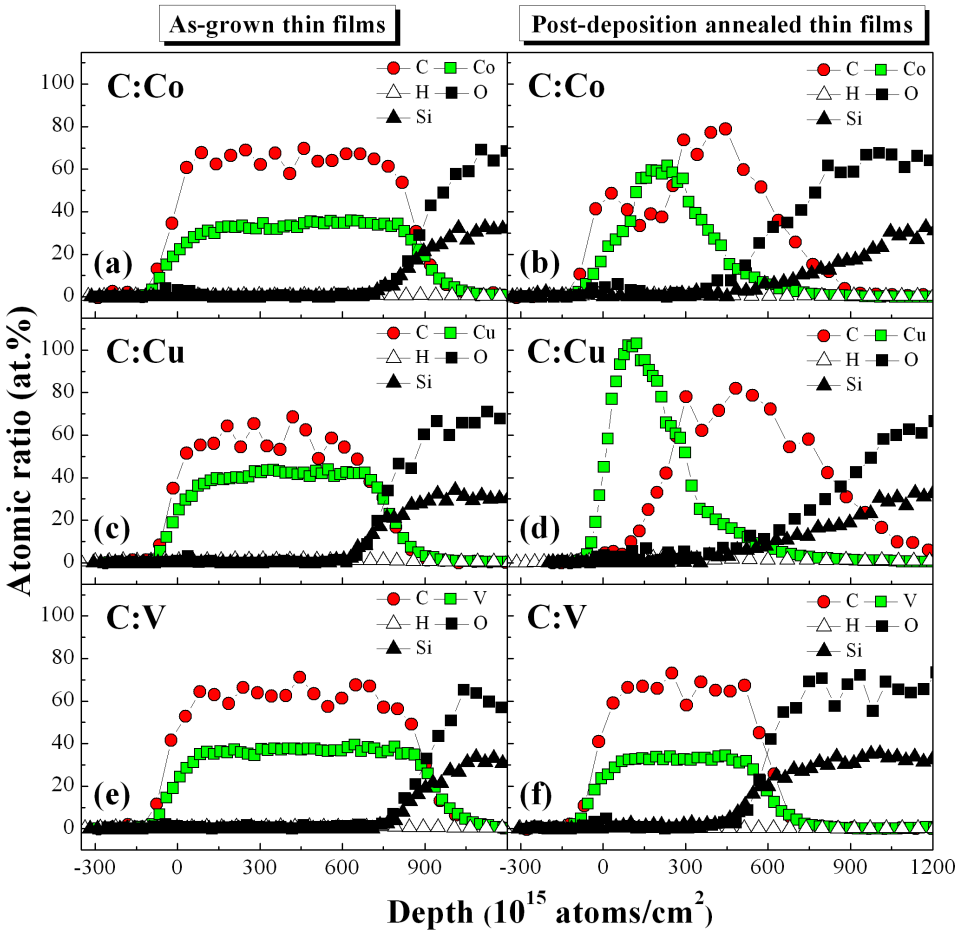

Figure 5.19: ERDA depth profiles of C:Co(∼35 at.%) ((a) and (b)), C:Cu(∼40 at.%) ((c) and (d)), and C:V(∼35 at.%) ((e) and (f)) films as-deposited at 200°C and of films which were postannealed at Ta=700°C.

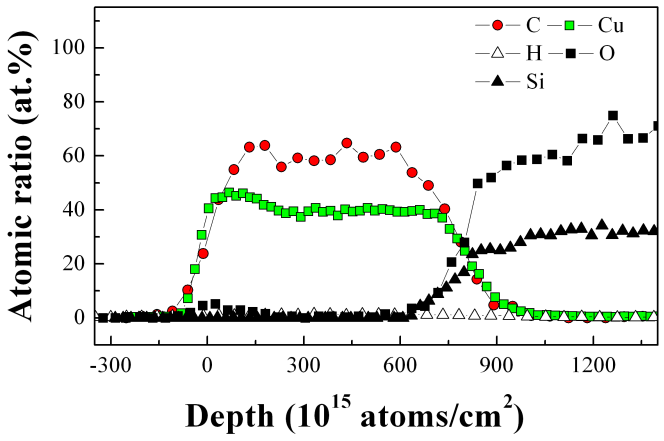

Figure 5.20: ERDA depth profile of the C:Cu(∼40 at.%) film postannealed at Ta=500°C.

should be noted that the C:V film presented in figure 5.19 (f) exhibits a lower film areal density, i.e. a lower film thickness, in comparison with the film shown in figure 5.19 (e), which is due to a lower film thickness of the original sample in the former case and not due to material loss during post-deposition annealing.

5.2.2 Dispersed phase: XRD investigations

Figure 5.21 shows the XRD patterns of as-deposited and of postannealed C:TM films. The estimated crystallite size from the width of diffraction peaks by the Scherrer formalism is illustrated in figure 5.22. The patterns are intermitted between 53° and 58° in order to blind out the broad peak around 55°, which is observed in some of the patterns, and is most probably related to the oxide layer on the Si substrate.

The effect of annealing on the nanoparticle phase structure in C:Co films is shown in figure 5.21 (a). The as-deposited film exhibits a broad diffraction peak at ∼43° which is present up to an annealing temperature of 400°C, while at higher annealing temperatures the peak becomes sharper and more intense. The broad feature at ∼43° of the as-grown film is assigned to the superposition of several diffraction peaks from cobalt carbide which is the majority phase and hcp Co existing as the minor phase as discussed in section 5.1. When T_a increases up to 500°C the peak maximum continuously shifts by ∼2° to higher diffraction angles which indicates that the metastable cobalt carbide phase starts to decompose above 200°C and hcp Co is formed. At T_a=500°C the peak is narrower than for lower annealing temperatures due to the absence of reflections from the cobalt carbide phase. The decomposition of cobalt carbide into hcp Co and carbon upon heating at 300-420°C has been reported in the literature [5, 6, 22, 33, 101]. Whether both metallic Co phases coexist at 500°C can not be determined unambiguously, but the relatively broad peak might be assigned to the overlapping of three peaks from the hcp Co phase, namely the (100), (002) and (101) reflection, and the (111) plane of the fcc Co phase. As T_a further increases up to 600°C the peak shifts slightly toward lower 2θ value. The calculated lattice spacing obtained from the peak center for the sample annealed at 500 and 600°C are 2.026 $\mathring{A}$ and 2.043 $\mathring{A}$, respectively. These values match well with those of the hcp and fcc Co lattice spacingsn of the (002) and (111) planes which are 2.023 $\mathring{A}$ and 2.046 $\mathring{A}$ [149], respectively, thereby confirming the phase transition from hcp to fcc structure. At T_a=550°C additional features at higher diffraction angles are observed which become more pronounced at higher annealing temperatures. The (200) reflection from fcc Co at 51.5° which is clearly visible at 600°C indicates that the phase transformation is complete at this annealing temperature. It has been reported that hcp Co existing at room temperature transforms to the fcc structure after annealing at ∼400 and ∼420°C in sputter deposited Co thin films and in bulk Co, respectively [35, 185]. However, the present observations indicate that the temperature of phase transition is shifted to a higher value in the Co-C system.

The increasing intensity and decreasing width of diffraction peaks above 550°C in-

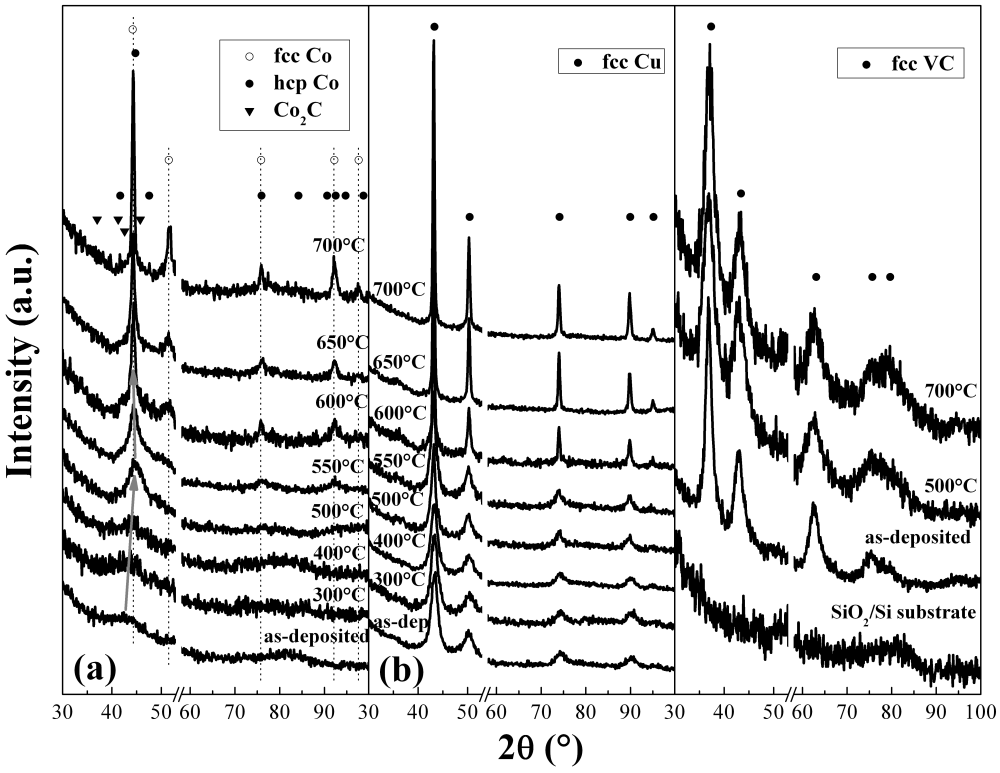

Figure 5.21: XRD patterns of C:Co (a), C:Cu (b), and C:V (c) composite thin films as-deposited at 200°C and of films which were postannealed at various temperatures. The arrows in (a) illustrate the shift of the peak maximum with increasing annealing temperature, and the dotted lines indicate the peak positions of fcc Co. A diffractogram of an uncoated SiO_2/Si substrate is given at the bottom in (c) for comparative purpose.

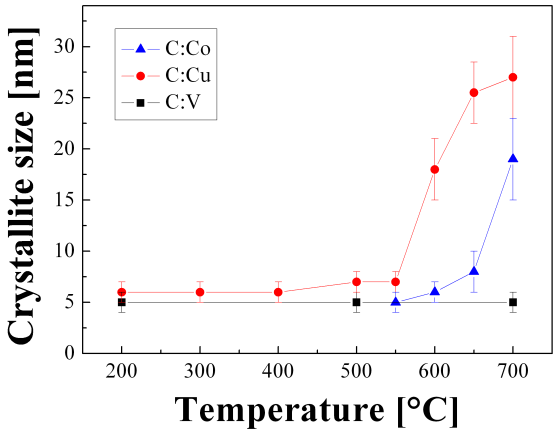

Figure 5.22: Crystallite size behavior in C:TM films with annealing temperature. The crystallite size was estimated from the (111) fcc Co, (111) and (200) fcc Cu, and (111) fcc VC peak widths in the XRD patterns by the Scherrer formula. The temperature of as-deposited films was 200°C.

dicates about the growth of Co crystallites (figure 5.22). It should be noted that the overlapping of several diffraction peaks from metallic Co or cobalt carbide phase prevents the estimation of the grain size at temperatures below 550°C.

Figure 5.21 (b) shows the XRD patterns of as-deposited and postannealed C:Cu films. The diffraction peaks correspond to the fcc Cu phase. No considerable changes are observed up to an annealing temperature of 550°C. At higher temperatures significant sharpening of the diffraction peaks occurs reflecting the increase in the average crystallite size from 7 to 27 nm as estimated from the width of diffraction peaks employing the Scherrer equation (see figure 5.22).

The diffraction patterns of C:V films grown at 200°C and of the annealed samples at T_a=500 and 700°C in figure 5.21 (c) show the peaks corresponding to the fcc VC phase. No changes are observed in the investigated temperature range indicating the stability of the dispersed VC phase and its morphology (figure 5.22). It should be noted that for the sample annealed at 700°C the broad peak ∼55° which is related to the SiO_2 underlayer is observed. Thus, the additional feature ∼80° might also be assigned to the substrate because the other peak intensities of fcc VC phase remain constant in comparison to T_a=500°C.

In summary, XRD reveals no changes in the phase structure of annealed C:V and C:Cu composite films upon annealing in the investigated temperature range of 300-700°C keeping the initial fcc VC and fcc Cu phase, respectively. In contrast, in the C:Co films cobalt carbide decomposes between 300 and 500°C into hcp Co and carbon, and hcp Co further transforms to fcc Co at higher annealing temperatures. The VC crystallites retain their initial size in the whole temperature range of this study, while grain coarsening takes place in C:Cu and C:Co films above an annealing temperature of 550°C.

5.2.3 Modification of film morphology: TEM investigations

Figure 5.23 (a) and (b) shows the BF cs TEM images of as-deposited and at 500°C postannealed C:Co films. The grains in the as-deposited film exhibit an elongated structure in the direction of the thin film growth which is consistent with the observed globular-elongated growth transition between RT and 300°C as reported in section 5.1.3. Their width is ∼3 nm, while their length is in the range of 5-10 nm. Such a morphology corresponds to zone III of the SZM [78, 81]. The corresponding SAED pattern in figure 5.23 (c) shows an innermost halo from (002) graphite and two broad diffraction rings whose positions can be assigned to the orthorhombic cobalt carbide or the hcp Co phase as discussed in section 5.1. The high-resolution image in the inset of figure 5.23 (a) shows that the carbon matrix exhibits a layered ordering consisting of small fragments typically 1-2 nm in length. The granular morphology is not changed by annealing up to 500°C (figure 5.23 (b)). At this annealing temperature the SAED pattern of figure 5.23 (d) shows the innermost (002) halo of graphite and three

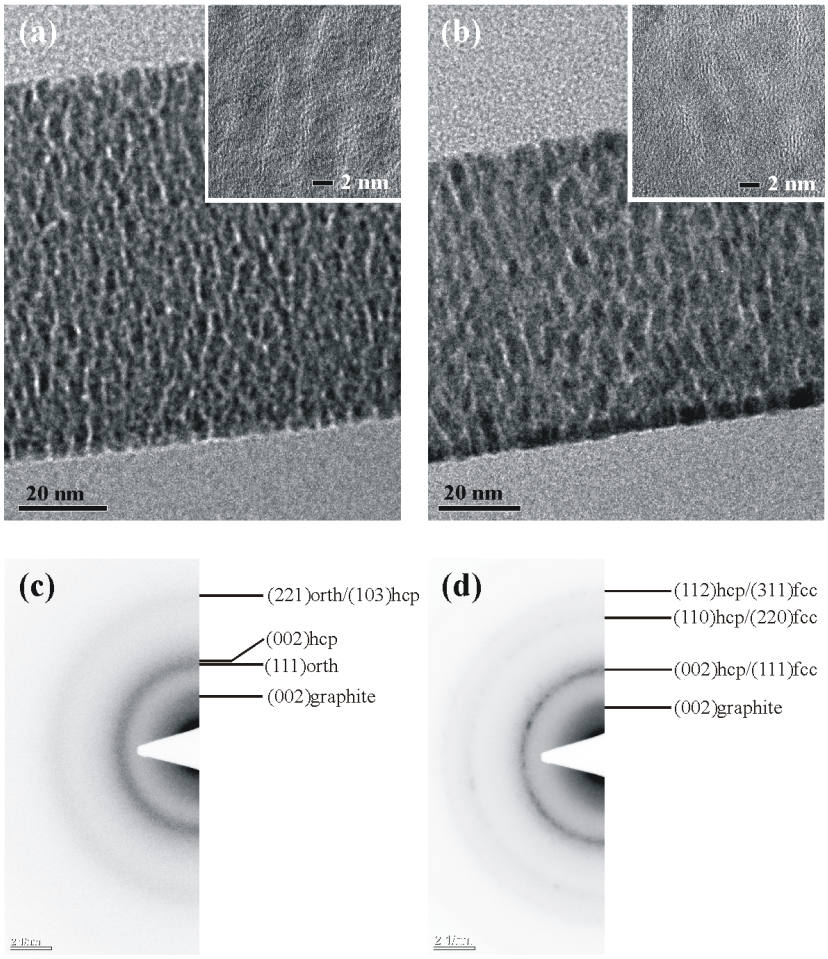

Figure 5.23: Cross-sectional BF TEM images of the C:Co composite thin film as-deposited at 200°C and of the postannealed sample at 500°C (b). The corresponding SAED patterns are shown in (c) and (d). In the diffraction pattern, the rings are indexed with $(hkl)_{orth}$, $(hkl)_{hcp}$ and $(hkl)_{fcc}$ for the orthorhombic carbide, the hexagonal cobalt and the face-centered cubic cobalt phase, respectively.

rings corresponding to $(002)_{hcp}/(111)_{fcc}$, $(110)_{hcp}/(220)_{fcc}$ and $(112)_{hcp}/(311)_{fcc}$. The broadening of the diffraction rings which is caused by the small size of the crystallites does not allow one to distinguish between both metallic phases. However, the pattern is not consistent with the carbide phase indicating the decomposition of cobalt carbide into metallic Co and graphitelike carbon upon annealing. Similar results have been reported in Refs. [22, 33]. The GLC layers which can be seen in the inset of figure 5.23 (b) follow the boundaries of the metal particles in a similar manner as for the as-grown film.

Annealing to 700°C significantly changes the initial film morphology. As can be seen from figure 5.24 (a) Co segregates on the surface. No continuous cobalt layer is formed, but large faceted grains ∼50 nm in height and up to several 100 nm in length are present. The darker regions in the carbon-rich underlayer represent small Co crystallites which remain trapped in the film (figure 5.24 (b)). Besides, bright areas in the carbon-rich underlayer denote diffusion voids while their presence at the film-

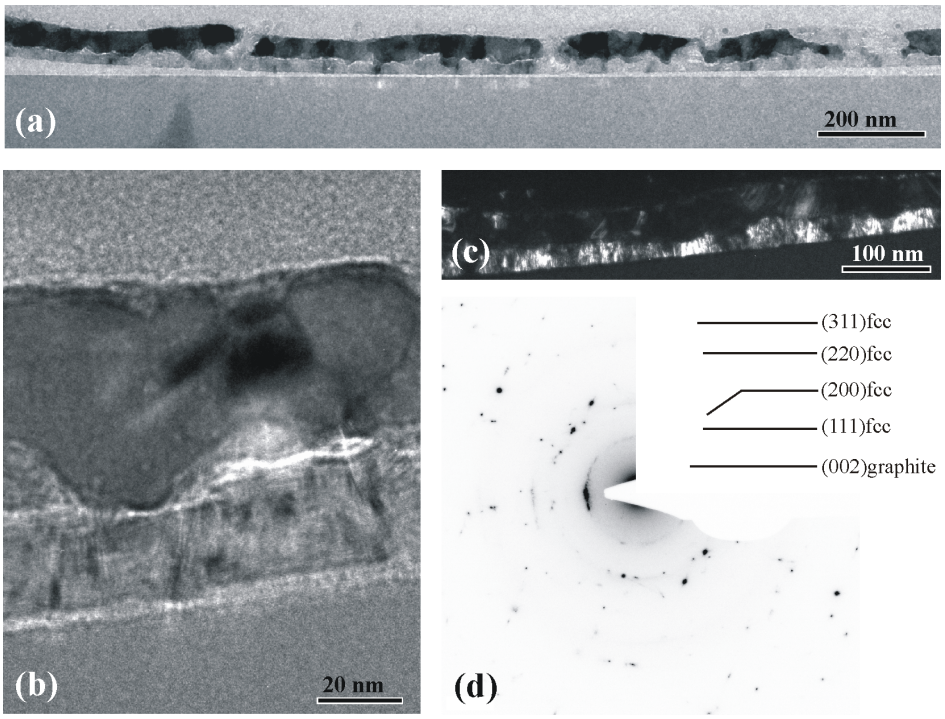

Figure 5.24: Cross-sectional BF ((a) and (b)) and DF (c) TEM images, and corresponding SAED pattern (d) showing a strongly textured graphite (002) diffraction ring for the C:Co film annealed at 700°C. In the diffraction pattern, the rings are indexed with $(hkl)_{fcc}$ for the face-centered cubic cobalt phase.

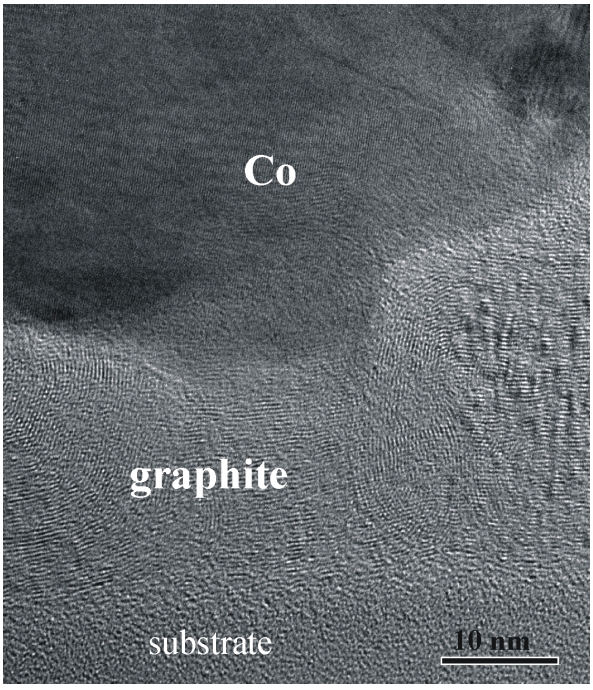

Figure 5.25: Cross-sectional high-resolution BF TEM image of the C:Co film annealed at T_a=700°C showing the graphite layer between a cobalt grain and the substrate.

substrate interface or between the carbon-rich and the Co layer indicates film or layer delamination. Thus, the altering of the film structure by annealing at 700°C causes the decreases of film adhesion [2]. DF TEM imaging (figure 5.24 (c)) shows the presence of Co crystallites in the carbon-rich underlayer more clearly. Besides, the image reveals that the large cobalt grains at the film surface consist of several crystallites. The spotted array in the diffraction pattern of figure 5.24 (d) implies a large size of the Co crystallites, while the inner sharp ring indicates the presence of a new polycrystalline phase. Its d-spacing of 3.4 $\mathring{A}$ corresponds to the graphite (002) spacing, suggesting that the former rather amorphous carbon has transformed to polycrystalline graphite after annealing at 700°C. This diffraction ring shows a strong intensity in the plane-parallel direction indicating that the graphite planes are mainly oriented perpendicular to the substrate surface. The high-resolution BF image of figure 5.25 reveals the presence of large graphene layers between the metal top layer and the substrate. A closer look at the image shows graphite planes perpendicular and parallel to the substrate surface. The presence of perpendicular to the surface oriented graphite planes has also been reported in annealed carbon-cobalt layered thin films [110]. The undulating character of the graphite fringes should be noted.

The BF cs TEM images of the C:Cu film prepared at 200°C, and of subsequently annealed samples at 500 and 700°C are presented in figure 5.26 (a)-(c). Figure 5.26 (a) shows dark grains which are slightly elongated perpendicular to the film surface and are separated by white layers. The shape of the dispersed phase is consistent with the globular-elongated growth transition in C:Cu composites grown between RT and 300°C as reported in section 5.1.3. The grains exhibit a width of 3-5 nm and a length of 6-8 nm. Annealing to 500°C does not change the granular morphology (figure 5.26 (b)). The carbon matrix has an amorphous appearance in the annealed sample (see inset of figure 5.26 (b)) similar to the as-deposited film. The corresponding SAED patterns in figure 5.26 (d) and (e) show sharp rings from the fcc Cu phase and a broad ring at the d-spacing of (002) graphite. Figure 5.26 (c) shows that annealing at 700°C significantly alters the film morphology. Large Cu grains are formed on top of the film. Besides, the facetted shape of the grains suggests that they have formed by liquid-like coalescence. The grains have a height of 70-110 nm and a width in the range of 50-200 nm. The corresponding SAED pattern in figure 5.26 (f) represents a spotted array which indicates about the formation of large Cu crystallites. Furthermore, small Cu grains which were well isolated by the carbon matrix remain in the film. These ones are clearer visible in the corresponding DF image shown in figure 5.27. The inset of figure 5.26 (c) reveals that the carbon phase is amorphous. It should be noted that all diffraction patterns show an innermost ring corresponding to the forbidden (110) reflection of fcc Cu as indicated by the arrow which is assigned to the presence of interstitial carbon atoms in the copper lattice. This ring was also observed in the C:Cu composite grown at 300 and 500°C (see section 5.1.3).

The cross-sectional bright-field TEM images of as-deposited and at 700°C postannealed C:V composite thin films are shown in figure 5.28 (a) and (c). No changes in the granular morphology are observed by annealing up to this temperature. The films are composed of globular and in the film growth direction slightly elongated grains

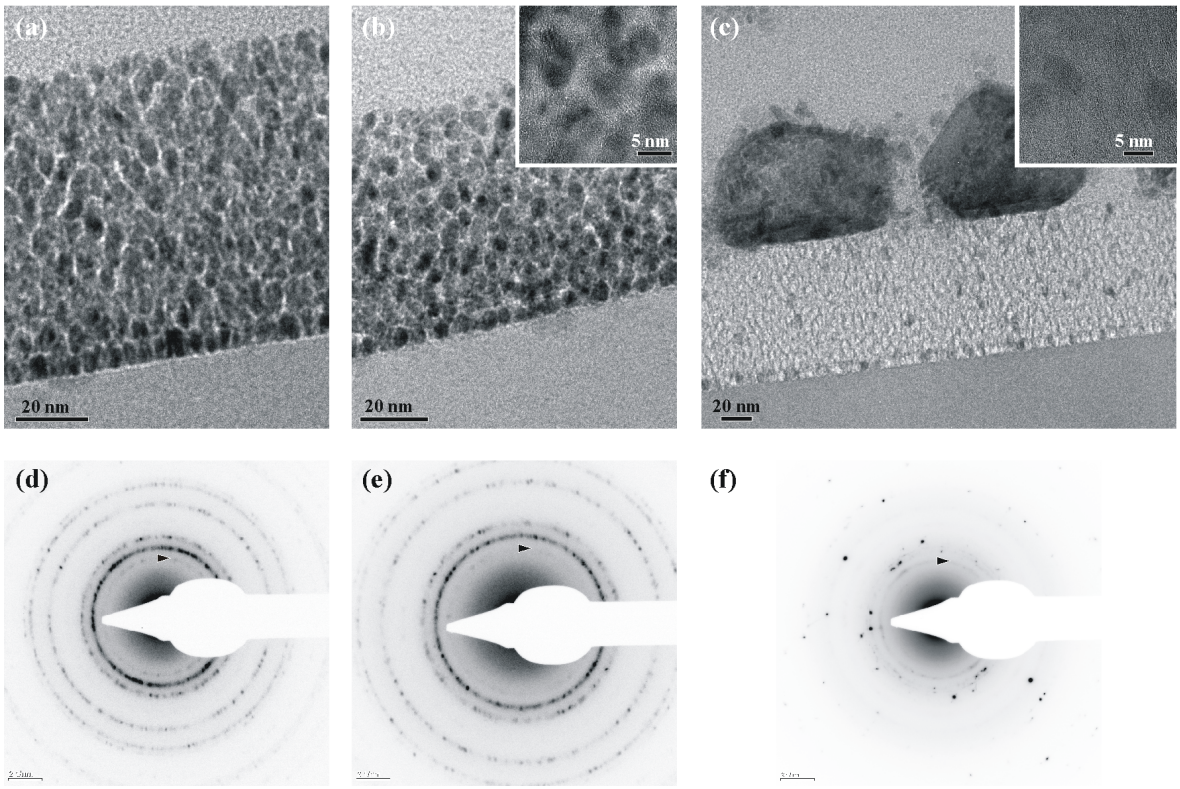

Figure 5.26: Cross-sectional BF TEM images of the C:Cu composite thin film as-deposited at 200°C and of annealed samples at T_a=500 (b) and 700°C (c). The corresponding SAED patterns are shown in (d)-(f). The arrow in the SAED patterns indicate the forbidden (110) reflection of the fcc Cu phase.

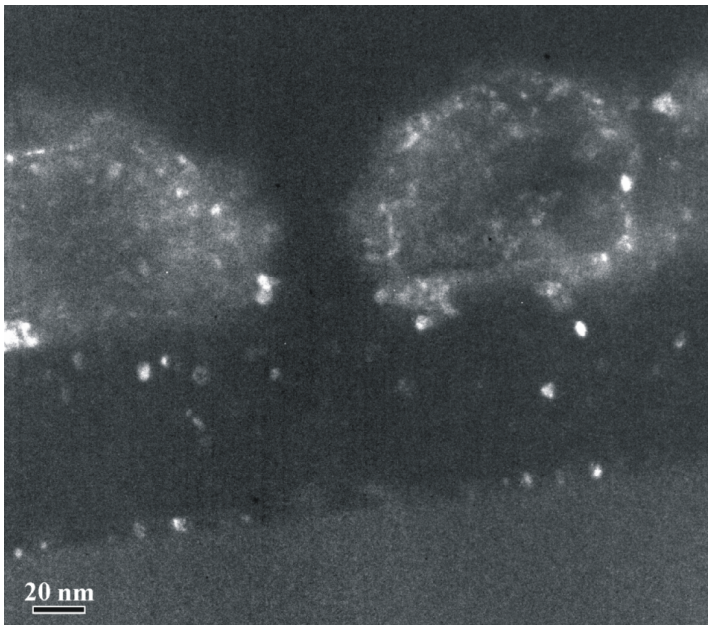

Figure 5.27: Cross-sectional DF TEM image of the C:Cu composite film annealed at T_a=700°C.

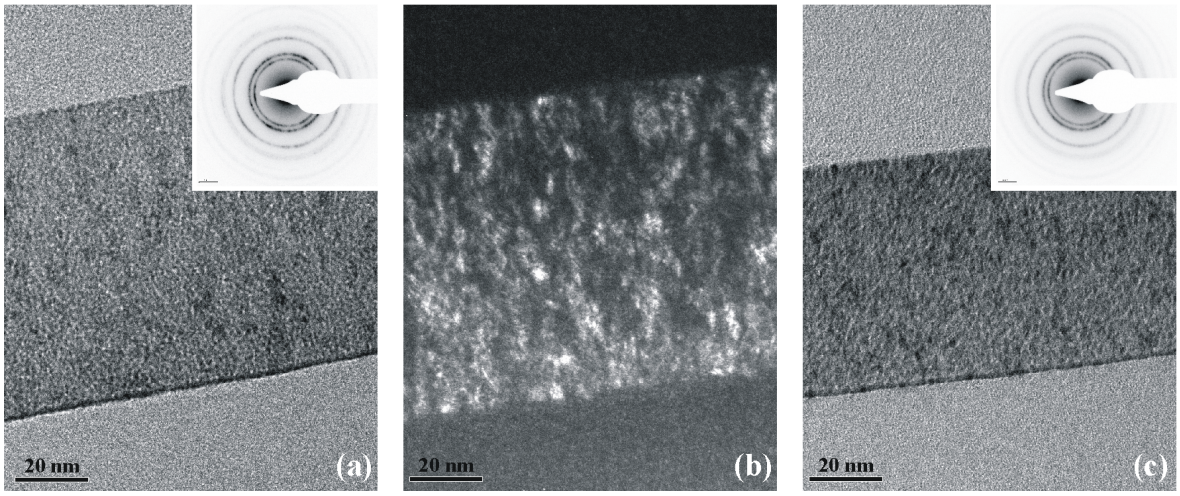

Figure 5.28: Cross-sectional BF (a) and DF (b) TEM images of the C:V composite thin film as-deposited at 200°C and cross-sectional BF TEM image of the annealed sample at T_a=700°C. The corresponding SAED patterns are shown in the insets.

which are clearer visible in the corresponding dark-field image (figure 5.28 (b)). The difference in granular morphology in comparison to the C:V films presented in section 5.1.3 is related with the higher V content of the films in the annealing series. The matrix (white layers) is hardly visible in the BF TEM images due to the small distance between neighboring grains resulting in a low contrast between matrix and dispered phase. This also complicates a precise determination of the particle dimensions. Roughly, the grains are 2-3 nm in width and up to 6 nm long. The surrounding carbon phase seems to have a featureless appearance. The corresponding SAED patterns of the as-deposited and annealed sample are similar showing sharp rings due to the fcc VC phase and an innermost broad ring at the graphite (002) position. The similarity of the patterns confirms the above observation that the initial granular morphology is retained.

The grain size obtained from the width of diffraction peaks employing the Scherrer equation is in good agreement with the size indicated by the high-resolution TEM images for the as-deposited and annealed C:V composite films. In contrast, for C:Co and C:Cu films annealed at 700°C the estimated grain size by the Scherrer formalism is significantly lower than the one obtained from the TEM micrographs indicating that the grains are composed of several crystallites as shown by DF TEM imaging.

Finally, SAED analysis confirms the presence of fcc VC and fcc Cu observed by XRD in C:V and C:Cu composites up to an annealing temperature of 700°C. In the C:Co composites the metastable cobalt carbide decomposes below 500°C into metallic Co and graphite-like carbon. TEM investigations show no changes in the granular morphology of C:Co and C:Cu composites by annealing up to 500°C. No composite structure is present in these films after annealing at 700°C because metal surface segregation results in a vertical phase separation. The different shape of the large Co and Cu grains on the surface of the carbon layer indicates that C/Co interface energy is lower than that of C/Cu. Polycrystalline graphite is formed in C:Co composites during annealing, while

the carbon matrix retains its amorphous appearance in C:Cu composites. No changes upon annealing up to 700°C are observed in C:V films.

5.2.4 Carbon matrix: Raman spectroscopic investigations

Figure 5.29 shows the normalized first-order and second-order Raman spectra of as-deposited and annealed C reference and C:TM composite films. The first-order Raman spectra of the annealing series of pure carbon films (figure 5.29 (a)) exhibit two broad overlapping features typical for amorphous carbon films, namely the D peak and the G peak. Besides, the peak at ∼950 cm^{-1} from underlying silicon is visible. No remarkable changes are observed up to 500°C, while at higher temperatures annealing leads to a slight increase in the relative D peak intensity and a slight shift of the G peak to higher wavenumbers. The Raman spectra shows a broad feature in the second-order region.

The first and second-order Raman spectra of the annealing series of C:Co composites is shown in figure 5.29 (b). The relative D peak intensity of the as-deposited C:Co film is higher than for the pure carbon film which is consistent with the observations on C and C:TM films grown at low temperatures as reported in section 5.1.4 and indicates about a larger size of sixfold ring clusters for the latter. Two broad overlapping features are observed up to 500°C while at higher temperatures the separation of D and G peaks becomes more pronounced. The blue shift of the G peak upon annealing should be noted. In addition, second order peaks appear at 650°C which are most pronounced at the highest annealing temperature of this study. The appearance of the second-order peaks is accompanied by a decrease in the relative D peak intensity. The dominant feature in the second-order spectrum is an intense line at 2700 cm^{-1}, denoted by D*. Two weak features around 2950 cm^{-1} and at ∼3240 cm^{-1}, which are labeled D+D' and G*, respectively, are also observed. The D* mode is the second order peak (overtone) of the D peak, its position is very close to twice the D mode frequency. The G* peak is an overtone of the disorder-induced D' line [56, 137] present at ∼1620 cm^{-1} in nanocrystalline graphite (figure 5.14), which is right above the G line. The feature around 2950 cm^{-1} arises from the combination of D and D' line. The identification of these peaks in the second-order Raman spectra can additionally be made by using the vibrational density of states of a single graphite layer [140]. The main peaks in the VDOS occur at 1620, 1360, 850, 830 and 570 cm^{-1}. Thus 2(1620) cm^{-1} = 3240 cm^{-1} and 2(1360) cm^{-1} = 2720 cm^{-1} correspond to G* and D*. The disorder-induced peak at ∼2950 cm^{-1} roughly corresponds to (1360 + 1620) cm^{-1} = 2980 cm^{-1}. The Raman spectra at 700°C resembles those of nanocrystalline graphite, see figure 5.14.

The Raman spectra of as-deposited and annealed C:Cu films are shown in figure 5.29 (c). The D-G band is clearly observed up to an annealing temperature of 400°C. The broad background is attributed to photoluminescence which contributes to the Raman spectra. Above 400°C, the Raman spectra are dominated by photoluminescence. The luminescence background was subtracted from the Raman spectra up to 400°C, see inset of figure 5.29 (c). For higher annealing temperatures it is not possible to sub-

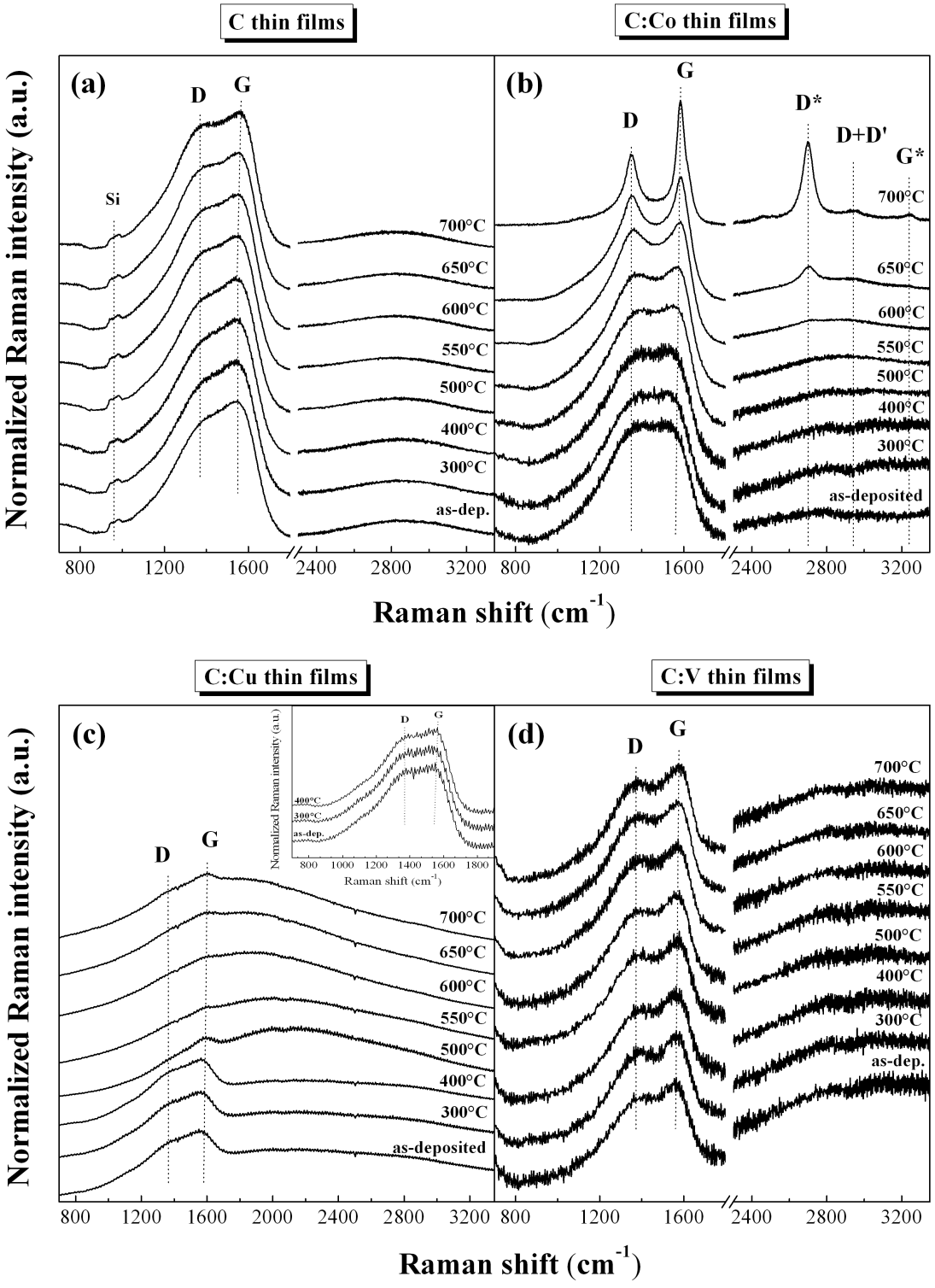

Figure 5.29: Normalized Raman spectra of C (a), C:Co (b), C:Cu (c), and C:V (d) films as-deposited at 200°C and after annealing at 300-700°C measured with 532 nm excitation light. The features in the second order Raman spectra are indicated by D*, D+D' and G*. Normalized Raman spectra of C:Cu films after subtraction of the photoluminescence background are shown in the inset. The spectra were vertically shifted, but the original intensity ratios for each measured series are preserved.

tract the luminescence background. The inset shows the increase in G peak position concomitantly with temperature. No peaks in the second-order Raman spectra can be identified, while two small broad peaks in the region of the D-G band which overlaps the photoluminescence background indicates about the presence of disordered carbon structures.

The Raman spectra of as-deposited and postannealed C:V films are shown in figure 5.29 (d). No remarkable changes upon annealing are observed in the composite films, except the slight increase in G peak position. The Raman spectra show no second-order peaks.

The results from peak fitting of the Raman spectra of as-deposited and postannealed C, C:Co and C:V films are summarized in figure 5.30. The results from the C:Cu films are excluded from the figure because the fitted temperature range (200-400°C) is too narrow to observe reasonable tendencies and to draw conclusions out of them. For the sake off completeness, all fitting parameters (D and G peak position and width, coupling coefficient q, coupling parameter Γ_G/q, I_D/I_G ratio and the calculated cluster size L_a) are summarized in appendix 7.2 for the as-deposited and annealed C and C:TM (TM=V, Co, Cu) films.

The evolution of the G peak position is shown in figure 5.30 (a). For pure carbon films the G peak is positioned at 1555 cm^{-1} in the as-deposited film and remains almost constant up to 500°C (1557 cm^{-1}), while it slightly increases at higher temperatures to 1563 cm^{-1} at 700°C. Annealing of C:V films leads to a slight increase from 1562 cm^{-1}(as-deposited) to 1575 cm^{-1} (700°C). The G peak position dependence on temperature is more pronounced for C:Co films, increasing concomitantly with the annealing temperature from 1545 cm^{-1} for the as-deposited film to 1588 cm^{-1} at 700°C. At T>600°C the G peak position is close to that of nanocrystalline graphite.

The behavior of G and D peak width and of the coupling parameter Γ_G/q vs. annealing temperature are illustrated in figure 5.30 (b)-(d). For C:V films no considerable changes with temperature are observed. Annealing of C and C:Co films up to 500°C has no remarkable effect on the width of D and G peak and Γ_G/q. Besides, the parameters of both types of films are close to each other. At higher annealing temperatures these parameters start to decrease, except for Γ_D in the pure carbon films. The decrease is more pronounced for C:Co films. At the highest annealing temperature the coupling coefficient is close to zero indicating that in-plane graphene ordering is complete and three-dimensional ordering begins [140, 145].

For the amorphous carbon films, annealing has no influence on the I_D/I_G ratio up to 500°C. At higher annealing temperatures the ratio increases from 0.71 at 500°C to 0.84 at 700°C. The as-deposited C:TM films show a higher I_D/I_G ratio in comparison to C films indicating a larger size of the sixfold ring clusters (see section 5.1.4 for details). Besides, annealing of C:TM films has the opposite effect as for C films: it decreases I_D/I_G. Up to 600°C, C:Co and C:V films show no significant changes while I_D/I_G starts to decrease significantly for higher temperatures for C:Co films and falls from 0.92 at

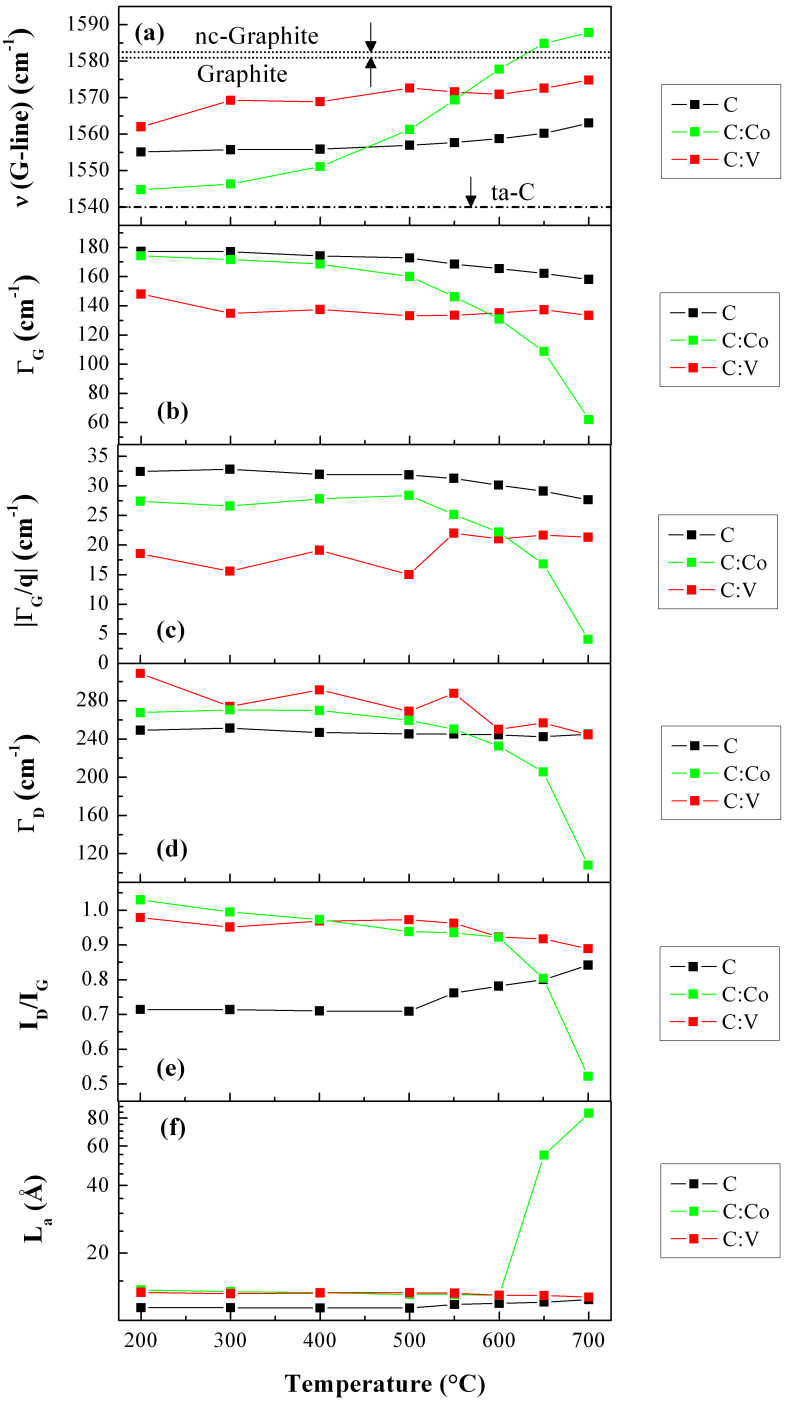

Figure 5.30: Position (a), width Γ_G (b) and coupling parameter Γ_G/q (c) of the G peak, width Γ_D of the D peak (d), I_D/I_G ratio (e) and cluster diameter L_a (f) of C, C:V and C:Co films as-deposited at 200°C and after annealing at 300-700°C for 532 nm excitation light. The corresponding G peak positions of nc-graphite, graphite and ta-C are additionally shown as horizontal lines for comparative purpose.

600°C to 0.52 at 700°C.

The evolution of the sixfold ring cluster size can be followed by plotting the cluster size L_a vs. annealing temperature. The question arises if equation 4.3 or 4.4 should be used to estimate L_a. The decision is based on the following arguments: The Raman spectra of all films show broad D and G peaks, except C:Co films annealed at 650 and 700°C, which indicates that they correspond to stage 2 of the amorphization trajectory [42, 56, 138]. Besides, the as-deposited films have already been assigned to stage 2 (see section 5.1.4). Furthermore, for a-C films annealing leads to an increase in G peak position and I_D/I_G ratio which indicates ordering in agreement with the predictions of stage 2. Thus equation 4.4 has to be used to estimate L_a. In contrast, for the C:Co films annealed above 600°C, the appearance of second order peaks indicates about a long-range ordering of the carbon phase, i.e. a larger size of the graphene-like sp^2 bonded clusters, while I_D/I_G significantly decreases. Thus, the TK relation (equation 4.3) is valid for these two films. The cluster diameter L_a as a function of annealing temperature is shown in figure 5.30 (f) for C, C:V and C:Co films. In a-C films the cluster size remains constant up to an annealing temperature of 500°C (L_a=11.4 $\mathring{A}$) and increases only slightly for higher annealing temperatures up to 12.4 $\mathring{A}$ at 700°C. In C:V films the cluster size remains almost constant of ∼13 $\mathring{A}$ upon annealing. For C:Co films annealing has only little effect on the cluster size up to 600°C (L_a ≈13 $\mathring{A}$), while L_a drastically increases at higher annealing temperatures up to ∼84 $\mathring{A}$ at 700°C.

5.2.5 Discussion

The results above obtained from the annealed samples demonstrate that the changes in the film morphology depend on the annealing temperature, and the transition metal presence and type. The first part of the discussion considers the modification of the dispersed phase while the second part discusses the structural modification of the carbon bonding structure by annealing for the three different transition metals. In the third part, the results on the annealed C:TM films are summarized in a model, and the results are discussed on the basis of the mutual C-TM chemical affinity and temperature activated bulk diffusion.

Modification of the dispersed phase

For the C:Co films, annealing in the temperature range of 300-500°C leads to the decomposition of the metastable cobalt carbide phase into the more stable hcp Co phase indicated by the phase diagram and graphite-like carbon. Such transformation proceeds with release of energy [2] as the thermodynamically phases are C and Co. Besides, no changes in the granular morphology are observed up to an annealing temperature of 500°C in comparison to the as-grown film. Thus, the carbidic-metallic transformation should be related with interstitial carbon bulk diffusion out of the cobalt carbide grains where it stops at the interfaces because carbon diffusion in carbon is very low as the

annealing series of carbon reference films shows. Above 500°C, the hcp Co nanoparticles are further transformed into the fcc Co nanoparticles. At annealing temperatures above 550°C bulk diffusion of the metal occurs which results in the increase in size of the Co crystallites as observed by XRD. The vertical phase separation and the formation of an almost continues metal layer on the surface at an annealing temperature of 700°C most probably should be assigned to the tendency of the system to minimize the free energy by reducing the amount of matrix-inclusion interfaces. Furthermore, the higher affinity of the carbon to silica (2D layer-by-layer growth mode) than that of metal (3D island growth) is the most probable reason of such a depth distribution (metal/carbon/silica). The faceted shape of the grains is a hint that the coalescence of contacting metallic islands occurs and proceeds via liquid-like coalescence mechanism.

Similar to C:Co films, in the annealed C:Cu films metal bulk diffusion above 550°C results in significant grain coarsening and the metal surface segregation. It should be noted that for the C:Cu film annealed at 500°C even though TEM shows no remarkable changes in the film morphology, ERDA indicates about a slightly higher Cu content on the surface which is a hint for the lower activation energy for bulk diffusion of Cu in comparison to Co, probably due to the lower melting point of the former as indicated by the phase diagram. In contrast to cobalt which forms a quasi-continuous metal layer at 700°C, the presence of large faceted grains on the surface for the postannealed C:Cu film shows that Co wets better carbon than Cu which is assigned to the lower affinity to carbon for the latter. This indicates that surface energy is lower than C/Cu interface energy for the C:Cu system in contrast to the C:Co system.

No changes in the morphology of the dispersed phase are observed for the C:V films upon annealing up to 700°C, the maximum temperature of the present study. This is associated with the strong V-C interaction which ensures the thermal stability of the VC phase up to 2670°C [35] and thus of the whole composite structure of the films in the investigated temperature range. Following this, neither carbon nor vanadium diffusion occurs in the studied temperature range.

The present results show that the thermal stability of the composite decreases in the order C:V > C:Co > C:Cu, i.e. is proportional to the TM affinity to carbon. In addition, the film changes upon heating start with the carbon interstitial out-diffusion from the Co carbide grains where it stops at the interfaces because carbon diffusion in carbon is very low as the annealing series of carbon reference films shows. This step is followed by thermally activated Co diffusion at higher temperatures. Such a two step process does not occur neither in C:Cu films as a carbidic phase does not form in this system nor in C:V films as the strong C-V bonds impose a high activation energy for such a diffusion.

Modification of the carbon bonding structure

The Raman spectra of the annealing series of carbon reference films show no remarkable changes in the investigated temperature range of this study indicating that bulk

diffusion of C atoms in the carbon matrix is strongly limited. Slight variations are observed in the Raman spectra fitting parameters (slight increase in G peak position and I_D/I_G ratio, slight decrease in G peak width and coupling parameter) above an annealing temperature of 500°C suggesting a low ordering of the carbon phase due to bulk diffusion. It should be noted that the graphitization of amorphous carbon often involves temperatures in the range of 1700-3000°C [36] which is well above the maximum temperature of the present study.

For the postannealed C:Co films even though the granular morphology is not changed by annealing up to 500°C and HRTEM also shows no considerable changes in the layer-like structure of the carbon matrix, Raman spectroscopy indicates ordering within the graphitic (sixfold ring) clusters as the G peak position increases (figure 5.30 (a)) according to the stage 2 of the *amorphization trajectory* (amorphous carbon → nanocrystalline graphite) [135, 138]. This most probably should be related with the decomposition of cobalt carbide into hcp Co and graphite like carbon, and carbon phase rearrangement at the interfaces. Above 550°C, when bulk diffusion of Co occurs, the ordering effect with increasing temperature becomes more pronounced (increase in G peak position, significant decrease in Γ_G, Γ_G/q and Γ_D). Besides, the appearance of second-order peaks in C:Co films annealed above 600°C indicates long-range ordering of the carbon phase and a significant larger size of carbon graphitic structures in comparison to lower annealing temperatures and when compared to C reference films. At 700°C, the structure resembles nanocrystalline graphite, indicating about a finite size of the crystallites and the absence of amorphous sp^2 and sp^3 carbon [56]. Similar results have been reported by annealing carbon/cobalt layered thin films up to 600°C [110]. In addition, the convex curvature in the G peak behavior of C:Co films above 600°C in figure 5.30 (a) hints toward a further decrease of the G peak position at higher annealing temperatures which is in agreement with the stage 3 of the amorphization trajectory when passing from nanocrystalline graphite to graphite.

The high-resolution TEM image for the C:Co composite annealed at 700°C shows that the graphite basal planes are not rigid but exhibit an undulating character and are bent. Therefore, the produced phase is not crystalline graphite, which would have a regular translational symmetry of the carbon atoms within the basal planes, but is best described as graphitized carbon, rather than graphite itself. The Raman spectra of the annealed C:Co film at 700°C is consistent with the nanocrystalline graphite structure observed by HRTEM. The graphitic structures in the annealed C:Co composite film are similar to the observations in annealed a-C/TM/a-C trilayer films employing a number of first row transition metals (Cr, Fe, Co, Ni) [110, 186]. The graphitization of amorphous carbon upon annealing of such sandwich structures occurs well below 800°C and is brought about by the elements themselves in the case of Co or Ni, and by metastable carbide phases - iron carbide and chromium carbide. In situ TEM observations revealed that upon annealing the metal or carbide (formed by the diffusion of C into the metal) layer splits and is ejected from the original layer, and that these metal-rich grains migrate through a-C, leaving the graphite phase in their wake. The observed catalytic graphitization of a-C in metal/carbon layered films shows a striking similarity to the behavior of other group IV amorphous elements Si and Ge, which

crystallize at unusually low temperatures well below the reaction temperature in the pure elemental phase (500-700°C [110, 186]) when they are in contact with metals, in particular those with which they form eutectic phase diagrams [186], i.e. limited solid solubility of the terminal phases. It should be stated here that cobalt also forms an eutectic system with carbon [72]. The graphite formation is termed metal-mediated crystallization (MMC) or, in the case of carbides, carbide-mediated crystallization, and is based on a dissolution-diffusion-precipitation mechanism [10, 110, 186]. The proposed model is that carbon atoms dissolve into the metal, thus supersaturating it with respect to the more stable crystalline phase due to the higher free energy of the amorphous state, followed by the diffusion of carbon through the metal and the precipitation on the surface as graphite. The diffusion through the metal lattice is more rapid than the direct rearrangement of the atoms in the amorphous network, i.e. this mechanism provides the shortest reaction path to release the excess free energy of the amorphous phase [186]. This is consistent with the present findings which show that carbon interstitial diffusion occurs at the temperatures far below 500°C. Presumably, the same mechanism as in the a-C/Co/a-C trilayer system occurs in the C:Co composite upon annealing, with the exception that no metal layer splits into individual particles. Carbon atoms are transported through the Co phase from the a-C/Co to the Co/graphite interface, thus pushing the particles forward to the surface leaving graphitic phase behind. On their way larger Co crystallites might be formed by coalescence of contacting particles. Even though the equilibrium solubility of C in Co is small, about 0.2 at.% at 700°C [72], the higher free energy of a-C compared to the crystalline form presumably extends the solubility limit of C in Co, thus supersaturating the a-C/Co interface with carbon and giving rise to a concentration gradient of C inside the Co grains. The estimated solubility of C in a splat-quenched Co-C solution is about 5.3 at.% [110]. Such a concentration gradient is the driving force for the C diffusion through the metal. The graphitization of a-C is mediated directly by the Co phase, because cobalt carbide decomposes prior to the reaction (<500°C). Such a mechanism requires a transport of entire metal particles, as carbon diffusion in carbon phase was shown to be negligible and static Co particles would result in a complete metallic particle encapsulation with a graphitic carbon in the immediate interface vicinity. Such a mobility of metal nanoparticles is not surprising. It has been demonstrated in the literature [187] by means of environmental TEM that during the carbon nanotube growth metal catalyst nanoparticles in contact with the surrounding carbon behave like liquid-like entities in terms of mobility and shape changing while remaining crystalline.

Konno and Sinclair observed by differential scanning calorimetry (DSC) on annealed a-C/Co/a-C trilayer thin films of variable Co layer thickness that a thicker metal layer induces the graphitization more rapidly and at slightly lower temperatures [110]. DSC scans showed a peak temperature of the exothermic reactions at 570, 590, and 610°C for a Co layer thickness of 21, 14, and 7 nm. This is consistent with the observations in annealed C:Co composite films, which show a lower degree of separation of the D-G band upon annealing for the films with the lower Co content [6, 9], i.e. a smaller size of the Co particles which take part in the reaction. The relatively small grain size in the C:Co composite films of the present study might explain the higher graphitization temperature in comparison to layered carbon-cobalt structures. These observations

support the conclusion that the growth rate of carbon graphitic structures is directly proportional to the flux of carbon atoms across the metal and metal nanoparticle movement through the carbon matrix.

At 700°C, the size of graphite crystallites L_a estimated from the I_D/I_G ratio obtained by fitting the Raman spectra is about 8 nm, while HRTEM shows continuous undulating fringes over longer distances. The discrepancy between the effective grain size L_a obtained by Raman and that of TEM imaging has also been reported elsewhere in the literature. Konno and Sinclair [110] pointed out that a strict definition of the size of graphite crystallites is quite difficult and raised the question how much deviation from a rigid basal plane should be sufficient to constitute the termination of a grain. They assumed that L_a is a measure of the correlation of graphite planes which does not necessarily correspond to the physical size of graphite in the presence of undulating planes. On the other hand a lower L_a value for Raman can be assigned to defects within the layers which reduces the effective graphitic cluster size [20]. From this picture, the L_a value corresponds to an average distance between defects.

At some locations the basal planes of the graphite tend to follow the contours of the metal particles from which they emerge. However, the observed graphite (002) texture with the planes mainly perpendicular to the surface most probably should be related with the conversion mechanism of a-C to graphite in the presence of small metal particles, because for annealed a-C/TM/a-C trilayer films the graphitic planes are roughly parallel to the original a-C/TM interface and the substrate surface [110, 186].

No second-order Raman signals are observed for the postannealed C:Cu films and the carbon first order spectrum, if visible, shows a broad feature in the D-G band region, which is in good agreement with the featureless appearance of the carbon matrix in these films and indicates that the majority of the sp^2 phase is probably present in small, distorted aromatic clusters. The Raman spectra of the annealed C:Cu films are dominated by carbon luminescence from 500°C on, most probably due to the metal surface segregation or the formation of larger Cu crystallites. Copper does not bring about the graphitization by annealing up to 700°C, which is assigned to the very low solubility of carbon in copper being 0.006 at.% at 700°C [35]. Thus, a metal-mediated graphitization process similar to Co can not take place. This behavior is consistent with the observation on copper/carbon layers which show no graphite formation by annealing up to 600°C [186]. On the other hand, it has been shown in the present work that co-sputtering of carbon and copper at T≥300°C produces copper particles encapsulated by graphite-like carbon. Thus, it can be concluded that in the surface diffusion dominated regime Cu promotes six-fold ring formation and clustering, but in the bulk diffusion regime does not act as a catalyst.

The annealed C:V films do not show the presence of layered structures in the carbon phase and also Raman spectroscopy shows no remarkable changes by annealing up to 700°C which indicates that the initial bonding structure of the carbon matrix consisting mainly of small aromatic clusters is preserved. Presumably, the diffusion of C is too slow in VC, a high melting temperature compound, to bring about the graphitization process

by a carbide-mediated mechanism similar to the system Fe-C and Cr-C [186]. It should be noted that no graphitization has been achieved by annealing Ti/C layered structures up to 1000°C, while only the extremely stable TiC phase was produced at 400°C [186]. As carbon atomic diffusion in the respective material is inversely proportional to its melting point, a much higher temperature is required for the graphitization of the carbon phase. Using known diffusion data for TiC a temperature of ∼1500°C was estimated to obtain equivalent changes to those in the Ni-C or Co-C system [186]. As VC exhibits a slightly lower melting temperature than TiC the graphitization in C:V composites is expected to occur at somewhat lower temperatures. However, such high temperatures are still beyond the scope of the present work.

The above observations suggest that the carbon graphitization upon annealing is determined in addition to the annealing temperature by the solubility of carbon in the metal, the diffusion speed of carbon in the particles, i.e. by the melting temperature of the dispersed phase, and the mobility of metal nanoparticles through the carbon matrix themselves. In the surface diffusion dominated regime during growth all the metals enhance the sixfold ring clustering, but in the bulk diffusion controlled regime only Co acts as a catalyst for the carbon graphitization as for C:V much higher temperatures are needed, while for C:Cu carbon is practically immiscible with Cu.

Structure zone diagram of annealed C:TM films

Figure 5.31 summarizes the modification of the C:TM composite structure upon annealing. The as-deposited films are composed of metallic/carbidic NPs embedded in amorphous/GLC matrix. For C:V films, no considerable changes neither of the dispersed phase nor of the matrix are observed up to the highest annealing temperature of the study of 700°C. For C:Co films, annealing in the T range of 300-500°C results in the carbon interstitial diffusion out of Co rich nanoparticles, i.e. in the formation of metallic NPs by the decomposition of metastable Co carbide without considerable changes of the granular morphology. Further increase of the annealing temperature to 550°C activates the metal bulk diffusion leading to significant grain coarsening and Co surface segregation. Similar surface segregation effect is observed in C:Cu films in a similar temperature range. This behavior is attributed to the minimization of the systems free energy by reducing the amount of interfaces. While the metal surface segregation is accompanied by carbon graphitization via the dissolution-diffusion-precipitation mechanism in C:Co films, the matrix in the C:Cu films retains its featureless appearance.

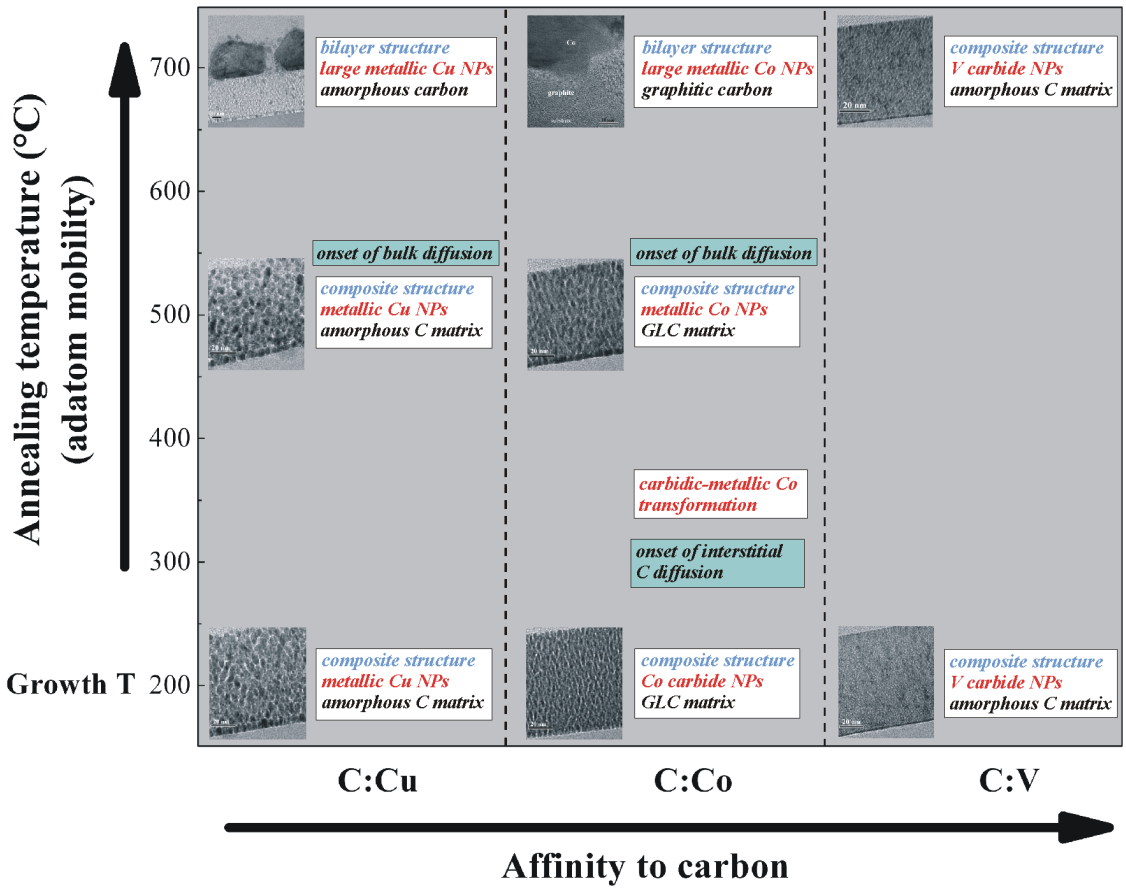

Figure 5.31: Structure zone diagram of C:TM films as a function of the mutual C-TM chemical affinity and annealing temperature. NPs denotes nanoparticles.

6 Conclusion

The structural evolution of carbon:transition metal films has been investigated in two regimes: (i) surface diffusion governed regime occurring during the film growth and (ii) bulk diffusion dominated regime occurring during the post-deposition thermal annealing. Vanadium, cobalt and copper were incorporated into the carbon matrix by co-deposition during ion beam sputtering. These elements exhibit different chemical affinity to carbon which manifests itself by three types of phase diagrams: intermediate compound (V-C), eutectic (Co-C), and peritectic (Cu-C). The influence of the metal type, metal content (15-40 at.%), substrate temperature (RT-500°C), and annealing temperature (300-700°C) on the structure and morphology of the composite has been studied by the means of ERDA, XRD, TEM and Raman spectroscopy. The combination of these analytical techniques has allowed the characterization of the dispersed phase *as well as* the carbon matrix.

The results demonstrate that for the films grown on thermally oxidized Si substrates, the thermodynamic equilibrium structure for Co-C and Cu-C systems consists of a metallic layer on the top of a carbon layer. This reflects the system's tendency to minimize the amount of interfaces. Higher affinity of the carbon to silica (2D layer-by-layer growth mode) than that of metal (3D island growth) is the most probable reason of such a depth distribution (metal/carbon/silica). Different wetting of the top layer of Co-C system consisting of quasi-continuous layer in relation to that of Cu-C consisting of faceted nanoparticles reflects the fact that the TM-C interface energy is lower for the Co-C system. It should be noted that different substrate types with different wetting behavior of carbon and metals might cause different depth distribution in the thermodynamic equilibrium. For C:V nanocomposite films, the thermal activation provided during the annealing in the temperature range addressed in this study (300-700°C) has not been sufficient to induce any considerable changes, and thus no conclusions can be drawn on the thermodynamic morphological configuration of this system. On the other hand, it reflects that the strong chemical C-V affinity stabilizes not only the VC dispersed phase, but also the embedding carbon matrix. As the pure carbon shows a weak tendency for local temperature induced reordering, this stability effect in C:V nanocomposite thin films is unambiguously attributed to the presence of a stable dispersed phase.

While the thermodynamic forces drive the system into the above structure, the low film growth temperature, and thus absence of bulk diffusion, imposes strong kinetic constraints which govern the structure formation in the surface diffusion dominated regime. Concerning the phase structure, low growth temperatures lead to the formation

of metastable cobalt carbide. The increase in surface diffusivity with temperature results in a carbidic → metallic Co phase transformation above 300°C. In contrast, vanadium (copper) is in carbidic (metallic) state in the whole temperature range of the study. This demonstrates that the moderate mutual dispersed phase-matrix affinities can result in a formation of metastable phases provided that the diffusion activation energy (temperature induced mobility) on the dispersed phase surfaces is sufficiently high (low).

The different compound forming tendency shows up through differences in surface diffusivity. As larger mobility results in larger dispersed nanoparticles for a given substrate temperature, TM content and growth rate, the present results show that the surface diffusivity decreases in the order Cu > Co > V. This indicates that the metal adatom mobility is inversely proportional to their affinity to carbon determining the strength of the TM-C interactions.

The film growth occurs as a competition of the dispersed phase to grow in size and the encapsulating tendency of the matrix. Similarly to the single phase films, the average nanoparticle diameter grows with the growth temperature. In contrast to single phase metallic films where the increase in growth rate at the initial growth stages results in higher nucleation density and thus fine structure formation, for C:TM nanocomposite films the increase in metal content during co-deposition (and thus of the effective growth rate of the metal rich phase) results in nanoparticle coarsening. This is consistent with the thermodynamic tendency of the system to minimize the free energy by minimizing the amount of matrix-inclusion interfaces. It is also consistent with a kinetic picture of metallic islands serving as sinks for metal adatoms whose mobility is dependent on the temperature, growth rate and state of the carbon matrix, where an increase in the metal content and the growth temperature increases the probability of the adatom trapping or nanoparticle coalescence (static or dynamic).

Low adatom surface diffusivity causes the repeated nucleation dominated growth regime with fine-grained structure of globular nanoparticles. This occurs at low growth temperatures for C:Co and C:Cu films and in the whole growth temperature range for C:V films. The present results do not allow revealing the exact cause of the repeated nucleation events. Most probably in this regime both the metal mobility on the carbon phase as well as the carbon atom diffusivity across the metal/carbon interface are responsible for this effect. The average diffusion length, which is determined by the ratio of surface diffusivity and growth rate, is low and prevents the metal adatoms to reach the existing nanoparticles before being covered. Amorphous carbon can easily trap the metal adatoms which further promotes the repeated nucleation. Defects in the carbon phase or surface steps act as effective nucleation centers, while the influence of contamination also cannot be excluded. On the other hand, though the carbon diffusivity on the metal nanoparticle surface is expected to be high, the situation can change drastically when a carbon adatom reaches a carbon/metal interface and starts to interact with carbon matrix atoms. This study clearly shows that carbon mobility on the carbon matrix is low owing to the strong covalent C-C interactions. Such interactions can drastically increase the energy barrier at the interfaces stopping the carbon atoms

and causing the nanoparticle closure and, consequently, repeated nucleation events.

The increase in the surface diffusivity promotes the lateral phase separation resulting in an elongation of the nanoparticles in the growth direction for C:Co and C:Cu nanocomposites. Even copper diffusivity is significantly larger than that of cobalt which results in the dispersed nanoparticles with significantly larger diameters in C:Cu films, the morphological transition globular→elongated occurs in the same temperature range for both types of films. This results demonstrate that indeed not the metal diffusivity on the carbon phase is the morphology governing factor, but the energy barrier for carbon adatoms at the metal/carbon interfaces. The interface crossing becomes effective somewhere in the temperature range of RT-300°C. This does not occur for C:V films, which most probably indicates that in these films both metal and carbon diffusion barriers are too high as to allow for any significant surface diffusivity in the temperature range of RT-500°C addressed in this study.

Despite of the morphological transition globular→elongated nanoparticles, repeated nucleation occurs in the whole investigated growth temperature range of this study in all the C:TM films independently of the metal type and content. This is in contrast to systems such as Al-Si or Al-Ge where nanowires with a height equal to the film thickness are formed already at RT. Even the results above cannot give an unambiguous answer to the reason of such a behavior, the findings of this work strongly suggest that the insufficient mobility is not the reason of such a behavior as at the highest growth temperature the onset of bulk diffusion is already observed. The 2D nature of graphite-like carbon whose formation is catalyzed and stabilized by the metal and the carbon capability to form stable curved graphene-like or fullerene-like sheets is the most probable reason for this effect. In this picture the growth proceeds as a competition of surface diffusion induced lateral phase separation promoting the formation of columnar structures and the formation of metastable metal catalyzed curved carbon structures with the tendency to encapsulate the metal nanoparticles. The observed tendencies demonstrate that the growth of nanocolumns with a height equal to the film thickness in the presence of a matrix consisting of a layered material (carbon, boron nitride, carbon nitride, ...) is very challenging if possible at all.

Concerning the carbon matrix, the results clearly demonstrate that metal influence qualitatively as well as quantitatively is very different in the surface and bulk diffusion dominated regimes. The present results clearly show that *all* the metals significantly enhance the formation of sixfold ring carbon clusters. This enhancement occurs independently of the nanoparticle size, shape, and phase, and metal content. The fact that this effect is strongly retarded in pure carbon films indicating about a low carbon self diffusion and the observation that the curved graphite-like structures are observed only at the close vicinity of the nanoparticles allows us to attribute this effect to the action of the metal nanoparticles as sixfold ring templates or fast diffusion short-circuits.

The sixfold ring formation enhancement degree depends on the transition metal type and content, and decreases for ∼30 at.% metal in the order Co > V > Cu. It should be noted, that the degree of enhancing sixfold ring clustering and the ordering

within the clusters do not change with temperature for C:V films while it changes for other C:TM films and even for carbon reference films. This strongly points out that metal phase even promoting the formation of graphite-like structures hinders their further development by imposing geometrical constraints. In addition to imposing curvature on the surrounding carbon matrix, the nanoparticles themselves can act as obstacles for extended planar graphitic plane growth. It is consistent with the observation that there is an optimal metal content which provides the largest amount of interfaces, thus largest amount of sixfold ring clustered material. Lower or larger metal content provides lower amount of interfaces due to lower metal/matrix ratio or particle coarsening, respectively.

In contrast to the 'catalytic' activity in the surface diffusion governed mode, only the eutectic Co-C system brings about the carbon graphitization for the bulk diffusion governed mode. No graphitization upon annealing occurs for the peritectic (Cu-C) or intermediate compound (V-C) system, and for pure carbon films owing to the very low solubility of carbon in the metal phase for the former and the slow carbon diffusivity for the latter two, respectively. The results suggest that for a metal nanoparticle to act as a catalyst, it should act as a carbon solvent and should exhibit a certain mobility as a whole. Such a behavior is a particular case of the 'dynamic' nanoparticle behavior in different chemical environments as observed for supported metal nanoparticles in reducing/oxidizing gases [188] or during carbon nanotube growth. The results are also consistent with a dissolution-diffusion-precipitation mechanism, similar to the metal-mediated crystallization of amorphous silicon and germanium which also form eutectic systems. For stable encapsulated particles such as those for C:V system, no changes occur in either dispersed phase or the matrix the latter most probably being stabilized by the dispersed phase imposed spatial constraints. For mobile nanoparticles but not exhibiting considerable carbon solubility such as those present in the Cu-C system, the thermal activation induced movement of the nanoparticles in the matrix actually induces even higher matrix disorder.

7 Appendix

7.1 Raman spectra fitting parameters of as-deposited C and C:TM films

Table 7.1: Raman spectra fitting results of C reference films grown at different substrate temperatures.

T	D peak		G peak			I_D/I_G
	Center	Γ_D	Center	Γ_G	q	
(°C)	(cm^{-1})	(cm^{-1})	(cm^{-1})	(cm^{-1})		
RT	1387	165	1539	204	-10.88	0.15
100	1378	203	1542	195	-9.18	0.32
200	1366	234	1552	182	-6.83	0.56
300	1363	245	1558	167	-5.93	0.75
400	1362	242	1565	156	-5.68	0.83
500	1364	237	1575	143	-5.77	0.87

Table 7.2: Raman spectra fitting results of tetrahedral amorphous carbon (ta-C), nanocrystalline graphite and graphite.

Reference	D peak		G peak			I_D/I_G
	Center	Γ_D	Center	Γ_G	q	
	(cm^{-1})	(cm^{-1})	(cm^{-1})	(cm^{-1})		
ta-C	-	-	1540	219	-7.76	0
nanocryst. graphite	1350	46	1583	18	-8.14	0.83
graphite	-	-	1581	14	-108.3	0

Table 7.3: Raman spectra fitting results of C:Co (∼15 at.%), C:Co (∼30 at.%) and C:Co (∼40 at.%) films grown at different temperatures.

T	Co content	D peak		G peak			I_D/I_G
		Center	Γ_D	Center	Γ_G	q	
(°C)	(cm^{-1})	(cm^{-1})	(cm^{-1})	(cm^{-1})			
RT	∼15	1354	241	1538	170	-6.41	0.83
100	∼15	1354	248	1541	171	-6.59	0.87
200	∼15	1354	246	1548	169	-6.34	0.87
300	∼15	1358	249	1557	163	-6.22	0.88
400	∼15	1362	250	1565	159	-5.90	0.93
500	∼15	1366	243	1576	146	-6.05	0.93
RT	∼30	1352	281	1532	165	-6.89	1.19
100	∼30	1351	286	1536	169	-7.35	1.13
200	∼30	1350	268	1545	174	-6.36	1.03
300	∼30	1356	268	1556	168	-6.12	1.00
400	∼30	1364	249	1568	155	-5.63	0.99
500	∼30	1357	210	1583	121	-6.11	0.96
RT	∼40	1337	284	1518	210	-11.48	0.97
100	∼40	1343	271	1533	175	-5.63	1.03
200	∼40	1349	268	1541	173	-5.91	1.03
300	∼40	1354	277	1554	172	-6.29	1.02
400	∼40	1362	270	1563	164	-5.94	1.02
500	∼40	1365	250	1578	139	-6.44	1.02

Table 7.4: Raman spectra fitting results of C:Cu (∼15 at.%) and C:Cu (∼30 at.%) films grown at different temperatures.

T	Cu content	D peak		G peak			I_D/I_G
		Center	Γ_D	Center	Γ_G	q	
(°C)	(cm^{-1})	(cm^{-1})	(cm^{-1})	(cm^{-1})			
RT	∼15	1361	246	1538	175	-7.02	0.69
100	∼15	1356	251	1541	176	-6.39	0.77
200	∼15	1352	253	1545	176	-5.97	0.84
300	∼15	1353	251	1555	162	-5.59	0.88
400	∼15	1363	235	1574	140	-5.71	0.86
500	∼15	1363	213	1588	117	-6.71	0.88
RT	∼30	1362	252	1541	171	-6.98	0.65
100	∼30	1359	260	1545	173	-5.60	0.73
200	∼30	1355	260	1549	174	-5.64	0.80
300	∼30	1355	257	1557	167	-5.36	0.82
400	∼30	1360	243	1570	150	-5.70	0.81
500	∼30	1361	213	1584	121	-6.30	0.80

Table 7.5: Raman spectra fitting results of C:V (∼15 at.%) and C:V (∼30 at.%) films grown at different temperatures.

T	V content	D peak		G peak			I_D/I_G
		Center	Γ_D	Center	Γ_G	q	
(°C)	(cm^{-1})	(cm^{-1})	(cm^{-1})	(cm^{-1})			
RT	∼15	1356	269	1536	171	-5.98	1.00
100	∼15	1354	262	1539	171	-5.75	0.96
200	∼15	1356	265	1547	170	-5.45	0.94
300	∼15	1358	254	1552	169	-5.64	0.92
400	∼15	1365	264	1561	158	-5.65	0.93
500	∼15	1368	250	1573	145	-5.77	0.91
RT	∼30	1362	246	1552	149	-8.38	1.03
100	∼30	1370	248	1561	140	-8.16	1.05
200	∼30	1367	240	1560	141	-7.45	0.98
300	∼30	1367	248	1561	143	-8.16	0.96
400	∼30	1360	248	1556	151	-6.70	0.93
500	∼30	1365	250	1565	148	-7.11	0.95

7.2 Raman spectra fitting parameters of annealed samples

Table 7.6: Raman spectra fitting results of C reference films grown at 200°C and of postannealed films at T_a=300-700°C.

T	D peak		G peak				I_D/I_G	L_a
	Center	Γ_D	Center	Γ_G	q	$\lvert\Gamma_G/q\rvert$		
(°C)	(cm^{-1})	(cm^{-1})	(cm^{-1})	(cm^{-1})		(cm^{-1})		($\AA$)
200	1365	249	1555	177	-5.46	32	0.71	11.4
300	1368	251	1556	177	-5.40	33	0.71	11.4
400	1368	247	1556	174	-5.45	32	0.71	11.4
500	1367	245	1557	173	-5.42	32	0.71	11.4
550	1366	245	1558	169	-5.39	31	0.76	11.8
600	1366	244	1559	165	-5.49	30	0.78	11.9
650	1365	242	1560	162	-5.57	29	0.80	12.1
700	1364	245	1563	158	-5.71	28	0.84	12.4

Table 7.7: Raman spectra fitting results of C:Co (∼35 at.%) films grown at 200°C and of postannealed films at T_a=300-700°C.

T	D peak		G peak				I_D/I_G	L_a
	Center	Γ_D	Center	Γ_G	q	$\lvert\Gamma_G/q\rvert$		
(°C)	(cm^{-1})	(cm^{-1})	(cm^{-1})	(cm^{-1})		(cm^{-1})		($\AA$)
200	1350	268	1545	174	-6.36	27	1.03	13.7
300	1353	271	1546	172	-6.45	27	1.00	13.5
400	1355	270	1551	169	-6.06	28	0.97	13.3
500	1358	260	1561	160	-5.64	28	0.94	13.1
550	1362	250	1569	146	-5.81	25	0.94	13.0
600	1360	233	1578	131	-5.89	22	0.92	12.9
650	1356	206	1585	109	-6.46	17	0.80	54.7
700	1351	108	1588	62	-15.14	4	0.52	84.3

Table 7.8: Raman spectra fitting results of C:V (∼35 at.%) films grown at 200°C and of postannealed films at T_a=300-700°C.

T	D peak		G peak				I_D/I_G	L_a
	Center	Γ_D	Center	Γ_G	q	$\lvert\Gamma_G/q\rvert$		
(°C)	(cm^{-1})	(cm^{-1})	(cm^{-1})	(cm^{-1})		(cm^{-1})		($\mathring{A}$)
200	1370	309	1562	148	-7.98	19	0.98	13.3
300	1371	274	1569	135	-8.64	16	0.95	13.2
400	1373	291	1569	138	-7.19	19	0.97	13.3
500	1372	269	1573	133	-8.87	15	0.97	13.3
550	1370	288	1572	134	-6.07	22	0.96	13.2
600	1368	250	1571	135	-6.43	21	0.92	13.0
650	1365	257	1573	137	-6.33	22	0.92	12.9
700	1364	244	1575	133	-6.25	21	0.89	12.7

Table 7.9: Raman spectra fitting results of C:Cu (∼40 at.%) films grown at 200°C and of postannealed films at T_a=300 and 400°C. Before fitting the copper photoluminescence spectra has been subtracted from the Raman spectra.

T	D peak		G peak				I_D/I_G	L_a
	Center	Γ_D	Center	Γ_G	q	$\lvert\Gamma_G/q\rvert$		
(°C)	(cm^{-1})	(cm^{-1})	(cm^{-1})	(cm^{-1})		(cm^{-1})		($\mathring{A}$)
200	1352	144	1553	173	-4.53	38	0.86	12.5
300	1354	146	1555	171	-4.37	39	0.87	12.6
400	1358	140	1559	163	-4.63	35	0.85	12.4

Bibliography

[1] Ajayan PM, Schadler LS, Braun PV. Nanocomposite science and technology. Wiley-VCH; 2005.

[2] Ohring M. The Materials Science of Thin Films. Academic Press; 2006.

[3] Abrasonis G, Kovács GJ, Mücklich A, Zhou S, Babonneau D, Martinavičius A, et al. J PhysChem C. 2009;113:8645.

[4] Hayashi T, Hirono S, Tomita M, Umemura S. Nature. 1996;381(6585):772.

[5] Yu M, Liu Y, Sellmyer DJ. J Appl Phys. 1999;85(8):4319.

[6] Wang H, Wong SP, Cheung WY, Ke N, Chiah MF, Liu H, et al. J Appl Phys. 2000;88(4):2063.

[7] Wang H, Chiah MF, Cheung WY, Wong SP. Phys Lett A. 2003;316(1-2):122.

[8] Shi J, Azumi M, Nittono O. Appl Phys A. 2001;73:215.

[9] Wang H, Wong SP, Li WQ, Chiah MF, Poon CY, Cheung WY, et al. Thin Solid Films. 2002;405(1-2):304.

[10] Babonneau D, Cabioc'h T, Naudon A, Girard JC, Denanot MF. Surf Sci. 1998;409(2):358.

[11] Nie X, Jiang JC, Tung LD, Spinu L, Meletis EI. Thin Solid Films. 2002;415:211.

[12] Yang S, Li X, Renevier NM, Teer DG. Surf Coat Technol. 2001;142:85.

[13] Patscheider J. MRS Bull. 2003;28:180.

[14] Pauleau Y, Thièry F. Surf Coat Technol. 2004;180-81:313.

[15] Knotek O, Lugscheider E, Löffler F, Bosserhoff B, Schmitz S. Mater Sci Eng A. 1996;209:394.

[16] Voevodin AA, Zabinski JS. J Mater Sci. 1998;33:319.

[17] Kovács GJ, Sáfrán G, Geszti O, Ujvári T, Bertóti I, Radnóczi G. Surf Coat Technol. 2004;180-81:331.

[18] Sedlačková K, Lobotka P, Vávra I, Radnóczi G. Carbon. 2005;43(10):2192.

[19] Zhou S, Berndt M, Bürger D, Heera V, Potzger K, Abrasonis G, et al. Acta Materialia. 2009;57:4758.

[20] Abrasonis G, Krause M, Mücklich A, Sedlačková K, Radnóczi G, Kreissig U, et al. Carbon. 2007;45(15):2995.

[21] Babonneau D, Briatico J, Petroff F, Cabioc'h T, Naudon A. J Appl Phys. 2000;87(7):3432.

[22] Delaunay JJ, Hayashi T, Tomita M, Hirono S. J Appl Phys. 1997;82(5):2200.

[23] Babonneau D, Toudert J, Camelio S, Pailloux F, Cabioc'h T, Girardeau T. Surf Coat Technol. 2006;200(22-23):6251.

[24] Cabioc'h T, Naudon A, Jaouen M, Thiaudiere D, Babonneau D. Philosophical Magazine B-Physics of Condensed Matter Statistical Mechanics Electronic Optical and Magnetic Properties. 1999;79(3):501.

[25] Konno TJ, Shoji K, Sumiyama K, Suzuki K. J Magn Magn Mater. 1999;195:9.

[26] Mi WB, Guo L, Jiang EY, Li ZQ, Wu P, Bai HL. J Phys D. 2003;36:2393.

[27] Voevodin AA, Zabinski JS. Diamond Rel Mat. 1998;7:463.

[28] Thièry F, Pauleau Y, Grob JJ, Babonneau D. Thin Solid Films. 2004;466:10.

[29] Pauleau Y, Thièry F, Latrasse L, Dub SN. Surf Coat Technol. 2004;188-189:484.

[30] Gulbiński W, Kukuelka S, Pauleau Y, Thièry F. Surf Coat Technol. 2005;200:2146.

[31] Pauleau Y, Thièry F. Mat Lett. 2002;56:1053.

[32] Sedlačková K, Ujvári T, Grasin R, Lobotka P, Bertóti I, Radnóczi G. Vacuum. 2008;82:214.

[33] Konno TJ, Sinclair R. Acta Metall Mater. 1994;42(4):1231.

[34] Abrasonis G, Scheinost A, Zhou S, Torres R, Gago R, Jiménez I, et al. J Phys Chem C. 2008;112:12628.

[35] Massalski TB, Okamoto H, Subramanian PR, Kacprzak L. Binary Alloy Phase Diagrams, Second Edition. ASM International; 1990.

[36] Pierson HO. Handbook of carbon, graphite, diamond and fullerenes: properites, processing and application. Noyes Publication, New Jersey; 1993.

[37] Dresselhaus MS, Kalish R. Ion Implantation in Diamond, Graphite and Related Materials. Springer-Verlag, Berlin; 1992.

[38] Cotton FA, Wilkinson G. Physical Chemistry. Interscience Publishers, New York; 1972.

[39] Robertson J. Adv Phys. 1986;35(4):317.

[40] Prawer S, Rossouw CJ. J Appl Phys. 1988;63(9):4435.

[41] Korshak VV, Kudryavtsev YP, Khvostov W, Guseva MB, Babaev VG, Rylova OY. Carbon. 1987;25(6):735.

[42] Ferrari AC, Robertson J. Phys Rev B. 2001;64(7):13.

[43] Austerman SB. Chemistry and Physics of Carbon. Dekker, New York; 1968.

[44] Moore AW. Chemistry and Physics of Carbon. Dekker, New York; 1973.

[45] Jenkins GM, Kawamura K. Polymeric Carbons - Carbon Fibre, Glass and Char. Cambridge Univ. Press, London; 1976.

[46] Dresselhaus MS, Dresselhaus G, Sugihara K, Spain IL, Goldberg HA. Graphite Fibers and Filaments. Springer-Verlag, Berlin; 1988.

[47] Dresselhaus MS, Dresselhaus G, Eklund PC. Science of Fullerenes and Carbon Nanotubes. Academic Press, San Diego; 1996.

[48] Dresselhaus MS, Dresselhaus G, Avouris P. Carbon Nanotubes: Synthesis, Structure, Properties and Application. Springer-Verlag, Berlin; 2001.

[49] Meyyappan M. Carbon Nanotubes: Science and Application. CRC Press, Boca Raton; 2005.

[50] Novoselov KS, Geim AK, Morozov SV, Jiang D, Katsnelson MI, Grigorieva IV, et al. Nature. 2005;438:7065.

[51] Eight Allotropes of Carbon, www.nationmaster.com/encyclopedia/Carbon; 7. February 2006.

[52] Kelly BT. Physics of Graphite. Applied Science, London; 1981.

[53] Kittel C. Introduction to Solid State Physics. Wiley, New York; 1986.

[54] Bundy FP. J Geophys Res. 1980;85(NB12):6930.

[55] Bundy FP. Solid State Physics under Pressure. Reidel, Dordrecht; 1985.

[56] Ferrari AC, Robertson J. Phys Rev B. 2000;61(20):14095.

[57] Robertson J. Prog Solid State Chem. 1991;21(4):199.

[58] Robertson J. Pure Appl Chem. 1994;66(9):1789.

[59] Robertson J. Mat Sci Eng. 2002;37:129.

[60] McNaught AD, Wilkinson A. IUPAC Compendium of Chemical Terminology. IUPAC International Union of Pure and Applied Chemistry; 1997.

[61] Greenwood NN, Earnshaw A. Chemie der Elemente. VCH, Weinheim; 1990.

[62] Christen HR. Grundlagen der allgemeinen und anorganischen Chemie. Sauerländer, Salle; 1973.

[63] Eulitz CM, Scheuermann S, Thier HJ. Brockhaus ABC Chemie. VEB F. A. Brockhaus, Leipzig; 1971.

[64] Vainshtein BK, Fridkin VM, Indenbom VL. Structure of Crystals. Springer, Berlin; 2000.

[65] Cahn RW. Physical Metallurgy. North-Holland Publishing Company, Amsterdam; 1965.

[66] Dietz M. Vorlesung Werkstofftechnik; 2001. Studium Physikalische Technik, WH Zwickau.

[67] Rudy E, Windisch S, Brukl CE. Planseeber Pulvermetall. 1968;16:3.

[68] Storms EK, McNeal RJ. J Phys Chem. 1962;66(8):1401.

[69] Adelsberg LM, Cadoff LH. J Am Ceram Soc. 1968;51(4):213.

[70] Storms E. The Refractory Carbides. Academic Press, New York; 1973.

[71] Guillermet AF. Z Metallkd. 1987;78(10):700.

[72] Ishida K, Nishizawa T. J Phase Equilibria. 1991;12(4):417.

[73] Nagakura S. J Phys Soc Japan. 1961;16(6):1213.

[74] Ruff O, Bergdahl B. Z Anorg Allg Chem. 1919;106(2):76.

[75] Bever MB, Floe CF. Trans AIME. 1946;166:128.

[76] McLellan RB. Scr Metall. 1969;3(6):389.

[77] Snead MC, Maynard JL, Brasted RC. Comprehensive Inorganic Chemistry, Vol. 2, Copper, Silver and Gold. van Nostrand, Princeton; 1954.

[78] Petrov I, Barna PB, Hultman L, Green JE. J Vac Sci Technol A. 2003;21(5):117.

[79] Neidhardt A. Vorlesung Physikalische Verfahrenstechnik; 2003. Studium Physikalische Technik, WH Zwickau.

[80] Kienel G, Röll K. Vakuumbeschichtung 2, Verfahren und Anlagen. VDI Verlag; 1995.

[81] Barna PB, Adamik M. Thin Solid Films. 1998;317:27.

[82] Venables JA. Introduction to Surface and Thin Film Processes. Cambridge University Press; 2000.

[83] Venables JA. Surf Science. 1994;798:299.

[84] Lüth H. Surfaces and Interfaces of Solid Materials. Springer-Verlag, Berlin; 1995.

[85] Movchan BA, Demchishin AV. Fiz Metal Metalloved. 1969;28:653.

[86] Thornton JA. J Vac Sci Technol. 1974;11:660.

[87] Messier R, Giri AP, Roy RA. J Vac Sci Technol A. 1984;2:500.

[88] Kelly PJ, Arnell RD. J Vac Sci Technol A. 1998;16:2858.

[89] Pócza JF, Barna Á, Barna PB, Pozsgai I, Radnóczi G. Jpn J Appl Phys. 1974;2:525.

[90] Eisenmenger-Sittner C, Bangert H, Stori H, Brenner J, Barna PB. Surf Sci. 2001;489:161.

[91] Barna A, Barna PB, Radnóczi G, Reicha FM, Toth L. Phys Status Solidi A. 1979;55:427.

[92] Fukutani K, Tanji K, Saito T, Den T. Jpn J Appl Phys. 2008;47(2):1140.

[93] Atzmon M, Kessler DA, Srolovitz DJ. J Appl Phys. 1992;72(2):442.

[94] Fukutani K, Tanji K, Saito T, Den T. J Appl Phys. 2005;98:033507.

[95] Cahn JW, Hilliard JE. J Chem Phys. 1958;28:258.

[96] Adams CD, Srolovitz DJ, Atzmon M. J Appl Phys. 1993;74(3):1707.

[97] He JH, Carosella CA, Hubler GK, Qadri SB, Sprague JA. Phys Rev B. 2006;73:235406.

[98] Aouni A, Weisbecker P, Loi TH, Bauer-Grosse E. Thin Solid Films. 2004;469-470:315.

[99] Sainte-Catherine MC, Farges G. Surf Coat Technol. 1992;54/55:266.

[100] Adelhelm C, Bladen M, Rinke M, Stueber M. J Appl Phys. 2009;105:033522.

[101] Wang H, Chiah MF, Cheung WY, Wong SP. Phys Lett A. 2003;316:122.

[102] Mamezaki O, Adachi H, Tomita S, ans S Hayashi MF. Jpn J Appl Phys. 2000;39:6680.

[103] Wang FL, Jiang JC, Meletis EI. Appl Phys Lett. 2003;83(12):2423.

[104] Wang FL, Jiang JC, Meletis EI. J Appl Phys. 2004;95(9):5069.

[105] Sundgren E, Hentzell HTG. J Vac Sci Technol A. 1986;4:2259.

[106] Zabinski JS, Voevodin AA. J Vac Sci Technol A. 1998;16:1890.

[107] Delaunay JJ, Hayashi T, Tomita M, Hirono S. Jpn J Appl Phys. 1997;36:7801.

[108] Wang H, Wong SP, Cheung WY, Ke N, Wen GH, Zhang XX, et al. J Appl Phys. 2000;88(8):4919.

[109] Wang FL, Jiang JC, Meletis EI. J Appl Phys. 2003;83(12):2423.

[110] Konno TJ, Sinclair R. Acta Metall Mater. 1995;43:471.

[111] Uglov VV, Kuleshov AK, Astashynskaya MV, Anishchik VM, Dub SN, Thièry F, et al. Composites Science Technol. 2005;65:785.

[112] Musil J, Louda M, Soukup Z, Kubásek M. Diam Rel Mat. 2008;17:1905.

[113] Onoprienko AA, Danilenko NI, Kossko IA. Thin Solid Films. 2007;515:6672.

[114] Frey H. Vakuumbeschichtung 1, Plasmaphysik - Plasmadiagnostik - Analytik. VDI Verlag, Düsseldorf; 1995.

[115] Kaufman HR, Cuomo JJ, Harper JME. J Vac Sci Technol. 1982;21(3):725.

[116] Ion Source Manual, Ion Tech Inc.; 1992.

[117] Simmons JM, Nichols BM, Marcus MS, Castellini OM, Hamers RJ, Eriksson MA. Small. 2006;2(7):902.

[118] Kreissig U, Grötzschel R, Behrisch B. Nucl Instr and Meth B. 1994;85(1):71.

[119] Barradas NP, Jeynes C, Webb RP. Appl Phys Lett. 1994;71(2):291.

[120] Lifshin E. X-ray Characterization of Materials. Wiley-VHC, Weinheim; 1999.

[121] Cullity BD, Stock SR. Elements of X-ray Diffraction. Prentice-Hall; 2001.

[122] Bubert H, Jenett H. Surface and Thin Film Analysis. Wiley-VHC, Weinheim; 2002.

[123] Spie L, Schwarzer R, Behnken H, Teichert G. Moderne Röntgenbeugung. Teubner Verlag, Wiesbaden; 2005.

[124] Als-Nielsen J, McMorrow D. Elements of Modern X-Ray Physics. Wiley-VHC, Weinheim; 2001.

[125] Gardiner DJ. Practical Raman spectroscopy. Springer-Verlag; 1989.

[126] Kuzmany H. Festkörperspektroskopie. Springer-Verlag; 1990.

[127] Saito R, Grüneis A, Samsonidze GG, Brar VW, Dresselhaus G, Dresselhaus MS, et al. New J Phys. 2003;5:157.1.

[128] Reich S, Thomsen C. Philos Trans R Soc A-Math Phys Eng Sci. 2004;362(1824):2271.

[129] Castiglioni C, Tommasini M, Zerbi G. Philos Trans R Soc A-Math Phys Eng Sci. 2004;362(1824):2425.

[130] Negri F, di Donato E, Tommasini M, Castiglioni C, Zerbi G, Mullen K. J Chem Phys. 2004;120(24):11889.

[131] Thomsen C, Reich S. Phys Rev Lett. 2000;85(24):5214.

[132] Maultzsch J, Reich S, Thomsen C. Phys Rev B. 2004;70(15):9.

[133] Tuinstra F, Koenig JL. J Chem Phys. 1970;53(3):1126.

[134] Elman BS, Dresselhaus MS, Dresselhaus G, Maby EW, Mazurek H. Phys Rev B. 1981;24(2):1027.

[135] Ferrari AC, Robertson J. Philos Trans R Soc A - Math Phys Eng Sci. 2004;362(1824):2477.

[136] Castiglioni C, Mapelli F C andNegri, Zerbi G. J Chem Phys. 2000;114(2):963.

[137] Vidano RP, Fischbach DB, Willis LJ, Loehr TM. Solid State Commun. 1981;39(2):341.

[138] Ferrari AC, Rodil SE, Robertson J. Phys Rev B. 2003;67(15):20.

[139] Lespade P, Marchard A, Couzi M, Cruege F. Carbon. 1984;22(4):375.

[140] Elman BS, Shayegan M, Dresselhaus MS, Mazurek H, Dresselhaus G. Phys Rev B. 1992;25(6):4142.

[141] Shiao J, Hoffman RW. Thin Solid Films. 1996;283(1-2):145.

[142] Yoshikawa M, Nagai N, Matsuki M, Fukuda H, Katagiri G, Ishida H, et al. Phys Rev B. 1992;46(11):7169.

[143] Tamor MA, Vassell WC. J Appl Phys. 1994;76(6):3823.

[144] Sadezky A, Muckenhuber H, Grothe H, et al. Carbon. 2005;43(8):1731.

[145] McCulloch DG, Prawer S, Hoffman A. Phys Rev B. 1994;50(9):5905.

[146] Abrasonis G, Berndt M, Krause M, Küpper K, Munnik F, Kolitsch A, et al. J Phys Chem C. 2008;112(44):17161.

[147] Abrasonis G, Kovács GJ, Ryves L, Krause M, Mücklich A, Munnik F, et al. J Appl Phys. 2009;105:083518.

[148] Powder Diffraction File, International Center for Diffraction Data; Card 72-1369 for cobalt carbide.

[149] Powder Diffraction File, International Center for Diffraction Data; Card 05-0727 for hexagonal cobalt and Card 15-0806 for cubic cobalt.

[150] Berndt M, Krause M, Abrasonis G, Mücklich A, Munnik F, Kolitsch A, et al.; 2009. DOI:10.1002/ppap.200932308.

[151] Guillermet AF. ZMetallkd. 1987;78(10):700.

[152] Powder Diffraction File, International Center for Diffraction Data; Card 04-0836 for cubic copper.

[153] Powder Diffraction File, International Center for Diffraction Data; Card 73-0476 for cubic vanadium carbide.

[154] Pei YT, Galvan D, Hosson JTMD, Cavaleiro A. Surf Coat Technol. 2005;198:44.

[155] Pei YT, Galvan D, Hosson JTMD, Strondl C. J Europ Ceramic Soc. 2006;26:565.

[156] Krause M; Private communication.

[157] Dillon RO, Woollam JA, Katkanant V. Phys Rev B. 1983;29(6):3482.

[158] Kovács GJ, Veres M, Koós M, Radnóczi G. Thin Solid Films. 2008;516(21):7910.

[159] Dahany P, Fleurovy V, Thurianz P, Heitzz R, Hoffmannz A, Broserz I. J Phys Condens Matter. 1998;10:2007.

[160] Townsend PD, Brooks R, Hole DE, Wu Z, Turkler A, Can N, et al. Appl Phys B. 2001;73:345.

[161] Wang XB, Song C, Geng KW, Zeng F, Pan F. Appl Surf Science. 2007;253:6905.

[162] Maultzsch J, Reich S, Thomsen C, Requardt H, Ordejon P. Phys Rev Lett. 2004;92(7):4.

[163] Campell C. Surf Sci Rep. 1997;27:1.

[164] Egelhoff WF, Tibbetts GG. Phys Rev B. 1979;19(10):5028.

[165] Schmidt AA, Eggers H, Herwig K, Anton R. Surf Sci. 1996;349(3):301.

[166] Hamilton JF, Logel PC. J Catal. 1973;29(2):253.

[167] Hamilton JF, Logel PC. Thin Solid Films. 1974;23(1):89.

[168] Hamilton JF, Logel PC, Baetzold RC. Thin Solid Films. 1976;32(2):233.

[169] Ratsch C, Venables JA. J Vac Sci Technol A. 2003;21:96.

[170] Mohaddes-Ardacili L, Zheng H, Ogale SB, Hannoyer B, Tian W, Wang J, et al. Nat Mater. 2004;3:533.

[171] Zheng H, Wang J, Lofland SE, Ma Z, Mohaddes-Ardacili L, Zhou T, et al. Science. 2004;303:661.

[172] Fukutani K, Ishida Y, Tanji K, Den T. Thin Solid Films. 2007;515:4629.

[173] Yasui N, Horie R, Ohashi Y, Tanji K, Den T. Adv Mater. 2007;19:2797.

[174] Babonneau D, Pailloux F, Eymery JP, Denanot MF, Guerin P, Fonda E, et al. Phys Rev B. 2005;71(3):13.

[175] Krause M, Abrasonis G, Kolitsch A, Mücklich A, Kreissig U, Möller W. Phys Stat Sol (b). 2007;244(11):4236.

[176] Marsh H, Warburton AP. J Appl Chem. 1970;20(5):133.

[177] Oya A, Otani S. Carbon. 1979;17(2):131.

[178] Takagi D, Homma Y, Hibino H, Suzuki S, Kobayashi Y. Nano Lett. 2006;6(12):2642.

[179] Cantoro M, Hofmann S, Pisana S, Scardaci V, Parvez A, Ducati C, et al. Nano Lett. 2006;6(6):1107.

[180] Raty JY, Gygi F, Galli G. Phys Rev Lett. 2005;95(9):4.

[181] Hofmann S, Csanyi G, Ferrari AC, Payne MC, Robertson J. Phys Rev Lett. 2005;95(3):036101.

[182] Babonneau D, Jaouen M, Denanot MF, Guerin P, Petroff F. Appl Phys Lett. 2003;82(18):3056.

[183] Babonneau D, Cabioc'h T, Denanot MF, Naudon A. Appl Phys Lett. 1999;74(6):800.

[184] Hultman L, Bareño J, Flink A, Söderberg H, Larsson K, Petrova V, et al. Phys Rev B. 2007;75:155437.

[185] Sharma A, Brajpuriya R, Tripathi S, Chaudhari S. J Vac Sci Technol A. 2006;24:74.

[186] Sinclair R, Itoh T, Shin R. Microsc Microanal. 2002;8:288.

[187] Hofmann S, Sharma R, Ducati C, Du G, Mattevi C, Cepek C, et al. Nano Lett. 2007;7(3):602.

[188] Newton MA. Chem Soc Rev. 2008;37(12):2644.

List of Figures

List of Tables

Erklärung

Hiermit versichere ich, die vorliegende Arbeit ohne unzulssige Hilfe Dritter und nur unter Benutzung der angegebenen Hilfsmittel angefertigt zu haben. Die aus fremden Quellen direkt oder indirekt übernommenen Gedanken sind als solche kenntlich gemacht. Die Arbeit wurde bisher weder im Innland noch im Ausland in gleicher oder ähnlicher Form einer anderen Prüfungsbehörde vorgelegt. Die Arbeit wurde am Institut für Ionenstrahlphysik und Materialforschung des Forschungszentrums Dresden-Rossendorf unter der wissenschaftlichen Betreuung von Herrn Prof. Dr. W. Möller angefertigt. Die Promotionsordnung der Fakultät für Mathematik und Naturwissenschaften der Technischen Universität Dresden vom 20.03.2000 erkenne ich an.

Dresden, den 09.09.2009

Acknowledgment

I would like to thank all people who contributed to the success of this work, in particular:

- To Prof. Wolfhard Möller for the supervision of this work and for the opportunity to work at the Institute of Ion Beam Physics and Material Research of the Forschungszentrum Dresden-Rossendorf.

- To Gintautas Abrasonis for the assistance in the strategical planning of the experiments as well as for useful discussions concerning the result interpretation.

- To Matthias Krause for the assistance in the Raman spectroscopy measurements as well in the fitting and the interpretation of the results.

- To Arndt Mücklich, György J. Kovács and prof. György Radnóczi for TEM analysis and to Annette Kunz for preparing the samples for TEM. The assistance of György J. Kovács in the interpretation of the TEM results is particularly acknowledged.

- To Andrea Scholz and Jörg Grenzer for measuring a large amount of samples by XRD and XRR.

- To Uli Kreissig and Frans Munnik for ERDA analysis.

- To Uta Lucessi and Joachim Wagner for their technical support during the Raman spectroscopic measurements.

- To Heike Felsmann, Claudia Neisser and Gabi Schnabel for the preparation of the SiO_2/Si substrates.

- To Günther Anwandt, Jürgen Grahl, Mario Steinert, Jens Zscharschuch, Robert Aniol and Udo Strauch for the mechanical constructions at the deposition chamber, the supply with media and their support in all technical problems which occurred at the deposition chamber.

- To Georg Talut for the opportunity to use the annealing equipment and his help using Latex.

- The FWII- and FWIN- team for a very collegial and pleasant working atmosphere.

- To my family for their moral support during preparation of the thesis.

Furthermore, I would like to thank the European Union for funding the integrated project „Fullerenebased Opportunities for Robust Engineering: Making Optimized Surfaces for Tribology“ under the contract number NMP3-CT-2005-515840.